

# Metal Phosphates as Proton Conducting Materials for Intermediate Temperature Fuel Cell and Electrolyser Applications

**Anfimova, Tatiana**

*Publication date:*
2014

*Document Version*
Publisher's PDF, also known as Version of record

Tatiana Viktorovna Anfimova

**PhD Thesis**

# Metal Phosphates as Proton Conducting Materials for Intermediate Temperature Fuel Cell and Electrolyser Applications

Kongens Lyngby, June 2014

Metal Phosphates as Proton Conducting Materials for Intermediate Temperature Fuel Cell and Electrolyser Applications

**Author:**
Tatiana Viktorovna Anfimova

**Supervisor:**
Associate Professor Qingfeng Li
**Co-supervisors:**
Professor Niels J. Bjerrum
Associate Professor Jens Oluf Jensen

This work has received financial support from the Danish National Research Foundation (the PROCON Center) and the Danish Council for Strategic Research (MEDLYS).

Section of Proton conductors
Department of Energy Conversion and Storage
Technical University of Denmark
Kemitorvet building 207, room 045
DK-2800 Kgs. Lyngby
Denmark

Tel. (+45) 45 25 23 08
E-mail: tatia@dtu.dk

*"I believe that water will one day be employed as fuel, that hydrogen and oxygen which constitute it, used singly or together, will furnish an inexhaustible source of heat and light "*

*Jules Verne "Mysterious Island" 1874*

*The greatest invention of the nineteenth century was the invention of the method of invention*

*A. N. Whitehead*

**Abstract**

The present thesis presents the results achieved during my ph.d. project on a subject of intermediate temperature proton conducting metal phosphates as electrolyte materials for fuel cells and electrolysers.

Fuel cells and electrolysers are electrochemical devices with high energy conversion efficiency and have been proposed as the future energy technology in association with renewable power sources. The currently available technologies are either operating at lower or higher temperatures. To achieve an intermediate temperature operation between 200 and 400 $^{o}$C, a key material is the electrolyte with a proton conductivity of above $10^{-2}$S cm$^{-1}$. Chapter 1 of the thesis is an introduction to basics of fuel cell and electrolyser technologies as well as proton conducting materials.

Extended discussion on the proton conducting materials, a particularly phosphates is made in Chapter 2. Three major types of phosphates were systematically reviewed including solid acids or alkali hydrogen phosphates, pyrophosphates, and rare earth metal phosphates. Demonstration of the fuel cell technology based on solid acid proton conductor $CsH_2PO_4$ has inspired the active research in the area. Based on the literature survey, the thesis work is defined and outlined.

Chapter 3 describes in details the theoretical background of techniques used in the present study. A significant part of the present study involves conductivity measurements with electrochemical impedance technique, which are discussed in Chapter 4.

The research work starts with synthesis and investigation of three rare earth metal phosphate hydrates, which is first presented in Chapter 5. Structural and surface water as well as its stability has been investigated using thermogravimetric and differential thermal analyses combined with structural modeling calculations. Conductivity results of the phosphates are presented.

The rare earth metal phosphates are further explored by preparing composites with cesium dihydrogen phosphate. The properties of the composites are characterized using SEM/EDX, XRD, TGA/DTA and conductivity measurements in slightly humidified atmosphere. The results are presented in Chapter 6.

In Chapter 7 the structure and conductivity mechanism of indium doped tin pyrophosphates are reported. For this purpose three synthetic techniques are employed to prepare a variety of the pyrophosphates with or without post treatments with phosphoric acid. The conductivity and its stability are studied and correlated with the phosphate morphologies. The additional solid state NMR studies have been performed in collaboration with Southern Denmark University (SDU). Chapter 8 presents the result obtained for a novel proton conductor based on cerium ultraphosphate. The ultraphosphate is found to be in form of the orthorhombic phase, whose stability is confirmed by heat treatments combined with XRD measurements. Initial measurements of the conductivity and its stability for the cerium ultraphosphate are also presented.

Chapter 9 summarizes conclusions of the thesis work.

Further information concerning experimental measurements is given in Appendixes.

**Dansk resume**

Denne afhandling præsenterer de resultater jeg har opnået i løbet af mit ph.d.-projekt vedrørende medium temperatur protonledende metalphosphater som elektrolyt- materialer til brændselsceller og elektrolysatorer.

Brændselsceller og elektrolysatorer er elektrokemiske enheder med høj energikonverteringseffektivitet, og disse er blevet foreslået som fremtidige energiteknologienheder i forbindelse med vedvarende energikilder. De nuværende tilgængelige teknologier opererer enten ved lave eller høje temperaturer. For at opnå en medium operationstemperatur mellem 200 og 400 $^{o}$C er nøglematerialet en elektrolyt med en protonledningsevne på over $10^{-2}$ $Scm^{-1}$. En introduktion til det grundlæggende i brændselscelle- og elektrolysatorteknologier samt protonledende materialer gives i kapitel 1.

En udvidede diskussion om protonledende materialer særlig om phosphat fremføres i kapitel 2. Tre hovedtyper af phosphater herunder faste sure eller alkaliske hydrogenphosphater, pyrophosphater og metalphosphater af de sjældne jordarter er systematisk blevet undersøgt. Demonstration af brændselscelleteknologi en baseret på den sure faste protonleder $CsH_2PO_4$, har inspireret den aktive forskning på området. Baseret på en litteraturoversigt er afhandlingsarbejdet blevet defineret og beskrevet.

I kapitel 3 beskrives i detaljer den teoretiske baggrund for de teknikker, der anvendes i den foreliggende undersøgelse. En væsentlig del af denne undersøgelse involverer ledningsevnemålinger med elektrokemisk impedansteknik. I kapitel 4 analyseres og diskuteres den elektrokemiske impedansteknik.

I kapitel 5 beskrives forskningsarbejdet med syntese og undersøgelse af tre sjældne jordarters metalphosphathydrater. Strukturelt og overfladebundet vand samt deres stabilitet er blevet undersøgt ved hjælp af termogravimetriske og differentielle termiske analyser kombineret med strukturel modelleringsberegninger. Resultaterne af ledningsevnemålingerne af phosphater præsenteres. Den strukturelle modellering der anvendes i kapitel 5 er blevet selvdesignet udfra eksisterende software til strukturelle modeller.

I kapitel 6 undersøges de sjældne jordarters metalphosphater i forbindelse med fremstilling af kompositter med cæsium dihydrogenphosphat. Egenskaberne af kompositter er kendetegnet ved hjælp af SEM / EDX XRD, TGA / DTA og ledningsevnemålinger i let fugtet atmosfære.

I kapitel 7 er rapporteret en struktur og ledningsevne-mekanisme af indium dopede tinpyrophosphater. Til dette formål er tre synteseteknikker brugt til at forberede en række pyrophosphater med eller uden efterbehandlinger med phosphorsyre. Ledningsevnen og dens stabilitet er blevet undersøgt og sammenholdt med phosphat-morfologier. Fastfase NMR-undersøgelser er blevet udført i samarbejde med Syddansk Universitet Danmark (SDU). De i kapitel 7 opnåede resultater har været brugt til udvikling af medium temperatur elektrolysatorer i andre ph.d.-studier.

I kapitel 8 præsenteres de opnåede resultater for en ny protonleder baseret på cerium ultraphosphat. Ultraphosphaten er fundet at være i form af den orthorhombiske fase, hvis stabilitet bekræftes af varmebehandlinger kombineret med XRD målinger. Indledende målinger af ledningsevne og stabilitet af cerium ultraphosphat er også fremlagt.

Kapitel 9 opsummerer konklusionerne i afhandlingen.

Yderligere information om eksperimentelle målinger er givet i Appendices.

**Acknowledgements**

*He who has gone,*
*so we but cherish his memory, abides with us,*
*more potent, nay, more present than the living man.*
*Antoine de Saint-Exupery*

The main source of my inspiration and origin of my strength were my father Viktor and brother Andrey who left me so early but are always in my heart.

This thesis presents the work performed during PhD studies at the Technical University of Denmark (DTU) under the supervision of Associate Professor Qingfeng Li, Professor Niels J. Bjerrum and Associate Professor Jens Oluf Jensen. The work was done at the Department of Energy Conversion and Storage, Section of Proton conductors in the time period from April 2011 to June 2014.

I would like to gratefully acknowledge all my supervisors. First of all, Associate Professor Qingfeng Li:

**开始的**时候，因为我们强烈的个性，我们并无法真正的理解对方。但这始终未影响我对您的深深的敬意和感谢。我决定使用您的母语向您说："**李老**师，谢谢您这三年来对我的指导，以及对我论文的帮**助**.

"At the beginning of my PHD study, because of different personalities, we were not entirely able to understand each other very well, so there was misunderstanding at times. However this did not influence the gratitude and respect in my heart. So I want to say my thanks in your native language. Many thanks for your supervision in past three years and great help with my thesis"

I thank Professor Niels J. Bjerrum for his influence on my research work, scientific development and his valuable advice which had helped me to complete the PhD program.

Also I would like to thank Associate Professor Jens Oluf Jensen providing for a kindness with which we solve all PhD related problems.

To Irina Petrushina who introduces me into the theoretical background of electrochemistry for our nice discussions about science and some cultural differences and challenges I have to give my special thankfulness.

I would also thank Senior researcher Erik Christensen for his valuable supervision in Chapter 7. Other acknowledgement in regard of Chapter 7 is also to graduate students Erik Pristed Jensen and Troels Lie-Andersen, who helped me with the synthesis and experimental part in Chapter 7 and Emeric Truchet for his thesis which was a starting point on this way. I should also thank for assistance in a help with synthesis of cerium ultraphosphate from Ater Baker Al-Ward in Chapter 8.

I am also especially grateful to Senior Scientist Nikolaos Bonanos for an extending my knowledge in Impedance Spectroscopy, very useful discussion about conductivity measurements and cell design.

During the whole work period, a great amount of input was obtained from collaboration with colleagues and friends from DTU and other places. I would like specially thank my colleagues and friends from Section of Proton Conductors, Anton Vasiliev, James Atwoki Mugabi, Claus Burke Mortensen, Larisa Seerup, Lijie Zhong, Lars Nilausen Cleemann, Carsten Brorson Prag and others for providing new ideas and collaborations.

The special thanks is extended to Annemeete Hindhede Jensen for assistance in fuel cell test of composite material. The discussions with her brought me a significant amount of trust in a field of intermediate temperature fuel cells. It was like a “light in the darkness”.

I should mention a warm gratitude to my wonderful roommate and great scientist Svava Davidsdottir who has provided me support to face both scientific and daily life challenges.

There is also a big acknowledgement to my friends PhDs Anastasia Permyakova and Antonio L. Tomas Garcia who were always supportive in the moment of need.

I should also say a couple of delightful words to Kasper Hessellund Hansen and PhD Jesper Fevre Bertelsen for their valuable consultation in Danish working culture and challenges of PhD studies.

A special acknowledgement is to Elena Ulantsikava for her rational mind which has been keeping me away from doing the rash decisions.

And finally my very warm thanks I would tell to my family, my mother Galina Viktorovna Anfimova and my son Daniil for their understanding and patience. I know, you, missed me a lot during past three years which were separating us in 1660 kilometers.

**List of publications**

***A. Papers published in international journals with reviewing***

(1) Thermal Stability and Proton Conductivity of Rare Earth Orthophosphate Hydrates, Tatiana Anfimova, Qingfeng Li, Jens Oluf Jensen, Niels Bjerrum, *International Journal of Electrochemical Science*, 9, 2285 - 2300, (2014)

(2) Indium doped niobium phosphates as intermediate temperature proton conductors, Yunjie Huang, Qingfeng Li, Tatiana Anfimova, Erik Christensen, Min Yin, Jens Oluf Jensen, Niels Bjerrum, Wei Xing, *International Journal of Hydrogen Energy*, 38 (5), 2464-2470, (2013)

(3) Conductivity of Composite Material Based on System $NdPO_4 \cdot nH_2O/CsH_2PO_4$, Tatiana Anfimova, Niels Bjerrum, Qingfeng Li, *Advanced Materials Research*, 699, 398-402, (2013)

(4) Metal Phosphates as Intermediate Temperature Proton Conducting Electrolytes, Yunjie Huang, Qingfeng Li, Chao Pan, Tatiana Anfimova, Jens Oluf Jensen, Niels *Bjerrum, E C S Transactions*, 45 (1), 99-104, (2012)

***B. Posters and oral presentation in conferences and workshops***

(5) Proton conducting composites for intermediate temperature fuel cells application, Tatiana Anfimova, Qingfeng Li, Jens Oluf Jensen, Niels Bjerrum, *Poster presented at DTU Energy Conversion PhD Symposium, Roskilde, Denmark, November (2013)*

*(6)* Preparation and conductivity of phosphate systems for intermediate temperature fuel cell and electrolyser applications, Tatiana Anfimova, *Presentation made at MEDLYS (Medium Temperature Water Electrolysers) meeting, Department of Chemistry, Technical University of Munich, Garching, Germany, October (2013)*

(6) Composite electrolyte based on $CsH_2PO_4$ with rare earth nanorods, Tatiana Anfimova, Qingfeng Li, Jens Oluf Jensen, Niels Bjerrum, *Poster and presentation made at HyFC Academy Ph.D. Workshop, DTU Lyngby Campus, Kgs. Lyngby, Denmark, June (2013)*

(7) Fabrication and characterization of proton conducting composite materials for electrolytes in intermediate temperature fuel cells and water electrolysers, Annemette Hindhede Jensen, Katrine Elsøe, Tatiana Anfimova, Erik Christensen, Jens H. Von Barner, Niels Bjerrum, *3rd CARISMA International Conference on Medium and High Temperature PEM Fuel Cells*, 75, (2012), *Poster presented at 3rd CARISMA International Conference on Medium and High Temperature Proton Exchange Membrane Fuel Cells, Copenhagen*

(8) Niobium Phosphates as Intermediate Temperature Proton Conductor, Yunjie Huang, Qingfeng Li, Chao Pan, Jens Oluf Jensen, Erik Christensen, Lars Nilausen Cleemann, Annemette Hindhede Jensen, Tatiana Anfimova, Niels Bjerrum, *3rd CARISMA International Conference on Medium and High Temperature PEM Fuel Cells*, 77, (2012) *Poster presented at 3rd CARISMA International Conference on Medium and High Temperature Proton Exchange Membrane Fuel Cells, Copenhagen*

(9) Conductivity of $NdPO_4$-$CsH_2PO_4$ composites investigated by electrochemical impedance spectroscopy, Tatiana Anfimova, Qingfeng Li, Jens Oluf Jensen, Niels Bjerrum, *3rd CARISMA International Conference on Medium and High Temperature PEM Fuel Cells*, 80, (2012) *Poster presented at 3rd CARISMA International Conference on Medium and High Temperature Proton Exchange Membrane Fuel Cells, Copenhagen*

(10) Proton Conductivity of Refractory Metal Phosphates at Intermediate Temperatures, Qingfeng Li, Yunjie Huang, Tatiana Anfimova, Jens Oluf Jensen, Erik Christensen, Niels Bjerrum *Presentation made at 16th Solid State Protonic Conductors (SSPC16), Grenoble (2012)*

(11) Conductive Properties of Neodymium Phosphate composites Investigated by Electrochemical Impedance Spectroscopy, Tatiana Anfimova, Qingfeng Li, Jens Oluf Jensen, Niels Bjerrum. *Poster presented at 16th Solid State Protonic Conductors (SSPC16), Grenoble (2012)*

(12) Rare Earth Metal Phosphates as Proton Conductors, Tatiana Anfimova, *Presentation made at PROCON Workshop, DTU Lyngby Campus, Kgs. Lyngby, Denmark, September (2012)*

(13) Proton Conductive Niobium Phosphates as Electrolytes for Fuel Cells Operating with Renewable Biofuels, Yunjie Huang, Qingfeng Li, Tatiana Anfimova, Annemette Hindhede Jensen, Jens Oluf Jensen, Erik Christensen, Niels Bjerrum *Presentation made at Pacific Rim Meeting on Electrochemical and Solid-State Science, Honolulu (2012)*

(14) Fabrication and Characterization of Proton Conducting Phosphate Electrolytes for Intermediate Temperature Fuel Cell Assembling, Annemette Hindhede Jensen, Qingfeng Li, Tatiana Anfimova, Erik Christensen, Jens H. Von Barner, Niels Bjerrum *Presentation made at Nordic Conference on Ceramic and Glass Technology, Roskilde (2012)*

(15) Solid electrolyte for intermediate temperature fuel cells, Tatiana Anfimova, *Participation in video presentation of the PhD project for the DTU Chemistry PhD School Symposium, Kgs. Lyngby, Denmark, October (2011)*, http://www.youtube.com/watch?v=eDwpcn5MmFA

(16) Phosphates of neodymium as potential electrolyte for fuel cells, Tatiana Anfimova, Qingfeng Li, Jens Oluf Jensen, Niels Bjerrum, *In Advanced Studies of Polymer Electrolyte Fuel Cells, The book of 4$^{th}$ International Summer School: book article, poster presentation, 95, Eds: S. Mitsushima, T. Araki, K. Ota, V. Hacker, M. Siebenhofer, Yokohama, Japan. Publisher: Craz University of Technology*, September (2011). ISBN: 978-3-85125-170-8

(17) Solid electrolyte for intermediate temperature fuel cells, Tatiana Anfimova,*Presentation made at PROCON Summer School, Changchun Institute of Applied Chemistry (CIAC) Chinese Academy of Sciences, Changchun, China, August (2011)*

## Table of Contents

**Symbols and abbreviations**

**Chapter 1**

*D*- diffusion coefficient
*C*- concentration
$E_a$- activation energy
$\sigma_0$- pre-exponential factor
$A_A$- cation in cation position
$A_B$- cation in anion position
$A_i$- interstitial atom
$V_A$- cation vacancy
$B_A$- anion in cation position
$B_B$- anion in anion position
*h*- electron hole
*k*- Boltzmann constant
$E_f$- enthalpy of formation
$E_d$ –enthalpies of charge carrier's diffusion
*Pt/C*- carbon supported platinum catalyst
*PCFC*- proton conductor fuel cell

**Chapter 2**

*p*- electron holes
$H_i$-hydrogen as interstitial atom
$\sigma_{tot}$-total conductivity
$R_{tot}$ – total resistance
*KDP*- potassium dihydrogen phosphate
*CDP*- cesium dihydrogen phosphate
*BZY10*- powdered $BaZr_{0,9}Y_{0,1}O_{2,9}$ prepared by solid –state reaction method.
*XRD* – X-ray diffraction
*DSC*- differential scanning calorimetry
*TGA*- thermogravimetric analyses
*DTA*- differential thermal analyses
*APP*- ammonium polyphosphate based electrolytes

**Chapter 3**

*EDX(EDS)* –X-ray energy dispersive spectroscopy
*XRD*-X-ray powdered diffraction
*PDF*-powder diffraction file

**Chapter 4**

*IS*- impedance spectroscopy
*AC*-alternating current
*DC*- direct current
*EMF*-electromotive force

*ASR*- area specific resistance
$C_{dl}$- capacitance of double layer
$X_c$- capacitive reactance
*Z*- impedance
$Z_R$- real component of impedance
$Z_i$- imaginary component of impedance
$|Z|$- absolute impedance
*CPE (Q)*- constant-phase element
$R_L$- bulk resistance of electrolyte
$C_L$- bulk capacitances of electrolyte
$R_{gb}$- grain boundary resistance of electrolyte
$C_{gb}$- grain boundary capacitances of electrolyte
$R_p$- resistance of electrode polarization processes
$\rho$- resistivity
*L*-thickness of the sample
*A* - cross-sectional area of the sample
$\sigma$ –conductivity
*I or i*- current
$\omega$- angular frequency
$\pi$ –mathematical constant
$\varphi$ –phase angle
*q*- charge
*n*- number of electrons
$Z_f$- Faradaic impedance
$k_f$- rate constant of forward reaction
$k_b$- rate constant of backward reaction
$\alpha$ –transfer coefficient
$Z_w$- Warburg impedance
*W*- Warburg element
*F*- Faraday constant
$R_{ct}$- charge transfer-resistance

**Chapter 6**

*NdP*- neodymium orthophosphate hydrate with rhabdophane type of structure
*CDP*- cesium dihydrogen phosphate

**Chapter 7**

*CA*- $Sn_{0.9}In_{0.1}P_2O_7$ phosphate prepared with oxide method
*MA*- $Sn_{0.9}In_{0.1}P_2O_7$ phosphate prepared from metal acetate precursor
*MC*- $Sn_{0.9}In_{0.1}P_2O_7$ phosphate prepared from metal chloride precursor

## List of Tables

**List of Figures**

# Chapter

# 1 Introduction

## 1.1 Hydrogen Technologies as a Solution to Energy and Environmental Challenges

There is a global push to develop a range of hydrogen technologies as an ultimate solution to the ever growing concern of energy and environmental concern in association with renewable energy sources[1]. The major renewable energy comes directly or indirectly from the sun. Solar energy can be used directly for heating, lighting and generating electricity. Heat from the sun also drives the winds, whose energy is captured by wind mills. The blow of wind and the heat of the sun cause water to evaporate and therefore rain or snow, which are the source of hydroelectric power.

Utilising electricity from solar, wind and hydro-power in a grid requires some back-up generating capacity due to the intermittent nature of these renewable energy sources. For a stand-alone power system utilising any kinds of renewable energies, a key issue is the effective energy storage technology at different time scales, from moment to moment, daily, weekly and seasonally. Water electrolysis, among others, offers a practical way of storing energy from renewable sources via hydrogen. Hydrogen and its combination with the electrochemical energy conversion technology, fuel cells, are recognized as a reliable, secure and clean energy technology in association with renewable energy sources.

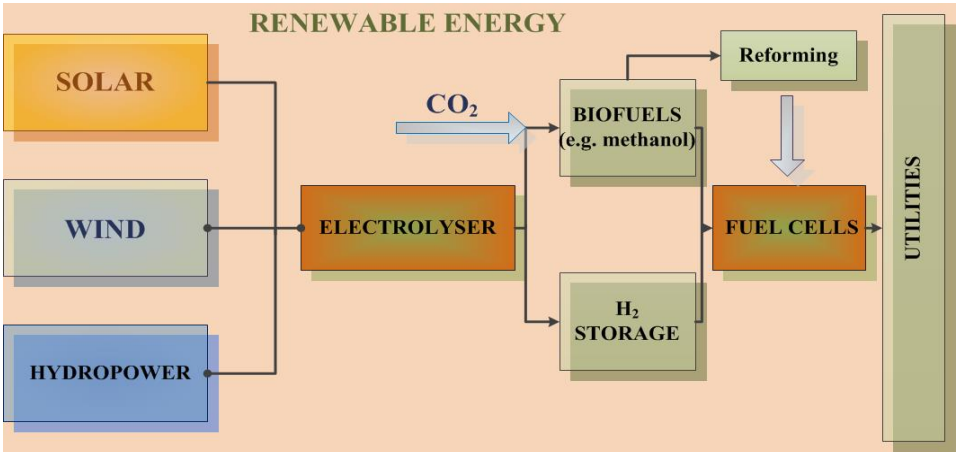


*Figure 1. 1 The power chain based on renewable energy with water electrolysers and fuel cells as the central linking technologies.*

For mobile applications, hydrogen can be further stored physically, for example, as compressed gas, liquid, or metal hydrides. An alternative way of hydrogen storage is via synthesis

of liquid biofuels e.g. methanol. Figure 1. 1 shows the power chains based on renewable energy sources with electrolyser and fuel cells as the central links.

## 1.2 Fuel Cells and Electrolysers

### 1.2.1 Principle of Fuel Cells

Fuel cells are electrochemical devices that convert the chemical energy of a fuel directly into electricity. A key material of a fuel cell is an electrolyte, which effectively separates the anode and cathode reactants and mediates the electrochemical reaction at the interface between the electrodes and the electrolyte [2]. It is the electrolyte material that defines all characteristics of fuel cell construction and operation and therefore types of fuel cells are named after the used electrolyte.

With a proton conductor as the electrolyte, a proton exchange membrane fuel cell is schematically illustrated in Figure 1. 2. No collision of the fuel (e.g. hydrogen) at the anodic side and oxygen at the cathodic side occurs owing to the separating electrolyte. Hydrogen is catalytically oxidized at the anode to give protons and electrons. Since the electrolyte is a non-electronic conductor, the electrons flow away from the anode via the external circuit to the cathode. The protons pass through the electrolyte to the cathode, where oxygen reacts with the incoming electrons and protons to produce water.

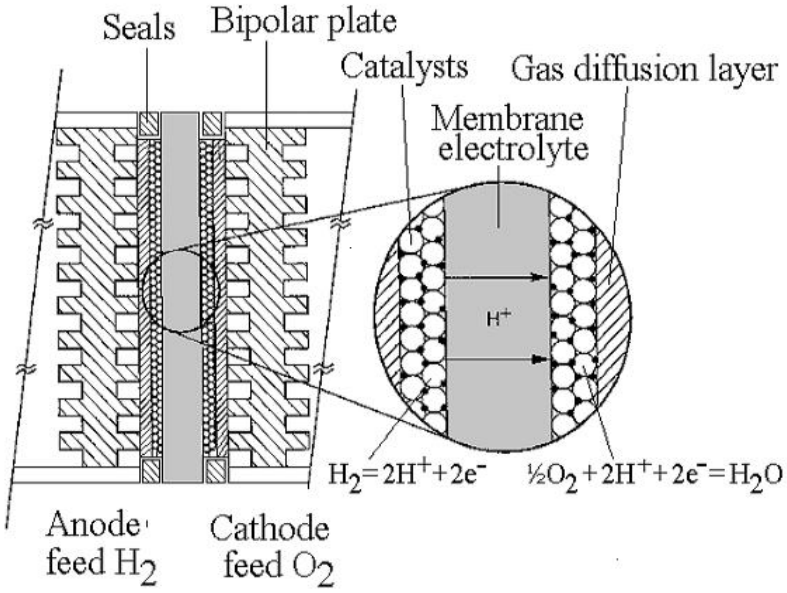


*Figure 1. 2 Schematic presentation of a PEMFC [3].*

The overall reaction of the fuel cell is the sum of the anode and cathode reactions, i.e. the combination of hydrogen and oxygen to produce water:

| | | | |
|---|---|---|---|
| Anodic: | $H_2 \longrightarrow 2H^+ + 2e^-$ | $E^0_{anode} = 0$ | *1.1* |
| Cathodic: | $½\ O_2 + 2\ e^- + 2\ H^+ \longrightarrow H_2O$ | $E^0_{cathode} = 1.229$ V | *1.2* |
| Overall: | $2\ H_2 + O_2 \longrightarrow 2\ H_2O$ | $E^0_{cell} = 1.229$ V | *1.3* |

### 1.2.2 Types of Fuel Cells

Different types of fuel cells that are currently under active development are listed in Table 1. 1, where the key materials, operating temperatures, operational features as well as historical remarks are also included.

As the key component, an ionic conducting electrolyte can be liquid acids or bases, molten salts, solid oxide ceramics or polymer membranes. In brief, phosphoric acid fuel cell (PAFC), molten carbonate fuel cells (MCFC) and alkaline fuel cells (AFC) use liquid based electrolytes. In general use of liquid electrolytes imposes issues of materials corrosion, liquid management, difficult to handle particularly in terms of storage, sealing and circulation.

Proton exchange membrane fuel cells (PEMFC) and solid oxide fuel cells (SOFC) use a solid electrolyte which is easy to handle and in general exhibiting excellent resistance to the crossover of gaseous reactants. In case of proton exchange polymer membrane, the sites responsible for proton conduction are chemically bonded to the polymer itself. In this way, issues such as sealing, interconnecting, assembling and handling are much less complex than other types of fuel cells. At expense the electrode catalysts in low temperature acidic electrolytes are noble metals, suffering from high cost and limited resources.

On the other hand, SOFC with oxide conducting ceramics, typically yttria-stabilized zirconia (YSZ) as electrolyte, operates at high temperatures in order to achieve sufficiently high oxide conductivity and power output. SOFC is of great interest especially for stationary applications, because they are able to operate directly on natural gas with high efficiency while low temperature fuel cell technologies require hydrogen as fuel. Cheap oxide catalysts are used for both anode (Ni) and cathode (e.g. oxide composite of lanthanum, strontium and manganese). Critical issues for SOFC are, however, the limited material selection for fuel cell construction. Metallic and carbon-based materials suffer from poor chemical stability in the high temperature range. As a result, ceramic materials should be used for construction such as electronically conducting interconnectors, current collectors and gas tight insulating seals. In addition, the thermal expansion coefficients of these materials should be as close to one another as possible in order to minimize thermal stresses which could lead to cracking and mechanical failure. Great efforts are being made to lower the operating temperatures down to a range of 500-600ºC to minimize these material problems.

*Table 1. 1. Comparison of different fuel cell types and their working characteristics (+ positive features; ÷ negative features).*

| Types | Electrolytes (charge carriers) | Catalysts (Anode/Cathode) | Operating temp. $^{o}C$ | Technical features | Years of research | Ref. |
|---|---|---|---|---|---|---|
| Solid Oxide Fuel Cells (SOFC) | Solid oxides ($O^{2-}$) | Ni/Perovskites | 700-900 | + Non noble metal catalyst; faster kinetics; Tolerance to fuel impurities (except sulphur); Internal fuel reforming; high heat values<br>- Slow startup; Critical selection of structural materials (compatibility); insufficient long-term durability; not mature technology | Since 1930s | [4] |
| Molten Carbonate Fuel Cell (MCFC) | Molten carbonate ($CO_3^{2-}$) | Ni/NiO | 550-650 | + Non noble metal catalyst; faster kinetics; Tolerance to fuel impurities (except sulphur); Internal fuel reforming<br>- Material corrosion and hence durability challenge; Long startup times (preheating); $CO_2$ circulation | Since late 1930s | [4] |
| Phosphoric Acid Fuel Cells (PAFC) | Concentrated $H_3PO_4$ ($H^+$) | Pt(Ru-C)/ Pt-C | 175-210 | + No water management; Fuel flexibility ($CO_2$ and CO tolerance);<br>- Slow kinetics and low power density; Noble metal catalysts; Material corrosion; lifetime issues | 1960s | [4] |
| AFC (Alkaline) | Concentrated or molten KOH ($OH^-$) | Ni(PtRu)/ Ag (Pt) | 60-220 | + Good choice of electrocatalyst; Electrolyte management (circulation); High power density<br>- Extremely intolerant to $CO_2$ (pure $H_2$ and air scrubbing); Short lifetime; Electrolyte management | Since the middle of 1960s and some work in 1940s | [4] |
| Proton exchange membrane fuel cell (PEMFC) | Perfluorinated sulfonic acid membrane ($(H_3O)^+$) | Pt-C/Pt-C | 60-80 | + Fast kinetics; High power density (portable and automotive); rapid start up<br>- Noble metal catalyst; mandatory humidification (water management); CO intolerance | Since 1960s | [4, 5, 6] |
| | Acid doped polybenzimidazole membranes ($H^+$) | Pt-C/Pt-C | 150-160 | + good CO tolerance; No humidification (water management)<br>-Noble metal catalyst; Acid leaching, slow kinetics; | Since 1995 | [7] |
| Inorganic Proton Conductor Fuel Cell (PCFC) | Phosphates ($H^+$) | Pt(WC)/Pt | 200-350 | + wide selection of structural materials; fitting biofuels (direct oxidation or via reforming); potential use of non-noble catalyst;<br>- under early development | SAFC Since 2009 | [8] |
| | Proton conducting perovskites, tungstates, pyrochlores, $LaNbO_4$ and other families | - | 500-700 | + Lower operation temperature and cost than existing SOFSc technologies<br>- poor chemical stability in $H_2O$ and $CO_2$ containing atmosphere (for perovskites doped with barium and strontium cerates) and lower power densities | - | [9, 10] |

### 1.2.3 Types of Water Electrolysers

For $H_2$ production by water electrolysis, the current dominant commercial electrolysis technology is alkaline cell systems, using KOH concentrated solution as electrolyte, and Ni-based electrode materials. Alternative electrolytic systems include Solid Oxide Electrolysis Cells (SOEC) and Proton exchange Membrane electrolyser Cells (PEMEC). For both systems, similar electrolyte materials, i.e. yttrium stabilized zirconia and perfluorinated sulfonic acid membranes e.g. Nafion®, are used. Main characteristics of different types of water electrolysers is summarized below in Table 1. 2.

*Table 1. 2 Characteristics of different water electrolysis systems [11].*

| Technology | Temperature, K | Cathode reaction | Ion carrier | Anode reaction |
|---|---|---|---|---|
| Alkaline | 333-363 | $H_2O+2e^-\rightarrow H_2+2OH^-$ | $OH^-$ | $2OH^- \rightarrow 1/2O_2+H_2O+2e^-$ |
| LT-PEM | 293-373 | $2H^++2e^-\rightarrow H_2$ | $H^+$ | $H_2O \rightarrow 1/2O_2+2H^++2e^-$ |
| SOEC | 973-1273 | $H_2O+2e^-\rightarrow H_2+O^{2-}$ | $O^{2-}$ | $O^{2-}\rightarrow 1/2O_2+2e^-$ |

In case of PEMEC, for example, the best known catalyst for hydrogen evolution is platinum while Ru and Ir oxides are the best for oxygen evolution. A relatively recent development is intermediate temperature electrolysis. It would be very advantageous to elevate the operating temperatures up to, say, above 200°C [12]. At elevated working temperatures water is in the gaseous form and the electrolysis process is thermodynamically favorable. The electrode kinetics will be enhanced and therefore the over potentials at both electrodes reduced at elevated temperatures. The heat generated inside the electrolyser is of higher value at higher temperatures and can be used for, for example, evaporation and preheating of the feeding water. On one hand, this will significantly improve the overall system efficiency. On the other, this will simplify the intensive cooling especially when operating at higher current densities. High operational pressures of 20-30 bars or higher (the saturated water vapor pressure at 200°C is 15 bars) will be another benefit, in which way the cost of subsequent gas compression will be reduced.

## 1.3 Why Intermediate Temperatures

Table 1. 1 illustrates a newly developed fuel cell technology that operates at intermediate temperatures 200-400 $^oC$ [8]. The electrolyte is currently based on two types of proton conductors: one is proton conducting phosphates and the other is represented with different families of proton conducting materials such as perovskites doped barium and strontium cerates [10], fluorite-related structures (tungstates i.e. $Ln_6WO_{12}$ [13]), fergusonites and eulytite ($Bi_4(SiO_4)_3$ and $Ba_3La(PO_4)_3$) [9] and other families [10]. The proton conducting phosphates are the subject of the current thesis and will be further discussed in Chapter 2. A driving force for developing this group of materials is the

application in lab scale PCFCs and electrolysis cells with lower operation temperatures (from 700 to 500 $^{o}$C Table 1. 1) than SOFCs based on oxygen ion conducting materials.

From fuel cell points of view this temperature range is of strategic importance for biofuels which can be directly oxidized or split to hydrogen via an integrated reformer. Electrode kinetics will be significantly enhanced so that non-noble metal catalysts might be used. Compared to liquid electrolyte fuel cells and electrolysers, these essentially solid proton conducting electrolyte membranes have numerous advantages. They are simple to handle, compact, amenable to mass production, can be fabricated into very thin films with excellent resistance to permeation of gaseous reactants. In addition, a solid composite membrane being strong and yet elastic is a major structural component in the cell. It makes the handling, sealing and assembling much easier than for fuel cells with liquid electrolytes. Moreover, it improves the pressure imbalance tolerance between half-cells.

In comparison with the solid oxide fuel cells and electrolysers, the operational temperature is much lower, allowing for a much wider materials selection for the system construction and operation. The available electrical conducting materials may include stainless steel, coated metals, graphite and carbon-composites. Non-conducting materials may include various types of thermal setting plastics, glass/ceramic fibers, and so on. Compatible thermal expansion of these materials will be much less demanding.

Compared with the PEM fuel cells and electrolysers, the cooling duty of the cell and heat recovery values will be significantly improved. The elimination of a two phase water system (liquid and vapor) will decisively simplify the system construction and operation. As a fuel cell technology, the enhanced electrode kinetics and fuel impurity tolerance will absolutely increase the fuel flexibility both for mobile and stationary uses, which can be decisive for a power system based on renewable biofuels. Most importantly, the elevated operational temperatures and enhanced electrode kinetics are expected to open the possibility for use of non-noble metal catalysts. The temperature matching of a fuel cell stack and the fuel processors makes the system integration possible. The integration is expected to give the overall power system advanced features such as higher efficiency, smaller size, lighter weight, simple construction and operation, and efficient capital and operational cost.

## 1.4 Proton Conductors as Electrolytes for Intermediate Temperature Systems

It is well recognized that the intermediate temperature range between 200-400 °C represents a technological “gap”, also termed as the “Norby gap” [14] (Figure 1. 3), which has stimulated research in this area [15]. For both fuel cells and electrolysers, the charge carriers of electrolytes should be either the product or reactant of the electrode reactions, i.e. proton ($H^+$) or oxide ($O^{2-}$) or sometime ions containing protons (as $OH^-$ in alkaline or $H_3O^+$ on Nafion ® membranes) or oxide (as $CO_3^{2-}$ in molten carbonates), in order to avoid concentration polarization at electrodes. Aiming at an intermediate temperature of operation, proton conductors seem the only candidate electrolyte materials.

As K.D Kreuer [16] pointed out, the development of proton conductor systems in this temperature range faces two main difficulties:

1) "First one arises from the fact that all compounds, for which proton conductivity has been reported so far, belong to a limited number of families of compounds with respect to the species 'solvating' the proton" [16].
2) The second problem for a further development of the available materials is, however, "limited because of the inherent properties of the species the proton conductivity is linked to; in particular, they impose constraints on the operation temperature and the chemical and electrochemical stability with other materials" [16]. "The further development of such systems for application requires the simultaneous optimization of all relevant properties for high and low temperature proton conducting materials" [16].

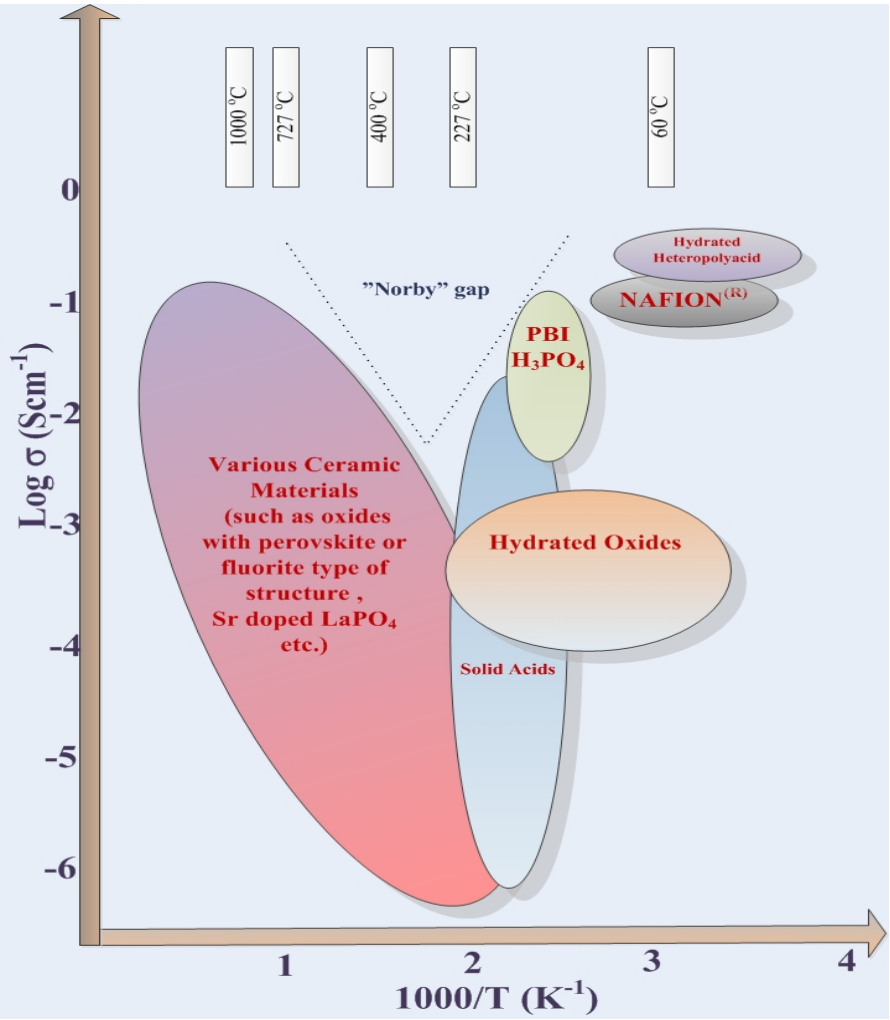


*Figure 1. 3 Selected literature data for proton conductivity as a function of inverse temperature represent so called the "Norby gap" [Data taken from ref.* [14,17,10]*].*

### 1.4.1 Proton Chemistry and Classification of Proton Conductors

The proton is the only ion that has no electron shell of its own. As a free species, in fact, a bare proton does not exist in condensed phases. Typical proton carriers include water molecules (in form of $H_3O^+$, $H_5O_2^+$), acidic molecules ($H_2SO_4^-$, $H_4PO_4^+$), ammonia ($NH_4^+$) [14] and others. The transport of protons ($H^+$) between relatively stationary host carriers is termed the Grotthuss of free-proton mechanism [14]. Transport together with any of the other species is termed a vehicle mechanism [14]. Vehicle mechanisms are most frequently encountered in aqueous solution and other liquids, melts or solid materials with open structures (channels, layers) to allow passage of the large ions and molecules (diffusion of water molecules in $SiO_2$ and many silicates; migration of $H_3O^+$ and $NH_4^+$ in β-$Al_2O_3$).

The distinction between electrical conductors and insulators is often not well defined. The conductivity can vary by more than ten orders of magnitude over a very narrow temperature range of only a few degrees. The charge carriers can be either electrons (or holes) or ions (or vacancies) and the diffusion of the matter through the solid and/or at its surface would define ionic conductivity. However, it is often that there is not a very clear distinction between bulk and surface ionic conductivity. In a densely packed structure the presence of defects can create local perturbations which facilitate the migration of ions or vacancies and enhance the conductivity.

By the Nernst-Einstein law:

$$\sigma = \frac{(DCe^2)}{kT} \qquad 1.4$$

the conductivity is proportionally dependent from the product of the concentration of the mobile species *C* (*1.5*) and the diffusion coefficient *D* (*1.6*). Both functions D and C are thermally activated and σ can be expressed as follows:

$$C = C_0 e^{\frac{-E_f}{kT}} \qquad 1.5$$

$$D = D_0 e^{\frac{-E_d}{kT}} \qquad 1.6$$

$$\sigma T = \left[\frac{(D_0 C_0 e^2)}{k}\right]\left[e^{\frac{-(E_f+E_d)}{kT}}\right] = \sigma_0 e^{\frac{-E_a}{kT}} \qquad 1.7$$

where $E_f$ and $E_d$ are enthalpies of formation and diffusion of charge carriers, respectively, $E_a$ is activation energy for conduction and $\sigma_0$ is the pre-exponential factor. Activation energy and pre-

exponential factor are important electrical characteristics of a material and can be used as a clue for suggesting possible proton conduction transfer mechanism.

$$A_A \leftrightarrow V_A + A_i \qquad 1.8$$

$$A_A + B_B \leftrightarrow A_B + B_A \qquad 1.9$$

$$0 \leftrightarrow V_A + V_B \qquad 1.10$$

$$V_A^{\times} \leftrightarrow V_A' + h^{\bullet} \qquad 1.11$$

In a simple AB crystal structure may present following type types of point defects (Figure 1. 4) such as a Frenkel defect (equation 1.8 and Figure 1. 4 (3)), anti-structure defect (equation 1.9 Figure 1. 4 (6)) or Schottky defect (equation 1.10 Figure 1. 4 (1,2)) and others. Such defects can have effective charge which is usually expressed as positive (•), negative (′) or neutral (×) (equation 1.11).

As represented (Figure 1. 4), the defect mechanisms even for simple compounds such as halides, sulphides, oxides and other similar materials has a very complex nature. In case of compounds consisting from more than two types of atoms a process of defect formation is getting more complicated for understanding due to association of point defects, formation of dislocations and existing of three dimensional defects. However, formation of defects can facilitate proton conduction transfer for some of solid proton conductors.

Glassy materials are usually poorer conductors and have higher activation energies than crystalline materials [18]. It must be noticed that other laws than the Nernst-Einstein law (1.4) are often used for estimation of electrical properties of glasses and polymers.

The presence or absence of hydrogen bonds, crystal structure, possible proton transfer or ion exchange properties and other electrical and material characteristics can be used to classify proton conductors. Colomban [18], among others, distinguished following types of proton conducting materials:

*Anhydrous proton conductors*. The conductivity behavior of this family is similar to alkali halides (Ionic conductor in Figure 1. 5) with high values of activation energies and proton conduction related to the presence of different types of defects. The $KH_2PO_4$ is an example of such proton conductor (Table 1. 3) and its main proton transfer mechanism behavior is by defects (Figure 1. 4).

*Ionic conductors* containing a loosely packed lattice (Figure 1. 4 right) have a high concentration of potentially mobile species. Such materials have high values of total conductivity and activation energy at low temperatures but with a rise of temperature activation energies may decrease (Figure 1. 5). The conducting species are different ions such as $H_3O^+$ or $NH_4^+$.

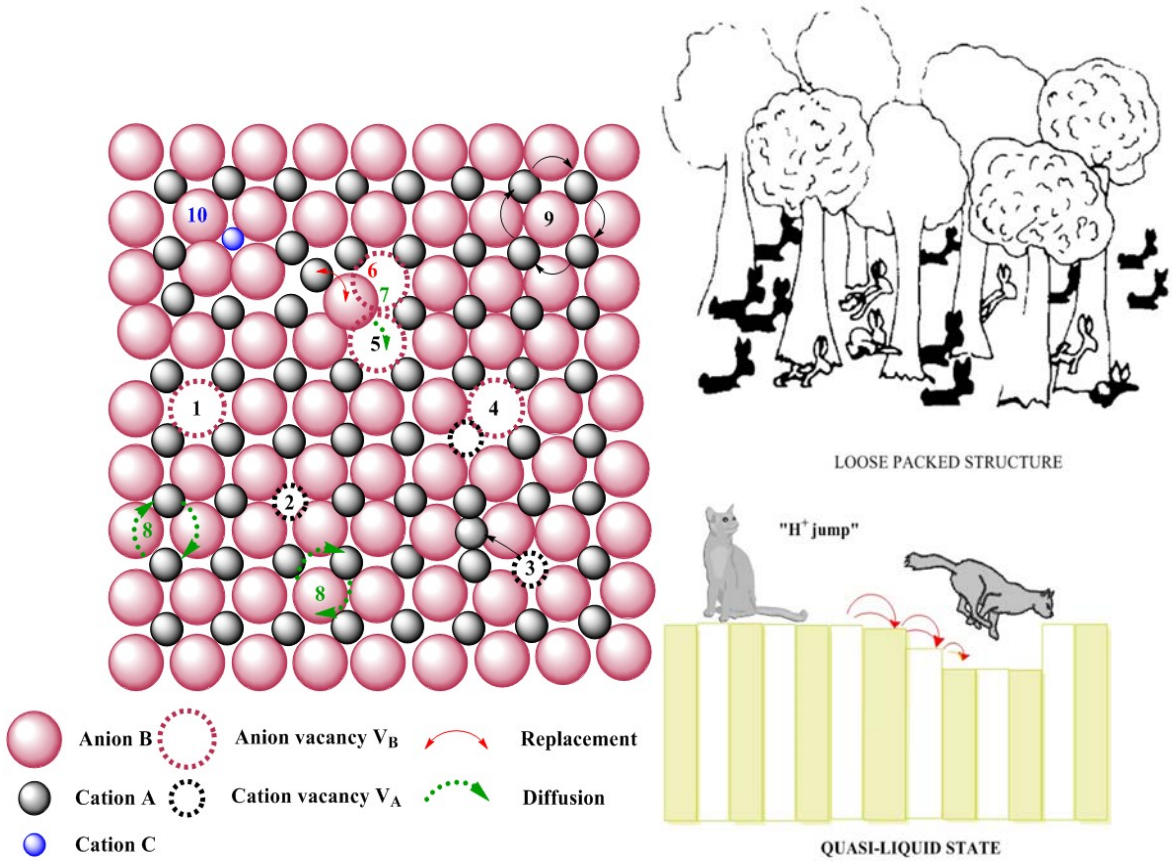


(a) (b)

*Figure 1. 4(a) formation of point defects, dislocations, diffusion mechanisms in chemical compound with formula AB: 1,2-Schottky defect; 3- Frenkel defect (interstitial); 4,5 - divacancy (association of point defects and formation of dislocation) ; 6- antistructural defect;7-diffusion mechanisms through vacancy; 8-diffusion mechanism by direct echange; 9-indirect exchange; 10-replacement of cation A by heterovalent cation C. (b) Illustration of three main proton transfer mechanisms: Defect mechanisms (a), Loose packed structure [*[18]*], Quasi-liquid state (surface).*

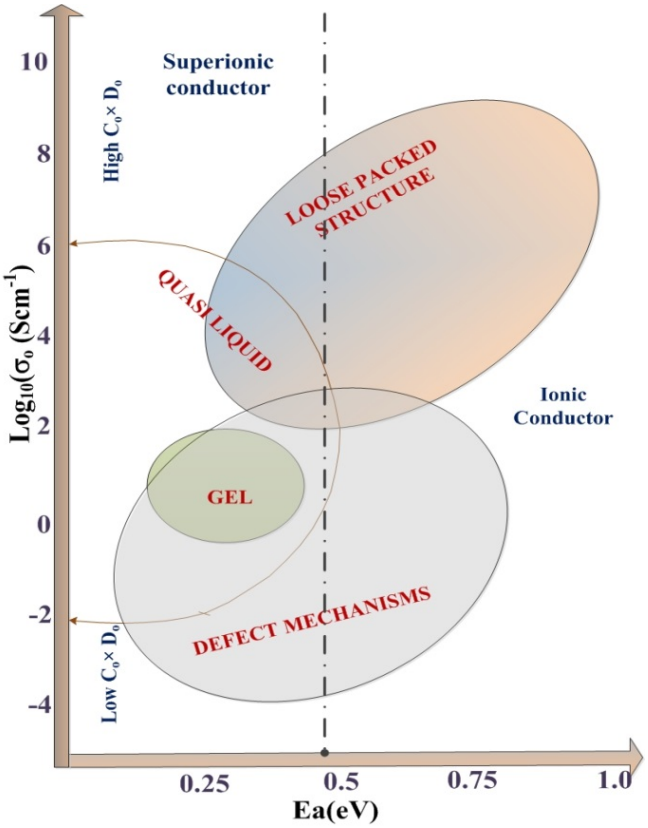


*Figure 1. 5 Schematic representation of relationship between the pre-exponential factor $\sigma_0$ and the activation energy $E_a$ for solid protonic conductors. (Inspired by data from ref. [[18]]).*

The third family of compounds characterized by the presence of protonic species in a *quasi-liquid state* Figure 1. 4 (right). The quasi-liquid state is a very complex proton transfer mechanism. The main difficulty is that such state can exist as inside the structure (in this case conductor will be bulk or intrinsic $H_3OUO_2PO_4 \cdot 3H_2O$, Table 1. 3) or at the surface (in case of gels like $V_2O_5 \cdot nH_2O$ or particle hydrates $Ce(HPO_4)_2 \cdot nH_2O$, Table 1. 3). "Various mobile species can move using different paths at different rates and some, such as proton, may jump from one to the other"[[18]]. The quasi-liquid state is more often characterized by "proton jump" or the Grotthuss mechanism.

Table 1. 3 lists proton conducting materials with different mechanisms of conduction in connection with their activation energy. Values of the activation energy (see also Figure 1. 5) can give a clue about the possible proton transfer. However in the range of activation energies between 0.4-0.6 eV there is a possibility to meet several mechanisms at the same time or changing mechanism with temperature as there are no certain criteria of distinguishing one mechanism from another.

The interesting feature which can be observed in hydrates is that with increasing number of water molecules in structures the conductivity seems to increase as well even at room temperature. One example is $Ce(HPO_4)_2 \cdot nH_2O$. As seen from Table 1. 3 with a surface quasi liquid proton conduction mechanism its conductivity is found to be dependent on the number of water molecules, n. For n =1.2 the conductivity is as low as $10^{-6}$ Scm$^{-1}$ while it becomes $2 \times 10^{-4}$ when n = 3.8.

## 1 Introduction

Classification of proton conductors generally helps to estimate possible mechanisms of proton conduction but cannot be used to find the best proton conductors as certain properties of a "good" proton conductor depend on application. Various types of electrochemical cells put restrictions for an applied electrolyte which limit the choice of possible candidates. For development of PCFC electrolyte it still remains a main challenge, even though the significant step was made by developing of the first type of solid acid fuel cell in 2009 [8].

The task of defining suitable materials is more complicated as the known "good" proton conductors belong to different "families" of materials. Some proton conductors have several mechanisms of conduction which act simultaneously (Figure 1. 5 and Table 1. 3) in the same material. This makes studies of proton conductivity a rather difficult task which is required extensive knowledge of different properties of studied materials.

In the family of phosphate proton conductors, three types of conduction mechanisms are possible to meet. This makes phosphates one of interesting candidates for future applications as an electrolyte in intermediate temperature fuel cells.

*Table 1. 3 Conductivity, activation energy $E_a$ and possible mechanisms of proton transfer for different families of proton conductors.*

| Name | Mechanism (assumed Fig.2 and Fig.3) | Conductivity $Scm^{-1}$ | Temp., K | $E_a$, eV | References |
|---|---|---|---|---|---|
| $NH_4H_2PO_4$ | Defect mechanisms | $10^{-8}$ | RT | 0.48 | [18] |
| $KH_2PO_4$ | Defect mechanisms | $10^{-8}$ | RT | 0.55 | [19] |
| $CsH_2PO_4$ | $H^+$ jump and free rotation | $10^{-7}$ | RT | 1 | [20] |
| | Superprotonic phase | $10^{-2}$ | 505 K | 0.3 | [20] |
| $CaHPO_4•2H_2O$ | $H^+$ jump and free rotation | $10^{-3}$ | 600 K | - | [18] |
| $HZr_2(PO_4)_3$ | Surface acidic conductivity of $H^+(H_2O)_n$ and ion jump | $10^{-7}$ | RT | 0.44 | [18] |
| $Ce(HPO_4)_2 \cdot 1.2\ H_2O$ | Surface (Quasi-liquid state) | $10^{-6}$ | RT | 0.45 | [21] |

| | | | | | |
|---|---|---|---|---|---|
| $Ce(HPO_4)_2 \cdot 3.8H_2O$ | Surface (Quasi-liquid state) | $2\times10^{-4}$ | RT | 0.17 | [22] |
| $V_2O_5 \cdot 0.5H_2O$ | Surface (Quasi-liquid state) Three dimensions | $5\times10^{-5}$ | RT | 0.42 | [23] |
| $V_2O_5 \cdot 1.6H_2O$ | Surface (Quasi-liquid state) Three dimensions | $3\times10^{-3}$ | RT | 0.35 | [23] |
| $H_3OUO_2PO_4 \cdot 3H_2O$ (uranyl phosphate) | Quasi-liquid state (intrinsic) | $1,3\times10^{-4}$ | RT | 0,35 | [24] |
| $HSbO_3 \cdot 0,5H_2O$ (cubic) | - | $9\times10^{-4}$ | RT | 0.39 | [25] |
| $HSbO_3 \cdot 1\text{-}2H_2O$ (pyrochlore) | Gel | $3\times10^{-3}$ | RT | 0.20 | [25] |
| $HSbO_3 \cdot 1\text{-}2.5H_2O$ (Layer-ilmenite) | Gel | $2\times10^{-3}$ | RT | 0.19 | [25] |
| $HNbO_3$ | Defect mechanisms | $5\times10^{-8}$ | RT | 0.20 | [26] |
| $HNbO_3 \cdot 0,4H_2O$ | Surface (Quasi-liquid state) | $10^{-4}$ | RT | 0.21 | [26] |

## 1.5 Scope of the thesis

The present thesis is devoted to investigation of a few selected phosphates as proton conductors for applications in intermediate temperature fuel cell and electrolyser technologies which are rare earth metal phosphates, alkali dihydrogen phosphates and indium doped tin pyrophosphate. In Chapter 2, a comprehensive literature survey is made on these phosphates.

After introduction to the experimental techniques (chapters 3 and 4), the stability and conductivity of rare earth metal phosphate hydrates is first presented in Chapter 5. In Chapter 6 the

conductivity and properties of composites of rare earth metal phosphate and cesium dihydrogen phosphate are reported.

Chapter 7 is devoted to an investigation of possible mechanisms of conductivity of indium doped tin pyrophosphates

In Chapter 8 the cerium ultraphosphate is discussed in relation to its conductivity and structural difference from orthophosphates from Chapter 5.

# Chapter

# 2 Phosphates as proton conductors

## 2.1 Why phosphates?

The research is focusing on ionic conducting materials in the intermediate temperature range from 200 to 400 $^{o}$C. This temperature range is an essential measure for selection of possible ionic conducting materials. As an electrolyte for fuel cells and electrolysers at such operational temperatures, the most favorable materials are proton conductors. From technological points of view, requirements for the proton conducting materials include:

- Proton conductivity higher than $>10^{-2}$ $Scm^{-1}$, most preferably under low water partials pressure or even anhydrous condition;
- Good electronic insulation to prevent any short circuit in the cell;
- High stability against chemical, thermal and electrochemical attacks particularly in the presence of water vapor;
- Ability to form thin films with strong mechanical strength, low porosity and therefore low gas permeation;
- Being easy to handle and process;
- High compatibility with other cell components such as electrodes, seals, current collectors;
- And low cost and wide availability of the materials

These considerations have limited the candidate materials to a very few and phosphates are one of the systems that have received most attention. Several review articles were published only about this particular family [17,27,28].

As a comparison, for example, sulfate based proton conductors such as alkali metal hydrogen sulfates have a limited operational temperatures by the thermal decomposition of the $SO_4^{2-}$ ions above 200 $^{o}$ C [29] as well as the chemical instability in hydrogen containing atmosphere.

Phosphates are a big family of salts of orthophosphoric acid and its condensed/polymeric forms. The anions are comprised of pentavalent phosphorus atoms surrounded by (distorted) tetrahedra of four oxygen atoms. Monophosphates or orthophosphates are the biggest group with an isolated anionic entity of $PO_4^{3-}$ tetrahedron while condensed phosphates are another containing corner-sharing $PO_4$ tetrahedra. Variations of the family materials also include gels [30,31] and glasses, for example, $P_2O_5$- $SiO_2$- $MO_2$ (where M is a tetravalent cation such as Zr, Ti, etc) [32,33,34,35]. In the following, more discussions are made for four major types of phosphates, acidic

phosphates (or solid acids), pyrophosphates, rare earth orthophosphates, and briefly ammonium polyphosphates, based on which the thesis work is carried out.

## 2.2 Phosphate based solid acids

Solid acid compounds exhibit properties which lie between those of a normal acid and a salt and consist usually of an alkali metal (or $NH_4$) and tetrahedral oxyanions linked together by hydrogen bonds. The general formula (*2.1*) of solid acids can be expressed as:

$$M_xH_y(AO_4)_z, \qquad (M = Li, K, Rb, Cs, NH_4; A = S, Se, P, As) \qquad 2.1$$

The proton conductivity of such compounds at ambient temperature is low but above certain temperatures, the proton conductivity is increased by several orders of magnitude. For caesium hydrogen sulfates, for example, at temperatures above around 130 $^oC$ (depending on the material), the material undergoes a structural change to a high temperature stable superprotonic phase where the conductivity is increased from $10^{-7}$ to $10^{-2}$ $Scm^{-1}$. This phenomenon, as called the superprotonic state, is typical for this type of solid acids. Here below the discussion is devoted to alkali metal dihydrogen phosphates.

Some of alkali solid acids also known as monophosphates (or orthophosphates) and by definition their anionic entity $[PO_4]^{3-}$ is composed by an regular tetrahedral arrangement of four oxygen atoms centered by a phosphorous atom [36]. The family of monophosphates is the largest in number of phosphate systems and this is easily explained by stability of these phosphates comparing to condensed phosphate's families (salts containing condensed phosphoric anions). The phosphorous anion containing P-O-P bonds is sensitive to hydrolysis and can be broken with final products always consisting of monophosphate or a mixture of monophosphates. It is important to say that rare earth metal phosphates hydrates which will be discussed in Chapter 5 also belong to the same family of monophosphates. In spite of rather simple geometry the monophosphates have very complicated structures which are often difficult to explain and represent [36] .

The thermal behavior of solid acids $M^IH_2PO_4$ is very complex and depends on the degree of acidity of the $M^I$ anions. Table 2. 1 represents data of thermal transitions together with literature references. The final reaction can be expressed as 2.2.

$$M^IH_2PO_4 \rightarrow M^IPO_3 + H_2O \qquad 2.2$$

As seen from equation 2.2 and Table 2. 1 the final product is always long-chain polyphosphate $M^IPO_3$ but intermediate steps can be different from one cation to another. These steps found to be dependent on conditions of surrounding atmosphere (humidity content). For some compounds there are differences depending on heating steps. For example $NaH_2PO_4$, which after relatively fast heating 550 $^oC$ gives $NaPO_3$, and if heated during 5 hours gives $Na_3P_3O_9$. The

behavior of solid acids mixtures with rare earth metal phosphates very much depends on the behavior of solid acid itself.

*Table 2. 1 Important phase transitions, formation of long chain polyphosphates and their related temperatures reported in literature for $M^{I}H_2PO_4$*

| Name | Tempreture, $^{o}C$ (atmospheric conditions) | Suggested process | Literature reference |
|---|---|---|---|
| $LiH_2PO_4$ | 350 (during 30 min) | Formation of $LiPO_3$ | [36] |
| $NaH_2PO_4$ | 200 -240 | Formation of $Na_2H_2P_2O_7$ | [36] |
| | 550 | Formation of $NaPO_3$ (polymer) | [36] |
| | 550 (5 hours) | Formation of $Na_3P_3O_9$ (trimer) | [36] |
| $KH_2PO_4$ | 252 | Melting of $KH_2PO_4$ | [36] |
| | 258 -510 | Formation of Kurrol salt $K_nH_2P_nO_{3n+1}$ | [19] |
| $RbH_2PO_4$ | 130 | Transition from tetragonal to monoclinic phase | [37] |
| | 255-280 | Formation and existence of $Rb_2H_2P_2O_7$ | [37] |
| | 280-810 | Decomposition of $Rb_nH_2P_nO_{3n+1}$($n >>1$ ) to $(RbPO_3)_n$ | [37] |
| | 810 | Melting of $(RbPO_3)_n$ | [37] |
| $CsH_2PO_4$ | 228 | Phase transition from paraelectric phase to superprotonic phase | [38] |
| | 233-263 (dry conditions) | Formation and existence of $Cs_2H_2P_2O_7$ | [38] |
| | Above 260 (Humidified conditions) | Formation and existence $CsH_{2(1-x)}PO_{4-x} \rightarrow CsH_{2(1-y)}PO_{4-y} \rightarrow CsPO_3$ $x \leq 0.4$, $0.4 \leq y \leq 1$ where x and y depend from humidity | [39] |
| | 345 | Melting of $CsH_2PO_4$ | [40] |
| | 735 | Melting of $CsPO_3$ | [39] |

### 2.2.1 Phase and structure relations of $KH_2PO_4$ and $CsH_2PO_4$

Potassium dihydrogen phosphate $KH_2PO_4$ (also referred to as KDP) and $CsH_2PO_4$ (also referred to as CDP) are two well-studied compounds in the family of solid acids.

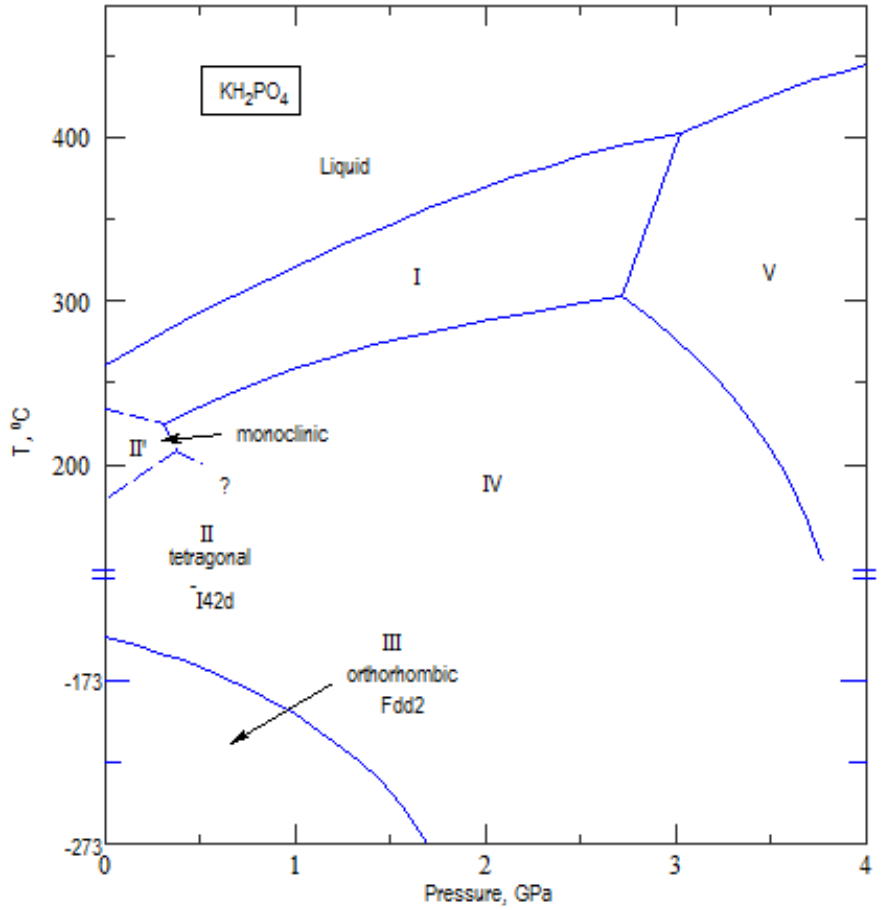


*Figure 2. 1 The pressure-temperature phase diagram of $KH_2PO_4$ built by Phase Equilibria Database based on data taken from ref. [41].*

**$KH_2PO_4$**

Structure and proton conductivity of KDP are widely discussed in literature [37,42,43,44,45] for its interesting electro-optical and dielectric properties. The complete phase diagram for KDP is shown in Figure 2. 1. The conductivity of KDP increases rapidly at a constant temperature 220 °C until the dehydration according to equation (2.3) starts. The long chain potassium polyphosphate is formed between 258 °C and 510 °C (also known in literature as the Kurrol's salt [19], see equation (2.3), which then undergoes several transitions at temperatures around 510 °C [46].

$$nKH_2PO_{4(s)} \rightarrow K_nH_2P_nO_{3n+1(s)} + (n-1)H_2O_{(v)} \qquad 2.3$$

It is interesting to point out that KDP has common features with ice as well as another proton conductor hydrogen uranil phosphate (see Chapter 1, Table 1. 3 ). According to the Bjerrum theory [18] an occurrence of doubly occupied sites (Doppelsetzung, D) and/or empty sites (Lehrstehle, L) in ice has been postulated [47] and it is the simplest model for translocation, which is known as the lone migration mechanism. In the presence of L defects the displacement of $H^+$ ions along a hydrogen bond can occur with following transport of such ions from one hydrogen bond to another. Four types of translocation mechanism has been proposed so far [18]. The possible existence of L defects have not been confirmed or disproved by the present knowledge for solid acids, however, a statistical dynamic disorder of $H^+$ sites in $CsDSO_4$ (and most likely in other solid acids such as $CsH_2PO_4$) leads to a quasi-liquid proton sublattice and promotes the formation of L and D defects.

**$CsH_2PO_4$**

For $CsH_2PO_4$ at the atmospheric pressure and temperatures higher than room temperatures studies revealed that there are two phase transitions. At room temperature CDP exists in the monoclinic phase III. A quasi irreversible transition from the monoclinic phase to the phase II is found at 149 $^oC$ [41] and the second reversible transition occurred at 230 $^oC$ [41], where the phase II is transferred into the cubic phase I. The cubic phase I is also known as the superprotonic phase and it has been confirmed using X-Ray Powder Diffraction (XRD), Differential Scanning Calorimmetry (DSC) and Thermogravimetric Analysis (TGA) [17].

In the monoclinic phase III the phosphate groups are linked together with hydrogen bonds of two different kinds: symmetric double minima and asymmetric single minimum [28]. The hydrogen network where $PO_4^{3-}$ anions are linked via O-H•••O bonds at all corners of the phosphate tetrahedra, forms two dimensional $[H_2(PO_4)^-]_\infty$ layers. Cesium cations reside at sites between these layers [28].

In the superprotonic phase I, the lattice becomes cubic (a CsCl-like structure) with the oxyanion placed in the center of a cube with Cs atoms on each corner. The oxyanion can take one of six possible orientations within the cube and therefore there are six possible ways that hydrogen bonds can be formed [28,48]. The melting point of CDP is about 345 $^oC$. Such a solid acid is of high interest for intermediate temperature electrolysis and fuel cell applications. Under dry conditions, dehydration occurred at temperatures above 200 $^oC$ according to reaction:

$$CsH_2PO_4 \rightarrow Cs_2H_2P_2O_7 \rightarrow CsPO_3 \qquad 2.4$$

From reaction (2.4) a total weight loss of 7.83% is expected for the complete dehydration. Thermal behaviors with the two-step mass loss and thermal event in the temperature range from 200 to 300 $^oC$ have been well described by Boysen et al. [49] and Taninouchi et al. [39]

This dehydration process which occurs at the same time with the second phase transition produced a lot of disagreements in the early literature, which have been clarified by Haile et al. [28], as to be discussed below.

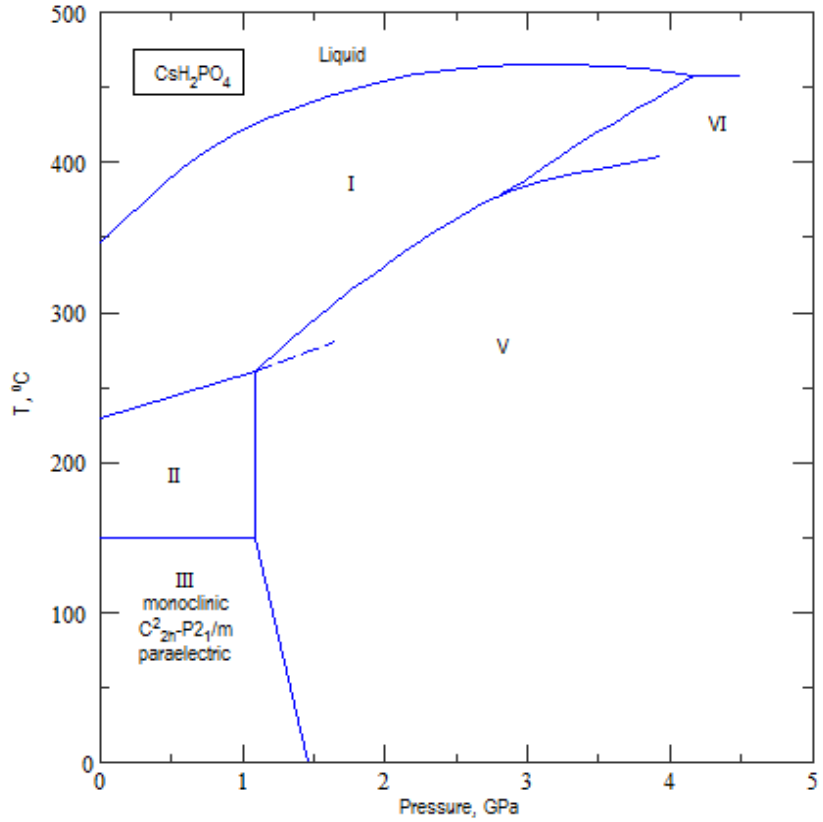


*Figure 2. 2. The pressure-temperature phase diagram of $CsH_2PO_4$ built by Phase Equilibria Database based on data taken from ref. [41].*

### 2.2.2 Conductivity of $CsH_2PO_4$

Cesium dihydrogen phosphate, $CsH_2PO_4$ or CDP, has received attention because of its high-temperature proton transport properties [17,27]. It is one of the most well studied compounds of solid acids. Several authors have investigated the high temperature structural and/or transport properties of $CsH_2PO_4$ as well reviewed recently by Haile et al. [28] The possibility to use $CsH_2PO_4$ as electrolyte for fuel cells was first demonstrated by Haile et al. in 2004 [50] and later confirmed by Otomo et al. in 2005 [51].

The conductivity measurements have been performed by two point ac impedance spectroscopy under humidified conditions by several authors [52,51]. Otomo [51] studied at temperatures from 150 to 250 °C and $P_{H2O}$ = 0.4 atm) the polycrystalline powder of $CsH_2PO_4$ as

presented in Figure 2. 3(a). Measuring conductivity under humidified conditions is important in order to suppress the dehydration process (*2.4*). The high temperature cubic phase exists from the transition temperature of ~223 $^{o}$C up to the highest measured temperature of 254 $^{o}$C and the conductivity increases from $8.5\times10^{-6}$ S/cm at 223 $^{o}$C to $1.8\times10^{-2}$ S/cm at 254 $^{o}$C. The reported activation energy of this process is 0.42 eV. Figure 2. 3(a) shows differences in conductivity values measured at first and second heating cycles, which is explained by the surface water present in the grain boundary regions of the polycrystalline sample.

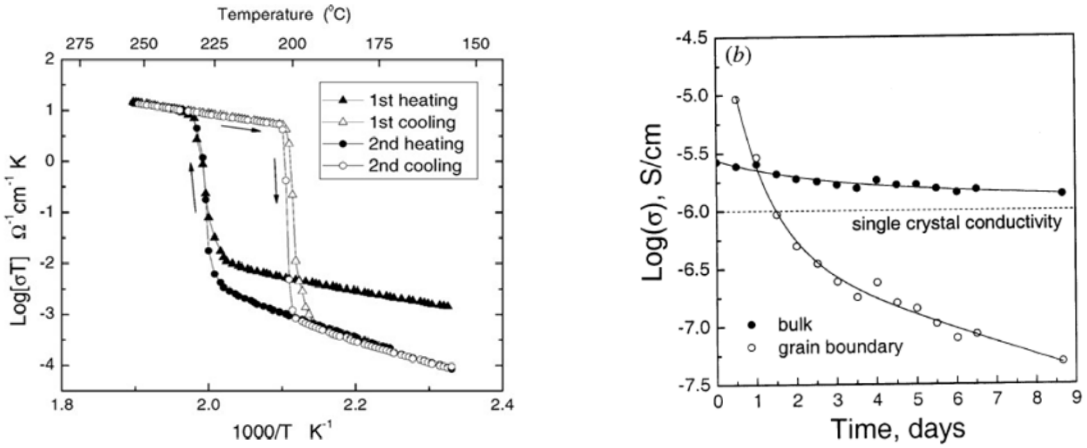


*Figure 2. 3. a)Conductivity of polycrystalline $CsH_2PO_4$ under humidified air ($p(H_2O)$=0,4 atm.) for two cycles [*[51]*] b) Influence of grain boundary conductivity: bulk and grain boundary conductivities as a function of time [*[52]*]*

The influence of the surface water is found to be difficult to remove and affects not only the grain boundary conductivity but also the impedance arc associated with the bulk conductivity [[52]]. Figure 2. 3(b) shows the conductivity of the single crystal and polycrystalline powder as a function of time, suggesting that both grain boundary and bulk conductivity decreases with time.

The influence of the chemisorbed surface water gives an increase of values of conductivity by about two orders of magnitude for the polycrystalline sample $CsH_2PO_4$. Materials such as $Zr(HPO_4)_2$ (see 1.4.3), in both hydrated and anhydrous forms, are known to show a somewhat similar humidity dependence in their transport behavior due to the adsorbed water between the layers of the highly layered crystal structure [[52]].

Unlike other known solid proton conductors, the conductivity of the superprotonic solid acid salts is an intrinsic property of the crystal lattice and it does not result from defects or impurities[[53]]. The contradictory of the high protonic conductivity and chemical stability in a very narrow temperature range has stimulated great efforts to further develop composites materials based on the cesium dihydrogen phosphate.

### 2.2.3 $CsH_2PO_4$ based composites

A challenge for the pure $CsH_2PO_4$ as electrolyte is the very narrow temperature range of the superprotonic phase from 230 to 250 $^oC$. Below this range the conductivity is very low while the chemical stability, mechanical strength and integrity, as well as the long term durability of CDP are of concern at temperatures higher than this range. To address this challenge, heterogeneous doping of the solid acid has been extensively explored.

The dopant materials include inorganic oxides ($SiO_2$, $ZrO_2$), metal phosphates [54] or heteropolyacids (HPAs) [55]. Table 2. 2 lists the investigated composite materials with their temperature ranges of conductivity and suggested mechanisms of conduction.

*Table 2. 2.Typical values of conductivity for composite materials based on cesium dihydrogen phosphate.*

| Composite material | Temperature range, $^oC$ | Conductivity range, $Scm^{-1}$ | Mechanism | Reference |
|---|---|---|---|---|
| $CsH_2SO_4/Al_2O_3;TiO_2$ $CsH_2PO_4/SiO_2$ | 40-200 | $10^{-5}$-$10^{-2.5}$ | Strong interface interaction and $Cs_2H_2P_2O_7$ formation | [17, 53, 56, 57, 58] |
| $CsH_5(PO_4)_2/SiP_2O_7$ | 100-300 | $10^{-5}$-$10^{-0.8}$ | $CsH_5(PO_4)_2$ responsible for the high conductivity | [54, 59, 60] |
| $CsH_2PO_4/ZrO_2$ | 20-270 | $10^{-7}$-$10^{-2}$ | - | [61] |
| $CsH_2PO_4/SrZrO_3$ | 40-230 | $10^{-5}$-$10^{-2}$ | Structural disordering and amorphization of the salt | [62] |
| $CsH_2PO_4$/Anodic alumina membranes | Room temperature | Fuel cell test $10^{-4}$-$10^{-3}$ at room temperature | Possibility of thin films and chemisorbed $H_2O$ in the grain boundary | [63] |
| $CsH_2PO_4$/Heteropolyacids (HPA, WPA) | 60-180 | $10^{-8}$-$10^{-3}$ | Form $Cs_xH_{3-x}PW_{12}O_{40}$ conductive at lower temperatures | [64, 55] |
| $CsH_2PO_4/C_5H_5N_5O$ | 80-260 | $10^{-8}$-$10^{-2}$ | Tautomerism of guanine after mechanochemical treatment influenced by highly acidic environment | [65, 66] |

In case of CDP/$SiO_2$ composites Otomo et al. [56] observed a large asymmetric thermal hysteresis in the conductivity, i.e. the conductivity in the cooling process maintains relatively high values as compared to that of the heating process. This was attributed to the significant supercooling of the cubic phase of CDP as induced by the inclusion of the oxides in the composites. In other words, as the authors assumed, the composite oxides induced shear elastic forces and orientational disorders of the $H_2PO_4^-$ anion and therefore improved conductivity at temperatures below the superprotic transition point.

Similarly Lavrova et al. reported a composite material of CDP with the perovskite-like $SrZrO_3$ [62]. By the introduction of 1-20 mol% of the highly dispersed strontium zirconate, they found an increase in the low temperature conductivity by 1-3 orders of magnitude. With no observation of any chemical interaction or new compound formation between the components, the increased conductivity was attributed to the salt disordering due to the interphase surface interaction.

Matsui et al. [54] prepared a composite of CDP and $SiP_2O_7$, which exhibited a higher composite conductivity than the pure CDP. The authors proved that the CDP chemically reacts with the $SiP_2O_7$ matrix at the contacting interface during the heat treatment, forming a new conducting phase of $CsH_5(PO_4)_2$ [67]. The compound $CsH_5(PO_4)_2$ was found to have a melting point at around 150 °C and form a pseudo liquid layer at the grain boundaries.

Interestingly Matsuda et al. [64] introduced phosphotungstic acid ($H_3PW_{12}O_{40} \bullet nH_2O$, WPA) into the CDP by mechanochemical milling. A conductivity of $6.6\times10^{-4}$ S/cm was achieved for a composite containing 5 mol% WPA at 170 $^oC$ under anhydrous conditions. This conductivity is significantly higher than the value for either pure CDP or pure WPA under the same condition. The authors proposed a mechanism of the developed hydrogen or acid-base interaction between the two components of the composite. More hints of the acid-base interaction were obtained by Matsuda et al. who recently prepared composites of CDP with organic bases such as Guanine and its tautomers [66], as well as azoles, though with $CsHSO_4$ as the inorganic acidic phase [66]. The composites, again, showed significantly higher proton conductivity than that of either CDP or the small organic molecules in their pure form under both hydrous and anhydrous conditions. The increase in conductivity was especially remarkable in the temperature region below the superprotic transition.

### 2.2.4 New type of fuel cell based on $CsH_2PO_4$

High protonic conductivity of $CsH_2PO_4$ in the superprotonic state has made this material an interesting candidate for application in intermediate temperature fuel cells.

The 25 μm thin membrane has been fabricated according to scheme presented in Figure 2. 4 (a), based on which fuel cells was assembled and tested. The single cell demonstrated a power density around 415 $mW/cm^2$ at the peak power. Such a performance is comparable with commercially available phosphoric acid fuel cells [28]. The electrodes were made of a composite mixture of cesium dihydrogen phosphate, Pt black and Pt supported on carbon.

In 2009 a fuel stack (see Figure 2. 4 (b)) was demonstrated by Haile et al. [8] Using the mechanically mixed composite electrodes the solid acid fuel cell (SAFC) reached peak power densities of 180 mW/cm$^2$ under operation at 250 $^o$C on hydrogen/air at ambient pressures.

A few remarks on operation of the SAFCs can be made as following:

- The control system must heat the stack above the phase transition temperature (~230 $^o$C) (below this point the stack is not operable due to low conductivity of MEA).

-The water generated in the stack at high temperatures is in the vapor form.

-Both cathode and anode gas streams must be humidified for safe operation of the stack (due to possible dehydration of electrolyte).

(a)

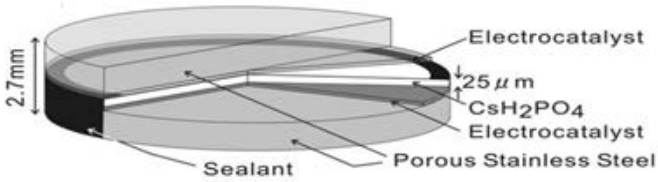


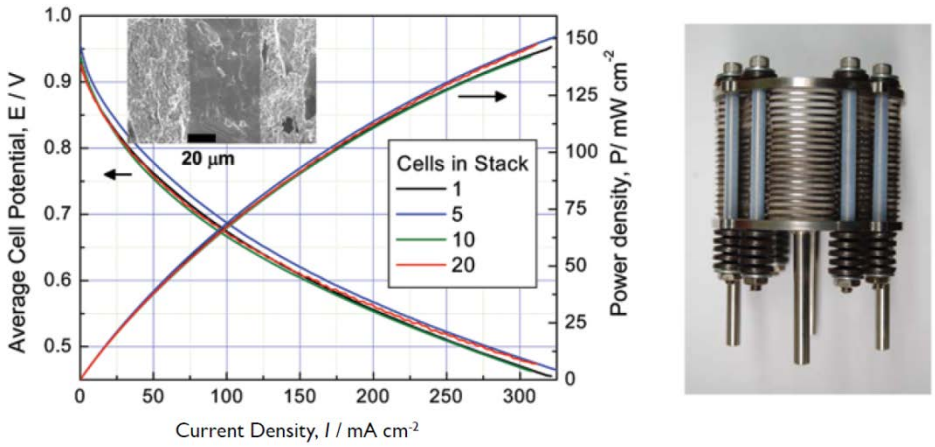


(b)

*Figure 2. 4 a)Schematic presentation of thin film cell[28]; b)Fuel cell polarization and power density curves for SAFC stacks with inset showing scanning electron microscope image of a typical MEA and a 50W net stack constructed from such MEA [8].*

## 2.3 $SnP_2O_7$ and other pyrophosphates.

$SnP_2O_7$ is a member of the $ZrP_2O_7$ family of materials, several of which show unusual thermal expansion behavior over certain temperature ranges. The structure of $SnP_2O_7$ phase was initially thought to have the simple cubic structure presenting in Figure 2. 5, where $PO_4$ tetrahedra sharing one corner to form $P_2O_7$ units (Figure 2. 5b). Later it has been demonstrated that the $SnP_2O_7$ phase undergoes a series of reversible phase transitions on heating and cooling and has a structure that differs from other members of this family [68]. The principal driving force for these phase

transitions can be considered to be the bending of P-O-P bonds of $P_2O_7$ groups, which are required by symmetry to be 180° in the high-temperature structure.

Japanese researchers are leading in development metal pyrophosphates ($MP_2O_7$, M=Sn, Ti, Si, Ge, Ce and Zr) [69,70,71,72,73] and composites based on these systems [54, 74] (see Figure 2. 6a). A review article about pyrophosphate systems has been written by Hibino [75] in 2011.

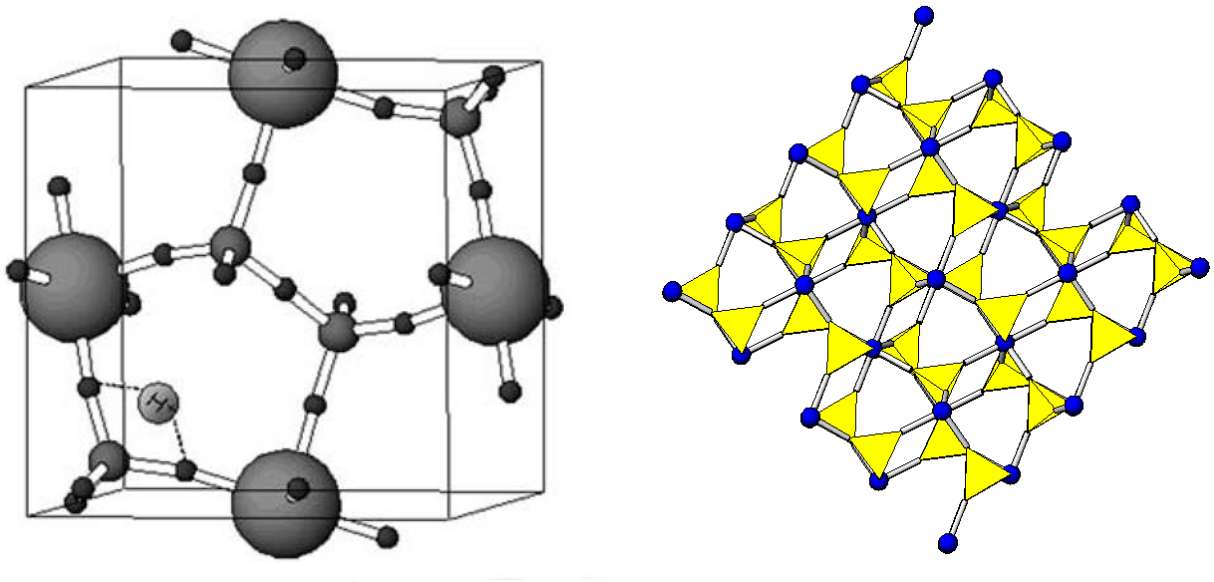

(a) (b)

*Figure 2. 5 a) Location of a proton in $SnP_2O_7$ [75], b) View of $SnP_2O_7$ structure along the c-axis using Atoms63$_{TM}$ software $Sn^{4-}$ ions shown in blue and $PO_4$ tetrahedra shown in yellow.*

The synthesis of undoped and doped pyrophosphates has been reported to be particularly critical for the definition of the transport properties [27]. A typical procedure of preparing pyrophosphates consists of mixing the oxide of the tetravalent atom as well as that of the dopant ion with an excess $H_3PO_4$ solution followed by heat treatment at 300 °C until a viscous paste is formed. Thus the paste formed is then calcined at higher temperature (normally ~ 650 °C), air quenched at room temperature and finally ground [69,70,72,73].

Doping with various cations such as $In^{3+}$, $Sc^{3+}$, $Al^{3+}$ (see Figure 2. 6b) has been reported as a promising way of enhancing the conductivity of the pyrophosphates[70,76] and 10 mol. % of $In^{3+}$ doped is found to be an optimum for enhancing conductivity of $SnP_2O_7$, which among all reported pyrophosphates exhibits the highest value of conductivity, above $10^{-2}$ $Scm^{-1}$.

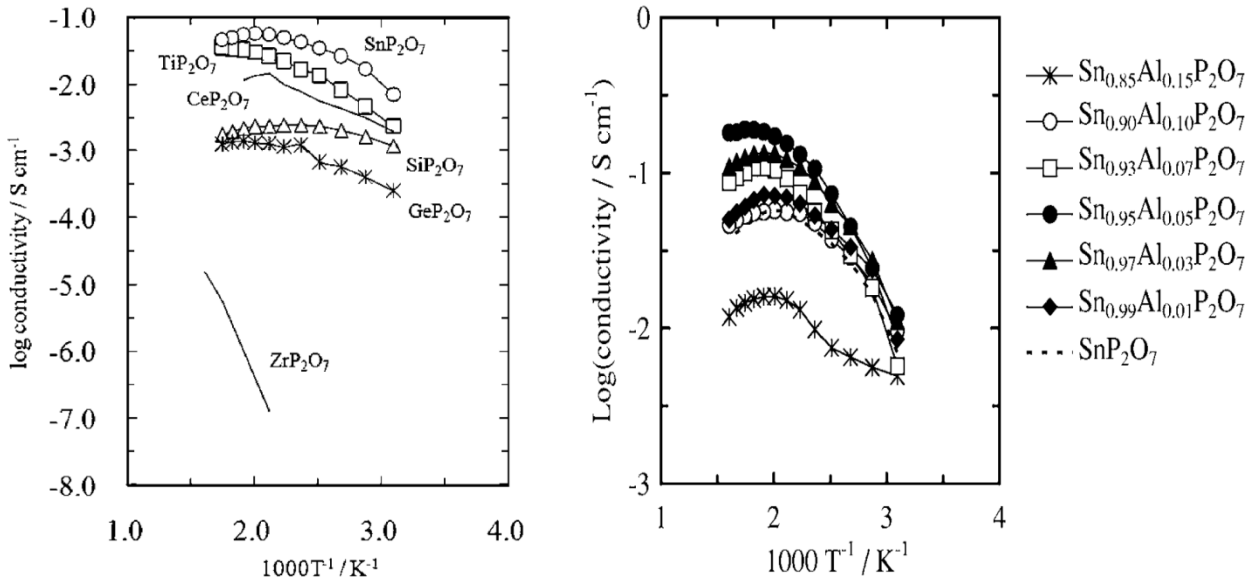


*(a)* *(b)*

*Figure 2. 6 (a) Temperature dependence of conductivity for $MP_2O_7$ (M= Sn, Ti, Si, Ge, Ce and Zr) in non-humidified air [69];(b) Temperature dependence of conductivity for $Sn_{1-x}Al_xP_2O_7$ in non-humidified air [70].*

One of suggested mechanisms responsible for high values of conductivity was described by Jin et al.[72]. The $MP_2O_7$ family does not contain protons in the bulk. In dry conditions ($P_{H2O}$=0.0008 atm) $SnP_2O_7$ exhibits the p-type semiconduction, however, such a tendency decreases with increasing $P_{H2O}$. At above $pH_2O$= 012 atm the conductivity is almost independent of $P_{O2}$ which was assumed to be an indication of an interaction between the water vapor and electron holes. The proposed equilibrium can be expressed by equation (*2.5*):

$$H_2O + 2h\cdot \rightarrow 2H_i\cdot + \tfrac{1}{2}\, O_2 \qquad 2.5$$

where $h\cdot$ and $H_i\cdot$ denote an electron hole and a proton, respectively.

Other authors such as Tao [77] suggested that the conductivity in this materials happened due to the presence of an amorphous phase, a possible, hygroscopic secondary phase for $SnP_2O_7$ materials prepared by aqueous solution methods have been reported to have conductivity at least three orders of magnitude less around $10^{-5}$ $Scm^{-1}$ that of material prepared from method reported by japanese authors.

The $P_2O_7^{4-}$ deficiency decreases the proton conductivity and changes the slope of the temperature dependence of conductivity, which has a flat line instead of characteristic maximum at temperatures 140-240 $^oC$. However the addition of excess of phosphoric acid at the same time lead to formation of unidentified highly hygroscopic impurities (assumed to be polyphosphorous oxides $P_mO_n$ [78]) with absorbed water from ambient atmosphere. These finding coming from the preparation technique opened several questions about the nature of proton conductivity of pure and doped pyrophosphates and the role of dopants in the mechanism of conduction. This phosphate

deficiency in $Al^{3+}$ doped $SnP_2O_7$ has been studied and reported as cause of the extremely low conductivity which can be explained by the disconnection of proton pathways. Depending on the amount of the deficiency, $Al^{3+}$ doped $SnP_2O_7$ conductivity can vary in two orders of magnitude [70,76].

The high values of conductivity was reported for $TiP_2O_7$ by Nagao et al. [69]. Nalini et al. [79] reported decrease of conductivity with increasing sintering temperature. The similar study has been done for undoped or La, Sc, Y doped $ZrP_2O_7$ [80]. The values of conductivity for $TiP_2O_7$ were $1.5\times10^{-5}$ $Scm^{-1}$ and $2.5\times10^{-6}$ $Scm^{-1}$ at 500 °C in dry and wet oxygen, respectively, protonic nature of which were confirmed by hydrogen/deuterium isotope effect. Influence of sintering temperature for $TiP_2O_7$ was as well confirmed by Lapina et al. [81], using TG and EDX methods together with conductivity measurement and systematic studies of synthesis.

As an approach for obtaining a dense membrane with good mechanical properties, it was recently proposed [74] to prepare $MP_2O_7$-$MO_2$ (M=Sn, Si, Ti, and Zr) composites from porous $MO_2$ substrates by treatment with $H_3PO_4$. The morphology of the prepared samples was studied by SEM/EDX (see Figure 2. 7) revealing large differences between prepared composites. While $SnP_2O_7$ filled up 90 % of the pores in the $SnO_2$ substrate during preparation, composite ceramics based on $ZrP_2O_7$ did not fully grow in the pores of the $ZrO_2$ substrate. The $TiP_2O_7$ -$TiO_2$ had a better dispersion because of the small pore size of the $TiO_2$ substrate and gave the densest composite ceramics whereas needle shaped $SiP_2O_7$ -$SiO_2$ ceramics had relatively low dense samples.

The dense properties of prepared composites had a significant influence on the proton conductivity and temperature dependence of the conductivity for the composite materials in comparison with their substrates, as shown in Figure 2. 8. The conductivity measurement was performed in a temperature range between 50-700 $^oC$ on the polished disk samples with a gold slurry deposited on both sides of the polished surface of disks. All composite ceramic samples (except $SiP_2O_7$-$SiO_2$) had shown increase in conductivity at temperatures above 200 $^oC$ but values of the observed increase were found to be dependent on the used M species. The sample with lowest dense properties (see Figure 2. 7) such as $ZrP_2O_7$-$ZrO_2$ and $SiP_2O_7$-$SiO_2$ composites showed conductivity below $10^{-4}$ $Scm^{-1}$in the entire temperate range while the $SnP_2O_7$-$SnO_2$ reached conductivity value of $10^{-2}$ $Scm^{-1}$above 250 $^oC$ and remained stable until the maximum measured temperature.

The Sn based composite was found to be as the most promising among the tested ceramics because of the dense membrane with a good stability of composite and high values of conductivity in the investigated temperature range.

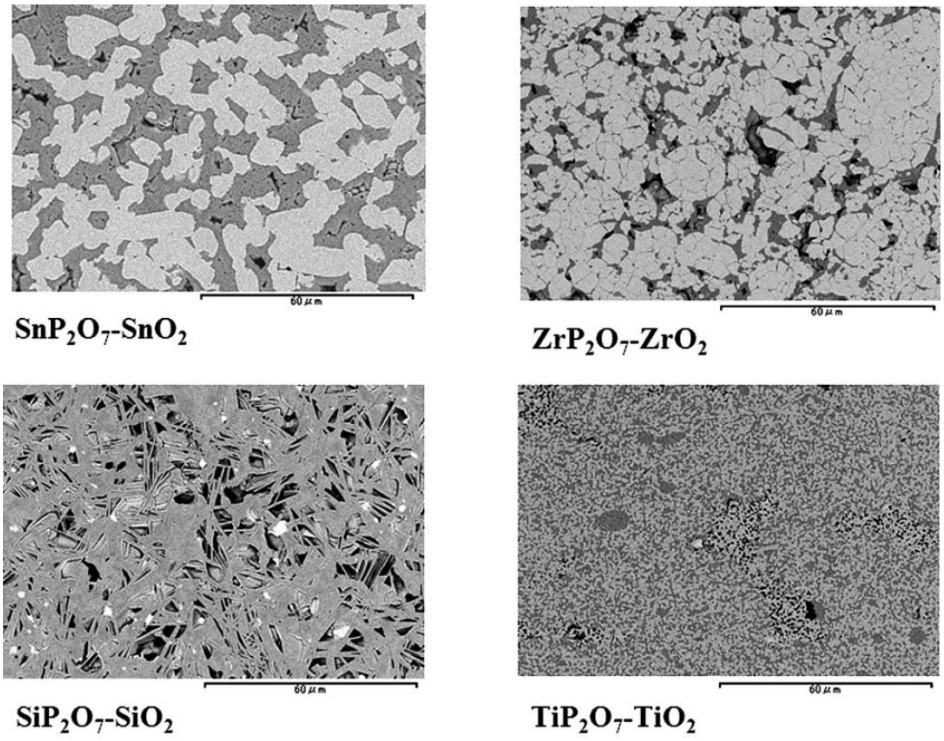


*Figure 2. 7. Cross-sectional SEM images of the $MP_2O_7$-$MO_2$ composite ceramics (M=Sn, Si, Ti and Zr) [74].*

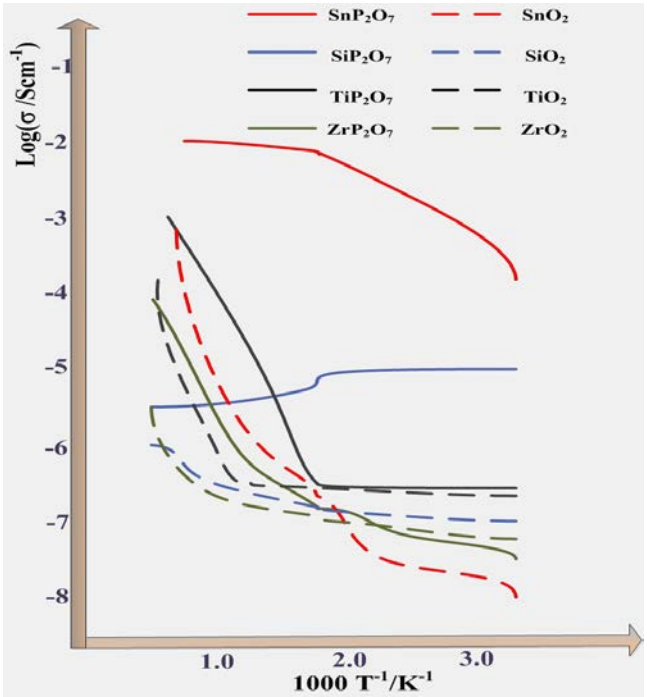


*Figure 2. 8 Temperature dependence of the electrical conductivity of the $MP_2O_7$-$MO_2$ composite ceramics (M=Sn, Si, Ti and Zr). For comparison, data for the $MO_2$ substrates are also included (Built based on data from[74]).*

## 2.4 $LaPO_4$ and rare earth metal phosphates

Proton conduction at high temperatures has been reported for different families of rare earth phosphates. Research efforts are mainly focused on orthophosphates such as Sr-doped $LaPO_4$ [82, 83, 84, 85, 86], $Ba_3Ce(PO_4)_3$ and $CePO_4$ [87]. The defect chemistry of phosphates is still a question of investigations [88, 89, 84] and usually meet certain challenges as described in Chapter 1. In these materials, protons are introduced from hydrogen containing gases in ambient atmosphere and the structure plays an important role in proton transfer.

Lanthanum phosphate $LaPO_4$ has been considered as a solid electrolyte by Norby [82] with potential applications to hydrogen fuel cells. Such interest in rare earth phosphates and doped rare earth phosphates was probably inspired by the previous research of rare earth oxides [90] with the fluorite-type structure. The $LaPO_4$ was known as a very stable material and the large $La^{3+}$ ions seemed to be beneficial for the proton mobility in oxides. Norby et al. [82], using a co-precipitation method, obtained 5 atom% Ca and Sr-doped $LaPO_4$. Figure 2. *9* represents the conductivity curves as a function of temperature under dry air, which was linear in the high temperature range with activation energies of around 1.3 eV. Higher conductivities were observed for the Sr-substituted than in the Ca-substituted sample. With an atmosphere containing $D_2O$ or $H_2O$, at higher temperatures, the conductivity approached the native conductivity curve where the isotope effect diminished, suggesting that the conductivity became non-protonic. This conductivity was believed to reflect the p-type electronic conductivity. Based on the proposed model, the activation energy for the proton mobility was estimated to be approximately 0.8 eV. The finding of the proton conductivity in this material encouraged further studies of proton conductivity in rare earth orthophosphates [15, 87, 91-97].

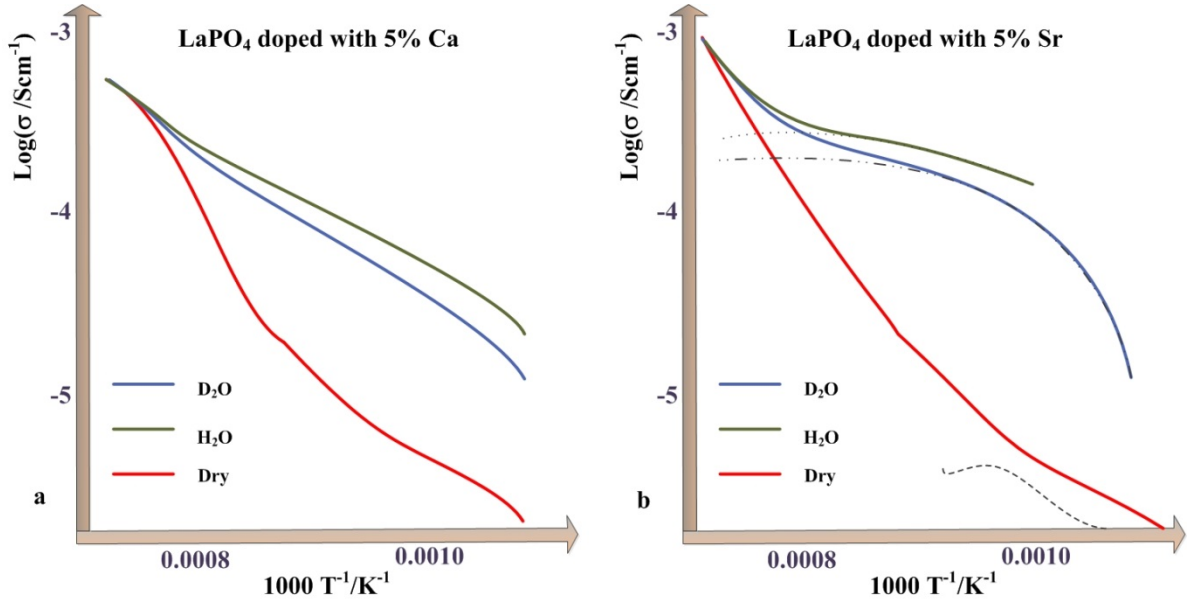


*Figure 2. 9 a) Log conductivity versus 1/T for Ca-substituted $LaPO_4$ in dry air and air with 2% $H_2O$ or $D_2O$ in the temperature range of 600-1100 °C b) Log conductivity versus 1/T for Sr-substituted $LaPO_4$ in dry air and air with 2% $H_2O$ or $D_2O$ in the temperature range of 600-1100 °C (Built based on data from [82]).*

This material indeed has a great advantage in term of thermodynamical stability over other proton conducting lanthanum phosphates, such as polyphosphate and ultraphosphate ($LaP_3O_9$ and $LaP_5O_{14}$) which undergo gradual hydrolysis at elevated temperatures. The mechanism of protons dissolution into Sr-doped $LaPO_4$ was proposed to be through the equilibria described by Amezawa [83] (*2.6-2.8*):

$$\frac{1}{2}Sr_2P_2O_7 \rightarrow Sr_{La'} + \frac{1}{2}(P_2O_7)^{\cdot\cdot}_{2PO4} \qquad 2.6$$

$$\frac{1}{2}(P_2O_7)^{\cdot\cdot}_{2PO4} + \frac{1}{2}H_2O \leftrightarrow (HPO_4)^{\cdot}_{PO4} \qquad 2.7$$

$$\frac{1}{2}(P_2O_7)^{\cdot\cdot}_{2PO4} + \frac{1}{4}O_2 \leftrightarrow (PO_4)^{x}_{PO4} + p \qquad 2.8$$

where $(P_2O_7)^{\cdot\cdot}_{2PO4}$ and $(HPO_4)^{\cdot}_{PO4}$ represent a pyrophosphate ion at adjacent two orthophosphate ion sites and a hydrogen phosphate group, possibly a diphosphate ion, at an orthophosphate ion site, respectively. On the first stage the oxygen deficits are introduced as pyrophosphate ions (*2.6*) by substituting Sr with La ions in the cation sub lattice and on the second stage (*2.7*) protons dissolve in phosphates through the equilibrium between pyrophosphate ions and water vapor. The electron holes *p* (*2.8*) contribute to the process of conductivity with increasing temperature via the equilibrium between pyrophosphate ions and oxygen gas.

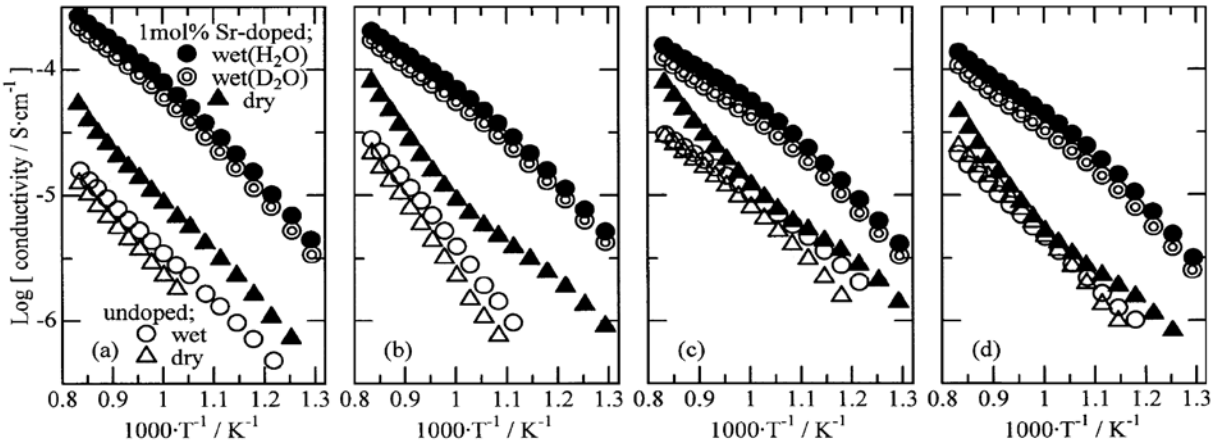


*Figure 2. 10 Conductivities of undoped and 1mol% Sr-doped (a) $LaPO_4$, (b) $PrPO_4$, (c) $NdPO_4$, (d) $SmPO_4$ under wet ($H_2O$ or $D_2O$) and dry atmospheres at $p(O_2)$=1 kPa [85].*

Electrical conduction in rare earth orthophosphates of formula Ln = La, Pr, Nd and Sm with the monazite structure was investigated at 500-925 °C (see Figure 2. 10).

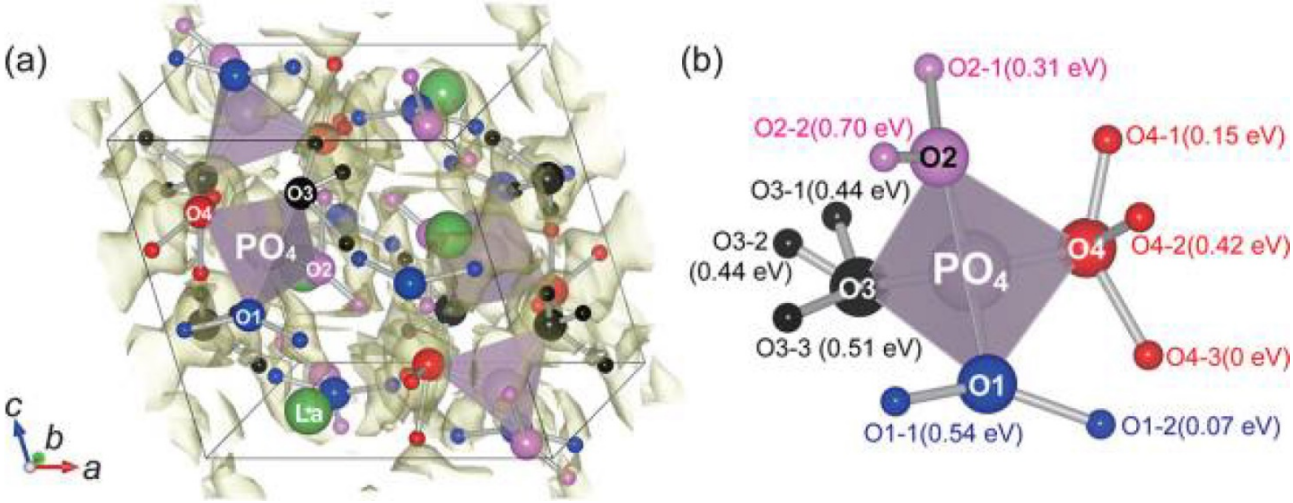


*Figure 2. 11 Crystal structure of $LaPO_4$ with the isosurface (points of a constant value) in the calculated potential energy surface (PES) of protons and the energy local minima, i.e., proton sites. The green balls and the purple tetrahedra denote La ions and $PO_4$ units, respectively. The oxygen sites at the corners of $PO_4$ are classified into four, O1, O2, O3, and O4, shown by blue, pink, black, and red balls, respectively. The isosurface level of the yellow surface is 1,3 eV with reference to the most stable. The small balls bonding to oxide ions are the proton sites. (b) The proton sites around each oxide ion. The energies in the parentheses are the potential energies with reference to the most stable [88]*

The proton transfer mechanism of lanthanum orthophosphate was first described by Yu and De Jonghe [15] at the atomic scale in the transition state theory on the basis of the density functional calculations. Recently the proton conduction mechanism in $LaPO_4$ was theoretically clarified using the kinetic Monte Carlo simulations by Toyoura [88]. It was found that the proton conducting network consists of as many as 20 kinds of migration paths with potential barriers below 1 eV. The migration paths can be classified into three groups: rotations, intra and intertetrahedral hoppings (Figure 2. 11). All the $PO_4$ tetrahedral units in crystals are crystallographically equivalent and four oxygen sites located at the corners of terahedra are not equivalent and distinguished as O1, O2, O3 and O4. There are two or three energy local minima around each oxygen site and all the O-H bond lengths are ~1 Å, which approximately is equal to that in water.

### 2.4.1 Mixed phosphates of rare earth and alkali metals

The study of phases and crystallization in the $Me_2O$-$Nd_2O_3$-$P_2O_5$-$H_2O$ system under hydrothermal conditions [98] shows that four phases can be crystallized in the system which are: $NdPO_4$, $Nd(PO_3)_3$, $NdP_5O_{14}$ and $MeNdP_4O_{12}$. The two known ways to obtain rare earth metal phosphates with alkali metals are synthesis from aqueous solutions (wet precipitation) and from high-temperature aqueous solutions (hydrothermal synthesis). The dependence of the changes in chemical potential and pressure-temperature conditions of the system is shown by the phase transformation diagram (see Figure 2. 12). The increase in temperature is proportional to the

decrease in concentration of alkaline elements and phosphorus in the system. Depending upon the initial conditions of crystallization it is possible to obtain the fields of crystallization of either $Nd(PO_3)_3$ or $NdPO_4$. The rise in temperature and the variation in the concentration of the initial components within the field of crystallization of $MeNdP_4O_{12}$ give different polymorphic modifications. For example, in the system $Cs_2O$-$Nd_2O_3$--$P_2O_5$-$H_2O$ below 500 °C the mixed cyclic phosphate $CsNdP_4O_{12}$ contains four-membered rings of phosphorous-oxygen in its structure are crystallized, but above 500 °C mixed polyphosphates containing infinite chains of phosphorous oxygen anions in the crystallized structures are formed [98].

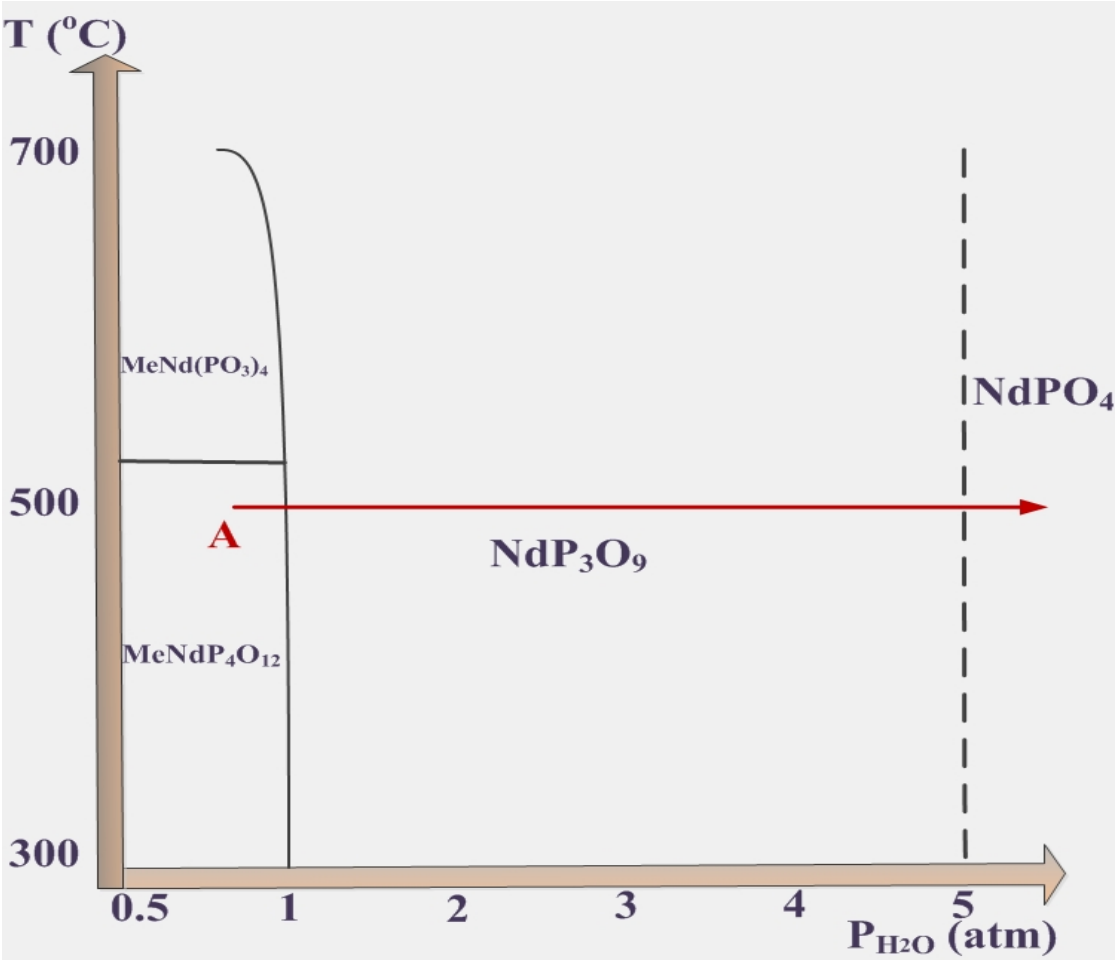


*Figure 2. 12 Phase transformation of rare earth and alkali mixed phosphates with reference to changes in pressure and temperature conditions. The transformation takes place with an increase in the molar fraction of water (point A: $MeNdP_4O_{12} \rightarrow NdP_3O_9 \rightarrow NdPO_4$) (Reproduced from[99]).*

Concerning synthesis of $MeNdP_4O_{12}$, three important conclusions have been reached from the diagram[98]. First of all, the growth from such solutions leads to the existence of a distinct amount of $(OH)^{-1}$ species and a high temperature of crystallization (500 to 600 °C) often reduces the concentration of $(OH)^{-1}$. This is quite interesting for proton conductivity studies because the hydroxyl groups can facilitate the proton conductivity at intermediate temperatures. Secondly the polymerization of the phosphoric acid can be hindered by any increase in the concentration of $H_2O$

and $Me_2O$ in the system. And finally the partial pressure of water beyond 5 atm in the system would lead to the crystallization of pure orthophosphates, as seen from Figure 2. 12.

Single crystals of $KLaP_4O_{12}$ were synthesized by using the flux technique for laser applications by Belam [100]. Several other rare earth phosphates with formula of $A^{I}LnP_4O_{12}$ (where $A^{I}$ = Li, Na, K, Rb, Cs) were obtained by different researchers [101, 102, 103]. Synthesis of $KLaP_4O_{12}$ consists of mixing of initial reactants ($K_2CO_3$, La $(OH)_3$ and $NH_4H_2PO_4$) with a molar ratio of K:La:P = 5:3:58. The mixture is placed in an alumina crucible with the following heating at 350 °C for 2 weeks and then cooled slowly at the rate 5 °C $h^{-1}$ to room temperature. Thus obtained crystals were washed with boiling water several times and the final product was colorless prism crystals of $KLaP_4O_{12}$. The crystal of obtained crystals had no isostructural analogues among the compounds investigated earlier even if taking into account the fact that alkali ions such as $K^+$ and $Cs^+$ had the same coordination. The phosphates are in layer structures with anionic layers formed by $[P_4O_{12}]^{4-}$ groups and cationic layers by $K^+$ and $La^{3+}$. This structure arrangement leads to a three dimensional framework with tunnels in which the $K^+$ cations are located as shown in Figure 2. *13*. [100]. On the other hand, the crystal structure of $CsNdP_4O_{12}$ is found to have no typical layered organization as observed for $KLaP_4O_{12}$. It is built of $NdO_8$ polyhedra and $P_4O_{12}$ groups linked by Nd-O-P mixed bridges to form a three-dimensional framework delimiting tunnels in which the $Cs^+$ cations are inserted.

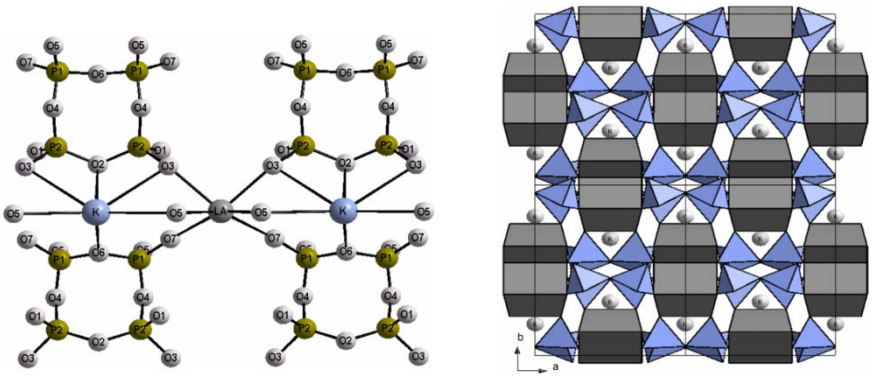

*Figure 2. 13 a) Coordination of potassium and lanthanum cations; b) the atomic arrangement of $KLaP_4O_{12}$ in projection along the c-axis [100].*

The DTA–TGA–DSC thermal analysis was made by Belam et al. [100] to determine the thermal behavior of $KLaP_4O_{12}$ as a function of temperature. In this work, the recorded thermogram indicates that $KLaP_4O_{12}$ undergoes a transformation into $KLa(PO_3)_4$ at 690 °C, whereas its fusion was detected at 875 °C. As a result the temperature range used in the complex impedance spectroscopy is selected to be in the thermal stability range of this compound from 200 to 600 °C. The impedance spectra have shown the presence of only one semicircle, from which the total conductivity, $\sigma_{tot,}$ was calculated from the total resistance value, $R_{tot}$. Furthermore, the activation energy of $E_a$ = 0.31 eV, which is calculated from the slope of the plot, is in agreement with literature data of NASICON, the other type of ionic conductor [104].

## 2.5 Other interesting proton conducting phosphates

Several other phosphate systems can be shortly mentioned as interesting candidate materials for intermediate temperature applications.

As an alternative way of replacement of polyphosphoric acid in fuel cells, ammonium polyphosphate (APP) has been under development for the past twenty years [27]. While pure APP is a rather poor proton conductor with conductivity around $10^{-7}$ S/cm at 250 $^{o}$C the partial decomposition of APP into $HPO_3$ and $NH_3$ is found to promote the conductivity. The practical application of APP based electrolytes has still bounded by several challenges [27]. Among others are its low density of materials, which is partly caused by the low sintering temperature (400 $^{o}$C) and its poor chemical stability due to partial decomposition of ammonium phosphates at elevated temperatures. Significant efforts have been made to develop APP based composites with the aim of improving the thermal and mechanical properties while preserving the high conductivities. Typical APP composites are $(NH_4)_2MP_4O_{13}$ where M = Si, Ti, Sn, Mn etc.

Zirconium phosphates are another important family of hydrate compounds consisting of tetravalent metal acid salts and have the general formula $M^{IV}(HPO_4)_2 \cdot nH_2O$, where $M^{IV}$ = Zr, Ti, Sn, Ce, Th, etc. The number of water molecules depends on the synthesis method and drying conditions. The ion-exchange behavior on these materials is due to structural hydroxyl protons. When these hydroxyl groups are hydrated, protons can move freely on the surface and therefore the conductivity of these materials strongly depends on the relative humidity, surface area and degree of crystallinity [105]. Clearfield and Stynes in 1960s reported the crystalline $\alpha$-$Zr(HPO_4)_2 \cdot H_2O$ and its $\alpha$-type layered structure [106]. Since then, a significant amount of work has been dedicated to this interesting compound. Alberti and his co-workers are among the significant researchers, who synthesized a series of layered and pillared metal (IV) phosphates and phosphonates [107].

## 2.6 Summary

The fuel cell and electrolyser technology operating in the intermediate temperature range has potentials for increasing performance and utilizing non-noble catalysts of low cost. Phosphate systems have been found to be promising candidates as the proton conducting electrolyte including solid acids, pyrophosphates and rare earth metal phosphates.

Phosphate based solid acids have received most of the research attention. On the basis of an evaluation of the literature it is now beyond doubt that $CsH_2PO_4$ undergoes a superprotonic transition at 230 °C and humidity control is essential to the material stability and therefore its applications in electrochemical devices. Fuel cell measurements to date demonstrate that it is possible to support thin-film $CsH_2PO_4$ electrolytes on porous gas diffusion electrodes and obtain peak power densities as high as 415 mW $cm^{-2}$. Efforts are demanded to extend the operating temperature range which is limited by the instable superprotonic phase. Development of composite materials based on $CsH_2PO_4$ has been a focus in the field.

## 2 Phosphates as proton conductors

Doped tin pyrophosphates showed a proton conductivity of above $10^{-2}$ S/cm in the intermediate temperature range under dry or low humidity atmosphere. The pyrophosphates have better chemical stability with no significant decomposition or phase transformation like the solid acids and therefore are less demanding for humidity control. However, understanding of conductivity mechanism and synthetic methods needs to be improved.

Conductive properties and conductivity mechanisms of rare earth metal phosphates are still under active investigation. Combination of proton conductivity, chemical stability and good mechanical properties makes those materials, as well as their composites, potential candidate, for use as electrolyte in water electrolysers and fuel cells.

# 2 Phosphates as proton conductors

# Chapter

# 3 Experimental methods and techniques

## 3.1 Preparation techniques of phosphates

Through this project several types of phosphates were investigated, including rare earth metal phosphates and particularly their hydrates, indium doped tin pyrophosphate, cerium ultraphosphate and cesium dihydrogen phosphate. These phosphates were prepared in the lab. Here below is a brief description of the preparation.

### 3.1.1 Preparation of $MPO_4 \cdot nH_2O$ where M=La, Nd, Gd

Three lanthanide elements were selected in the projects which were lanthanum, neodymium and gadolinium. The phosphate hydrates were prepared using $La_2O_3$ (Sigma-Aldrich 99.99 %), $Nd_2O_3$ (Sigma-Aldrich 99.9 %) and $Gd_2O_3$ (Megon 99.99 %) as precursors by a method that can be referred as wet precipitation synthesis. The individual oxide was added into a 0.6 M aqueous $H_3PO_4$ solution and the mixture was heated to 150 °C and kept for 3 hours under constant stirring. The resulting precipitates were slowly cooled down to room temperature and then filtered from the solution with following washing of the precipitate.

### 3.1.2 Preparation of $CsH_2PO_4$

The $CsH_2PO_4$ powder have been prepared by neutralizing solutions of $Cs_2CO_3$ (Sigma-Aldrich purity 99%) with $H_3PO_4$ (Sigma-Aldrich purity 85%) until pH of solution to about 4.6. All prepared powders have been kept in furnace constantly at temperature $80^o$ C in order to remove residual water.

### 3.1.3 Preparation of $Sn_{0.9}In_{0.1}P_2O_7$

**Preparation of $Sn_{0,9}In_{0,1}P_2O_7$ using oxides precursors**

The metal precursors $SnO_2$ (size 80 nm) and $In_2O_3$ are first mixed with water is then added in according to desired molar ratios (typically P/M=2.8) with $H_3PO_4$ wt. 85%. The mixture was contained in a Pyrex round-bottom flask and heated in an aluminum DrySyn® heating block with magnetic stirring. A thermocouple was placed in a wall of the aluminum block for temperature control. The temperature was first increased from room temperature to $90^oC$ within an hour, by which most of the water was evaporated. The temperature was then increased to $280^oC$ under

constant stirring until a viscous paste was obtained after about 2 hours. The resulting paste was transferred to an alumina crucible and further heated with a lid to 650$^{o}$C with a temperature ramp of 180$^{o}$C h$^{-1}$ and kept at this temperature for 3 hours. The material obtained by the above procedure was ground and kept in a desiccator. Later in text the samples prepared by this method are referred to as CA samples (Chapter 7). A part of the sample (CA2) was further boiled in demineralized water for an hour and then filtered. The water washed sample was referred to as CA2V.

**Preparation of $Sn_{0,9}In_{0,1}P_2O_7$ using acetate precursors.**

According to Park et al. [108] the acetate aqueous method allows to produce pure crystalline and highly uniform powders of $Sn_{0,9}In_{0,1}P_2O_7$ with thin amorphous layers depending on the phosphorus to metal ratio. The detailed procedure have been taken from [108] and can be described by a flow chart as in Figure 3. 1.

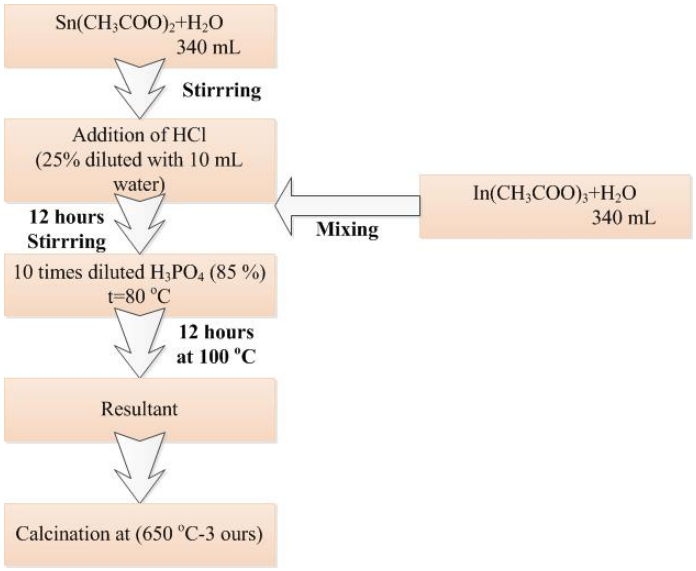


*Figure 3. 1 Steps of preparation method of $Sn_{0,9}In_{0,1}P_2O_7$ from acetate precursor [108].*

Acetate precursors of tin and indium in desired stoichiometric amounts were first dissolved in water. The aqueous solution of HCl was added and the mixture was stirred during for 12 hours. A dilute solution of 8.5% $H_3PO_4$ was added dropwise at a temperature of 80 $^{o}$C with constant stirring. The beaker was then placed in oven at 100 $^{o}$C for 12 hours. The resultant viscous paste was then heat treated at 650 $^{o}$C. Later in text the samples prepared by this method are referred to as MA samples (Chapter 7). Additionally part of the MA sample was further treated with additional amount of $H_3PO_4$ wt. 85%. The specified amount of phosphoric acid (P/M ratio 1:1) was diluted to ensure the full wetting of the powder when the MA powder was added in an alumina crucible. The crucible was then placed in furnace at 100 $^{o}$C to evaporate water, and then powder was finally heated with a lid on at 650 $^{o}$C for 2 hours with a ramp of 180 $^{o}$C/h.

**Preparation of $Sn_{0,9}In_{0,1}P_2O_7$ using chloride precursors.**

The detailed procedure was taken from [109] for preparation of pure crystalline phosphates. The precursors $SnCl_4 \cdot 5H_2O$ and $InCl_3$ were first dissolved in an aqueous solution of HCl in desired stoichiometric amounts (pH = 0.5 otherwise tin chloride can hydrolyze). Another solution of $(NH_4)_2HPO_4$ (Sigma-Aldrich purity 99%) was separately prepared by dissolving the chemical in water. The two solutions were mixed dropwise to reach a final phosphorus to metal ratio of 2. To evaporate the water the mixture solution was slowly heated to 120 $^oC$ within 3 hours. It was further heated to 200 $^oC$ until it got almost dry. The solid mixture was then placed in a crucible and heat treated without lid on at 650 $^oC$ for 3 hours with a ramp of 180 $^oC$/h. Later in text the samples prepared by this method is referred to as MC (Chapter 7). Additionally part of the MC sample was further treated with an additional amount of $H_3PO_4$ with a P/M ratio of 1:1 and for the second time heated with a lid on at 650 $^oC$ for 2 hours with a ramp of 180 $^oC$/h.

### 3.1.4 Preparation of $CeP_5O_{14}$

Crystals of $CeP_5O_{14}$ were synthesis by a high temperature solution reaction, between $CeO_2$ $CeO_2$ (IV) (Johnson Mattey Alfa Products 99,9%) and $NH_4H_2PO_4$ (BDH Laboratory reagent 99%) in molar ratio Ce/P =1:12, as described by Zhu, Cheng and Zhang [110]. The mixture was mixed for 1 hour in vitreous carbon crucible with magnetic stirrer. The crucible was transferred to furnace, where the temperature and atmosphere can be precisely control. The heating process was done under an argon atmosphere. The crucible was heated at 100 $^oC$ for 4 hours, and then the heating was increased to 800 $^oC$ for 24 hours. Finally, the crucible was cooled to 500 $^oC$ at rate 2 $^oC$ and then air quenched. A large number of white blocked crystal were obtained.

## 3.2 Electron microscopy

### 3.2.1 Scanning electron microscopy

In the early 1950s, the scanning electron microscopy (SEM) has been developed and this invention opened new areas of research in science communities earlier impossible because of use traditional optical microscopes. Nowadays SEM has become a common practical technique. A schematic overview of the SEM is presented in Figure 3. 2. Electrons are emitted from a filament (electron gun) in vacuum conditions and accelerated by a positively biased anode. After acceleration focused by magnetic lenses they hit the sample and it yields secondary, backscattered, Auger electrons and X-rays. The final image depends from detector type used to collect these X-rays or electrons and convert them into a signal. When morphology or topography (surface parametrs) of samples is main purpose of research secondary electron detector is most useful. Multiphase samples and differences in compositions can be well studied with the backscattering detector. The general rule is that elements with high atomic numbers (for example rare earth elements La, Nd, Gd) are more efficient scatters in such studies. Their images appear brighter. The bias determines the resolution of the image and depending from type of SEM it is possible to achieve resolution better than 1 nanometer. The Carl Zeiss EVO MA10 microscope was used for acquiring the SEM images.

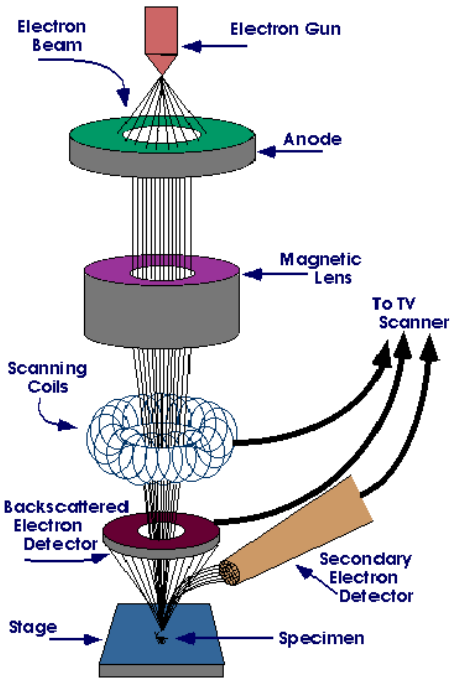


*Figure 3. 2 Scanning electron microscope. Reproduced from [111]*

The sample preparation had been usually more complicated than the general procedure as phosphate powders commonly are not good electronically conducting materials additional coating procedures often have been required and parameters of this coating had been developed for each powder separately.

### 3.2.2 Energy dispersive X-ray Spectroscopy

The chemical analyses of specimen can be performed qualitatively and quantitatively by collecting characteristic X-rays after bombarding sample with electrons from the electron gun. Such technique received name X-ray energy dispersive spectroscopy (EDX or EDS). Oxford EDX X-max 80 $mm^2$ detector had been used for performing element analyses and mapping (elemental spatial distribution) and data was analyzed with INCA Energy Software. The elements with atomic number less than 5 (H, He, Li or Be) cannot be studied by this technique. The EDX usually gives a general overview of chemical element content of the sample but a precision of quantitative numbers is limited by different artifacts such as high energy of the incident beam or distance of sample from EDX detector and depend on atomic number of studied element.

## 3.3 X-ray diffraction and structure determination

In order to solve a crystal structure it is required to determine the precise arrangements of all of the atoms in a chemical compound in the crystalline state. Obtaining such knowledge gives a wide range of information such as accurate bond lengths and angles, stoichiometry, density, phase transitions and a picture of three dimensional packing of the atoms in solids. The process by which the radiation (λ=50-300 pm) without changing its wavelength, is converted through interference by the lattice to a vast number of observed "reflections with characteristic directions in space is called X-ray diffraction (XRD) [[112]]. Since all diffraction experiments employed monochromatic radiation, it is became a practical to use a very strong $K_\alpha$ lines as listed in Table 3. 1 which are derived from the mean of the $K_{\alpha1}$ and $K_{\alpha2}$ – wavelengths weighed by their 2:1 intensity ratio.

*Table 3. 1. $K_\alpha$ – wavelength of the most important types of X-ray tubes.*

| | Mo | Cu | Fe |
|---|---|---|---|
| $K_{\alpha1}$ | 0.70926 | 1.54056 | 1.93597 |
| $K_{\alpha2}$ | 0.713543 | 1.54433 | 1.93991 |
| $K_\alpha$ | 0.71069 | 1.54178 | 1.93728 |

Several techniques can be used to obtain X-ray diffraction pattern of a studied material. The choice of techniques depends on requirements to obtain information, conditions and type of samples.

Under this project mostly powdered samples were obtained and X-ray powder diffraction has been used. For this purpose Huber D670 applying Guinier method with the Cu $K\alpha_1$ i.e. 1.54056 radiation source from a focusing quartz monochromator was chosen.

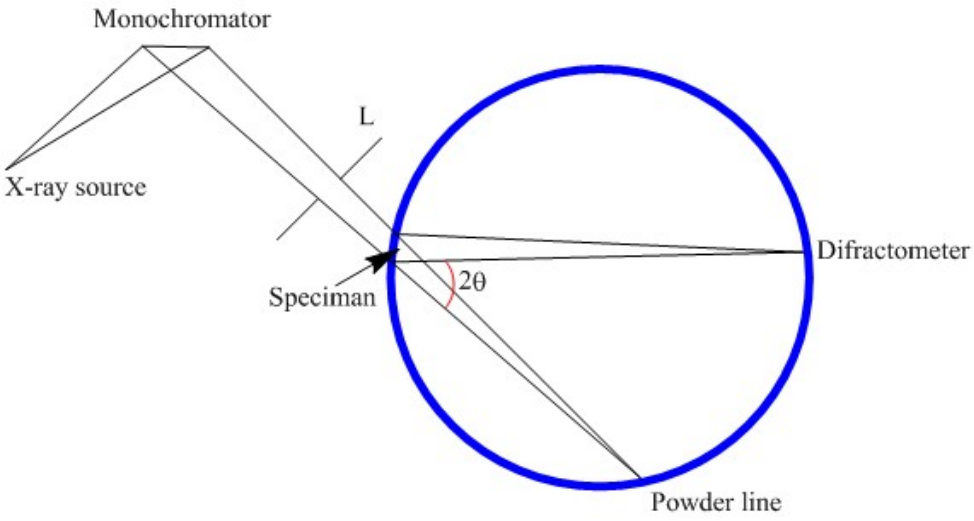


*Figure 3. 3 The scheme of camera with Guinier geometry.*

The geometry of the Guinier camera is based on transmission mode. It is possible to remove $K\alpha_2$ line by focusing monochromator and only strong $K\alpha_1$ is used. The powdered sample (only a few hundred μg as grounded in an agate mortar) is mounted on a tape and attached to a sample holder. The sample is kept spinning during data collection.

It is important to record diffraction pattern of the tape as well. Influence of background is relatively high because of air and tape scattering thus sample adsorption will affect a powder diffraction pattern and intensities of recorded peaks. The measured diffraction pattern will be different from an ideal powder pattern and a position of peaks can be shifted with respect to reference.

An unidentified powder diffraction pattern is used to compare with known powder diffraction files (PDF). The International Centre for Difraction Data database [113] with extensive collection of known patterns is available as software.

### 3.3.1 Structural refinement and other analyzing techniques

The diffraction data usually contains a lot of information which can be used for better understanding of a studied material. For the calculation of the *crystal size* which gives a good overview in differences between synthesis methods of phosphates and materials in general the Scherer equation can be used, see equation *3.1* where K=0.9 is a shape factor, λ is the X-ray wavelength, see Table 3. 1, β is the peak width in radian and θ is the Brag angle of the peak.

$$\tau = \frac{K\lambda}{\beta cos\theta} \qquad 3.1$$

Modern software such as Winprep can calculate the crystal size automatically when a peak from diffraction data is chosen. In theory any peak can suit for this calculation but in practice it is better to use peaks with high intensities. The calculation with equation *3.1* usually gives some deviation from the measured value and uncertainty will be larger if peaks with low signal-to-noises ratios are used.

The *asymmetric unit* is the minimum group of atoms whose positions, together with those from the symmetry operations of the space group generate the complete contents of unit cells [112]. When a molecule symmetry conformed to the crystallographic symmetry, it can occupy a special position, and the asymmetric unit can then be a half molecule or even a smaller fraction. In this case it is necessary in structural determinations, to know Z, number of formula units per unit cell (if one considers an approximate volume of 17 $Å^3$ to each of the non-hydrogen atoms in the formula), since it is possible to calculate the density of the substance using equations *3.2* and *3.3* where $M_r$ is the molar mass, $N_A$ is the Avogadro number, V is volume of the unit cell calculated from the lattice constants.

$$Z = \frac{V}{17 \cdot M} \qquad 3.2$$

$$d_c = \frac{M_r Z}{V N_A} \qquad 3.3$$

The measured density is usually slightly lower than the ideal value $d_c$ but can be used to calculate the unknown Z. In international tables of PDF files an asymmetric unit Z is given for each space group.

For many compounds it is almost impossible to obtain single crystals but relatively easy to get a very good powder diffraction patterns. By refining diffraction data it is possible to derive a starting structural model using such software as Winpow and Atoms63. These software programs are complementary but are far from the only available software for the structural refinement. The Winpow software is based on conceptions of the Rietveld refinement. In order to use Atoms 63 knowledge of crystallography is required. By importing previously refined diffraction data from Winpow to Atoms63 it is possible to obtain 3D representation of structure for different materials. Since diffraction refinement methods are not within the scope of this study, further details can be found in relevant literature [[112], [114]].

## 3.4 Thermogravimetric and differential thermal analyses

The way to study the thermal stability of powders can be performed by combination of thermogravimetric analysis (TGA) together with the differential thermal analysis (DTA). Some of phase transitions, adsorption/desorption of water on the surface or in the crystal structure and oxidation, reduction or evaporation of the sample in different atmospheres can result in mass change (mass loss). By the TGA method the weight change of the sample is measured against time and plotted as a function of the mass loss versus temperature (or time at a fixed heating ramp). By the DTA method the temperature difference of the heating sample with respect to that of the reference (usually the empty $Al_2O_3$ crucible) is recorded. In this way it is possible to study the thermochemical nature of the sample changes, for example positive difference indicates an exothermic reaction whereas negative difference shows an endothermic reaction. In this study the TGA and DTA measurements were performed using a Netzsch STA 409 PC equipment. Air, argon and 5 vol. % of hydrogen in nitrogen as a reducing atmosphere were used as purge gasses and the powder samples were heated with a typical heating rate of 10 K/min if not specified.

## 3.5 Vibrational spectroscopy of proton conductors

It was discussed in Chapter 1 that the structure plays an important role in mechanisms of proton conduction. Vibrational spectroscopy such as (infrared, Raman and neutron) is well suited for studies of various protonic species (even at their low concentration) since the AH stretching modes (A= O, N or halogen) give strong absorption bands in the region of (4000-1700 $cm^{-1}$) where an influence of other groups is not strong. X-ray diffraction methods and vibrational spectroscopy are complementary. Both methods can be used to determine with good accuracy the structure of rigid frameworks, to identify protonic entities and their type of association, to investigate different crystallographic or protonation sites and degree of the structural disorder (statically or dynamically). Spectroscopic studies of such dynamical aspects as phase transitions can also shed

some light on the conductivity mechanisms since proton transfer can change significantly from one phase to the other.

The frequency, intensity and width of infrared bands measured as a function of temperature have been used to obtain information about phase transitions. The low frequency bands are generally more associated with lattice aspects than the high frequency intramolecular bands.

The hydrogen bonds in the OH…O system (the frequent case for proton conductors) can be divided into weak, medium-strong and strong with O…O distances > 0.27, 0.27-0.26 and 0.26-0.24 nm, respectively [18]. The weak bonds usually present in hydrates, medium-strong bonds in self associated carboxylic acids and strong bonds in acid salts of many inorganic and organic acids.

For the Fourier transform infrared spectroscopy (FT-IR), spectra of the powder sample were recorded using a Perkin-Elmer VATR TWO spectrometer in the range 450 - 4000 $cm^{-1}$ with a resolution of 4 $cm^{-1}$ under ambient atmosphere and at room temperature. The spectra were integrated using the Spectrum software.

# Chapter

# 4 Experimental aspects of conductivity measurements

## 4.1 Conductivity measurement in solid state

The efficiency and electrochemical performance of fuel cells and other devices depend on the transport and kinetic properties of electrodes, electrolyte and the electrode/ electrolyte interface. Ionic conductivity in the electrolyte is the concern of the present project. There are two general groups of techniques that can be used for characterization of ionic conductivity, the steady state and transient techniques including impedance spectroscopy (IS), galvanostatic current interruption, direct current (DC) conductivity measurements, transport number determination using ion or electron blocking electrodes and electromotive force (EMF) methods for studying thermodynamics using galvanic cells. In case of solid state ionic conductors the IS and galvanostatic current interruption are the most often used techniques. Both methods are complementary but the IS spectroscopy generally brings wider understanding than the galvanostatic current interruption. Solid state ionic conductors can be distinguished from liquid or molten electrolytes in that there is usually only one mobile ionic species and point defects, whose concentrations are determined by the material composition and responsible for the high ionic conduction [115].

### 4.1.1 Definition of conductivity

Proton conductivity is the key characteristics of electrolyte materials developed within this project. Conductivity is the ability of a material to pass an electric current. The opposition of the material to the passage of an electric current is called resistance. The resistance of the material (R) can be calculated using Ohm's law:

$$R = \frac{V}{I} \qquad 4.1$$

where V is voltage (volts), I is current (amperes) and R the resistance (ohms).

For an object of uniform cross section, for example, in form of a pellet, its resistance is proportional to its resistivity (ρ) and length or thickness (L) and inversely proportional to its cross-sectional area (A) by Pouillet's law:

$$R = \rho \frac{L}{A} \qquad 4.2$$

In fuel cells and other electrochemical devises, the area specific resistance (ASR in Ohm•cm$^2$) is of engineering importance and can be expressed as the product of the thickness and the resistivity (ρL).

The conductance (G) is defined as the reciprocal of the electrical resistance (R) of a substance:

$$G = \frac{1}{R} = \frac{I}{V} \qquad 4.3$$

The reciprocal of the resistivity is called conductivity, which has a unit of Ohm$^{-1}$•cm$^{-1}$ or more commonly used S/cm. In electrochemical devises, the area specific resistance (ASR in Ohm cm$^2$) of a pellet electrolyte can therefore be expressed as the ratio of the thickness and the conductivity (L/σ). The physical meaning of the ASR can be understood as the voltage loss (V) of the electrolyte at the unit current density (A/cm$^2$). The expression of the thickness to conductivity ratio indicates that the higher the conductivity (σ) and the smaller the electrolyte thickness (L) give the lower cell ohmic loss.

### 4.1.2 Parameters influencing conductivity measurement

In general the accuracy of conductivity measurements can be influenced by many factors such as:

- Polarization
- Sample dimensions
- Contact point resistance
- Cable/wire resistance or capacitance
- Conditions of experiment such as temperature and humidity (in case of proton conductivity)

***Polarization***

Applying an electrical current through electrodes to the conducting sample may cause a polarization at the electrode surfaces due to electrochemical reaction and concentration changes of active species. In this case a polarization resistance arises on the electrode surface, which may lead to erroneous results as it is a parasitic component to the resistance.

One way to eliminate the polarization effect is to introduce two reference electrodes through which the voltage signals were measured. As there is no current flowing through these reference electrodes, no polarization is developed or included in the measuremnt. This is a popular method for conductivity measurements in liquid electrolyte or polymer membranes, however in our research handling thin pellet of solid conductor, it is difficult to introduce extra two electrodes. This will be discussed in the next section.

Alternatively the polarization effects can be reduced or prevented by using an alternating current, i.e. the measuring current will flow through the double layer capacitance ($C_{dl}$) of the electrodes instead of building up any voltage drop across the electrode surface or the ionic conducting sample. This can be achieved in two ways, the direct current interruption or impedance spectroscopy technique.

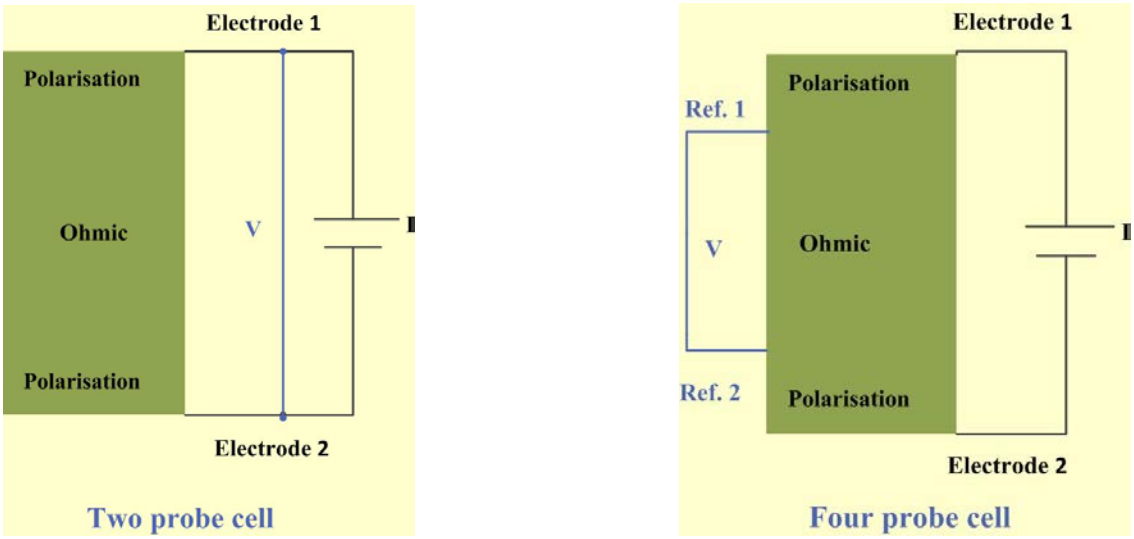


*Figure 4. 1 A schematic representation of two probe and four probe conductivity cells.*

***Contact resistance and current distribution***

Strong pellets should be prepared e.g. by using high press forces, pre-sintering or even hot-pressing. Another issue in this connection is good contact between the sample and leading wires. Compromise should be made by ensuring good contact without breaking the sample. Strong pellets should be prepared e.g. by using high press forces, pre-sintering or even hot-pressing. Another issue in this connection is good contact between the sample and leading wires. Compromise should be made by ensuring good contact without breaking the sample.

***Cable/wire resistance and capacitance***

The leads including cables have a given length and, therefore a given resistance. The cable resistance induces error on the result and must be taken into account. In case of four probe cells, as no current is passing through the voltage measuring reference electrodes, this effect is eliminated. When the cable is shielded, a cable capacity may arise. In two probe cells this has to be considered. In our practice, calibration of the cell assembly without containing the sample is often made.

***Temperature and humidity***

The temperature dependence of conductivity was discussed with relation to activation energy previously (1.4.1). The conductivity mechanisms of the same structure may change as a

function of water partial pressure. In the case of such proton conductors as layered phosphates (see Table 1. 3 and 2.5) the change in water content leads to a change in values of conductivity indicating a variation in the number of charge carriers.

## 4.2 Basics of impedance spectroscopy

Impedance Spectroscopy or IS has come into it is own in the last twelve to fifteen years. IS can be a powerful method to study of a wide range of electrochemical systems and determine the contribution of individual electrode or electrolyte processes especially if it is combined with microstructural and surface characterization techniques such as X-ray diffraction (XRD), electron microscopy and so on. For ionically conducting materials, the technique was first applied by Bauerle [116] in 1969 in order to analyze the response of zirconia based solid electrolyte cells to sinusoidal perturbations. Normally various processes from electrode reactions at the electrode/electrolyte interface (diffusion, adsorption/dissociation, charge transfer) and those associated with mass transport within the solid electrolyte grains and across grain boundaries all have different time constants and can be separated in the frequency domain [115]. Microstructural fluctuations, phase assemblage, compositional variations, segregation of impurities or secondary phases have an influence on the migration mechanism of charge carrying species and thus on the response time.

### 4.2.1 Impedance of an electrochemical cell

Using the conductivity (4.1.1) it is possible to describe an interaction of electromagnetic wave with a condensed matter and thus electrical properties can be determined in a wide frequency range. The relaxations which have a direct correlation with the bulk conductivity and electrode /electrolyte interfacial phenomena are often observed in the a.c. measurement and can be described in terms of complex impedance formalism [18] or the so-called phasor concept of the sinusoidal alternating current, in which voltage and current are presented as rotating vectors in the complex plane (Argand diagram).

Sinusoidal voltage can be expressed as:

$$E = \Delta E \sin \omega t \qquad 4.4$$

$$\omega = 2\pi f \qquad 4.5$$

where ω is the angular frequency, $f$ is in hertz, $E$ is the instantaneous value and $\Delta E$ is the maximum amplitude. In most of cases current will also be sinusoidal and usually of the same frequency ω but different in amplitude and phase φ from the voltage (lagging or leading in amplitude) [117] and can be expressed by *4.6*:

$$i = \Delta i \sin(\omega t + \varphi) \qquad 4.6$$

For a capacitor it is necessary to apply the definition of capacitance, C, which is a relation between potential across the plates, *E*, to the charge *q* of these plates:

$$q = CE \qquad 4.7$$

Differentiating *4.8* to get the current *i* from *4.4* and receive:

$$i = \frac{dq}{dt} = C\frac{dE}{dt} \qquad 4.8$$

$$i = \omega C \Delta E \cos \omega t \qquad 4.9$$

By replacing 1/ωC called the capacitive reactance $X_c$ the current can be expressed:

$$i = \frac{\Delta E}{X_c}\sin(\omega t + \frac{\pi}{2}) \qquad 4.10$$

which is similar to the Ohm's law *4.1* but with *R* replaced by $X_c$ and a phase angle equal to π/2. This phase angle is positive so the current is leading to the voltage.

$$E = -jX_c i \qquad 4.11$$

In mathematical terms components of phasors *E* and *I* can be presented in an Argand diagram with the real component on the abscissa and the imaginary component on the ordinate. For a resistor and a capacitor connected in series, the sum of the voltage drops across the elements summaries to the total of E, and can be expressed in phasor notation as:

$$E = E_R + E_c = i(R - jX_c) \qquad 4.12$$

where $Z=(R-jX_c)$ is called the *impedance*.

Applying Euler's relationship impedance *Z* can be represented as a function:

$$Z(\omega) = Z_R - jZ_i \qquad 4.13$$

where $Z_R$ and $Z_i$ is real and imaginary part of impedance respectively.

In case of circuits connected in series, the total impedance is the vector sum of separate elements whereas for parallel connection it is reciprocal of the sum of the reciprocal impedances of each component.

***Impedance-related functions***

Impedance is by definition a complex quantity and it is only real at θ = 0 only in case of pure resistive behavior when the impedance is completely frequency-independent. There are several other functions related to the impedance, such as admittance Y, modulus M and dielectric permittivity ε that received the name *immitances* and often help to understand results. Both admittance and permittivity are parallel functions whereas impedance and modulus are series functions.

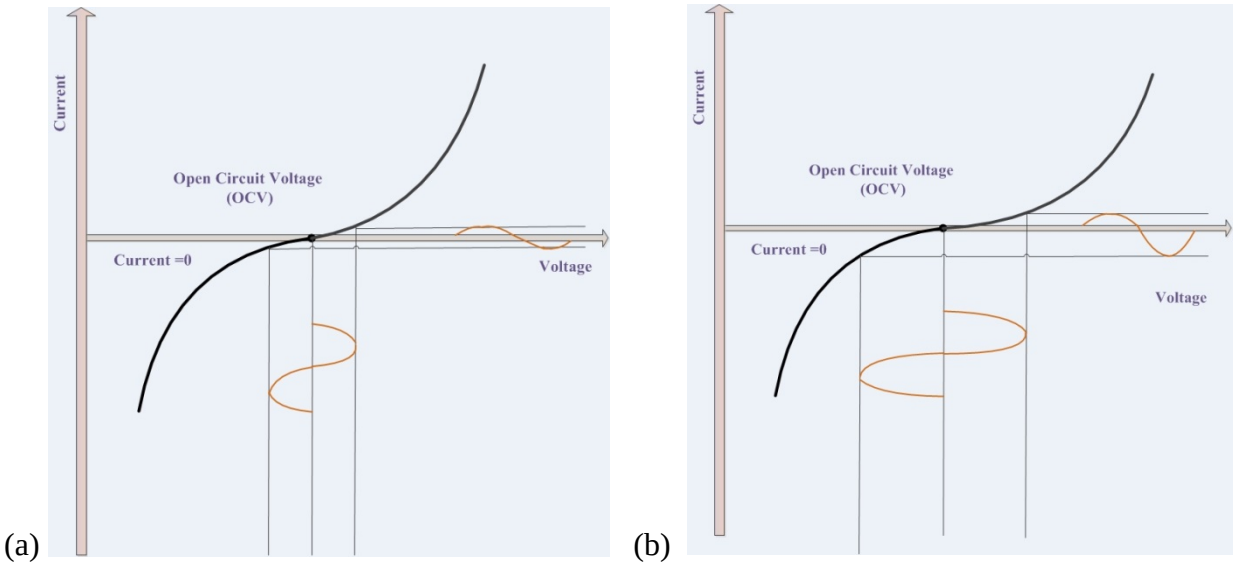


*Figure 4. 2 The DC conditions for the cell and impedance test with (a) linear and (b) non-linear behavior. Reproduced from [*[118]*].*

The actual dc conditions depend on the application while in some cases it is necessary to run impedance tests at the "open circuit" potential of an electrochemical cell (Figure 4. 2), in other cases it may be necessary to set up a particular dc steady state current. It is necessary to remember that small amplitude of a sinusoidal signal (usually 10 mV) should be applied in order to remain within a linear region of the cell (see Figure 4. 2 (b)).

### 4.2.2 Data representation: Nyquist and Bode plot

The graphical format of presentation of IS data is important for correct interpretation and evaluation of the properties of the studied electrochemical systems. The most common presentation of IS data are Nyquist and Bode plots.

#### *Nyquist or Cole-Cole plots*

Impedance plots presented in the complex plane are known as Nyquist or Cole-Cole plots. In the Nyquist plot format, the imaginary part of impedance ($Z_i$) is plotted versus the real component of impedance ($Z_R$) for a wide range of excitation frequencies. Such representation is frequently used especially for electrode or electrolyte studies if the variance of time constants arises from the difference in the capacitance influence of various processes [[115]]. When the data disturbs a

correct fitting of the complex impedance semicircle the Bode format can be used for better interpretation.

***Bode plots***

This format provides detailed information about how the absolute impedance $|Z|$ or its components $Z_i$, $Z_R$ and the phase shift $\varphi$ are changing as a function of frequency. Each peak on Bode plots corresponds to a semicircle in the impedance plane presented by the Nyquist graphical presentation and that is why Bode plots are mainly used in analyses. Example of Nyquist graphical presentation with corresponding Bode plot for a resistor and capacitor connected in parallel is shown in Figure 4. 3.

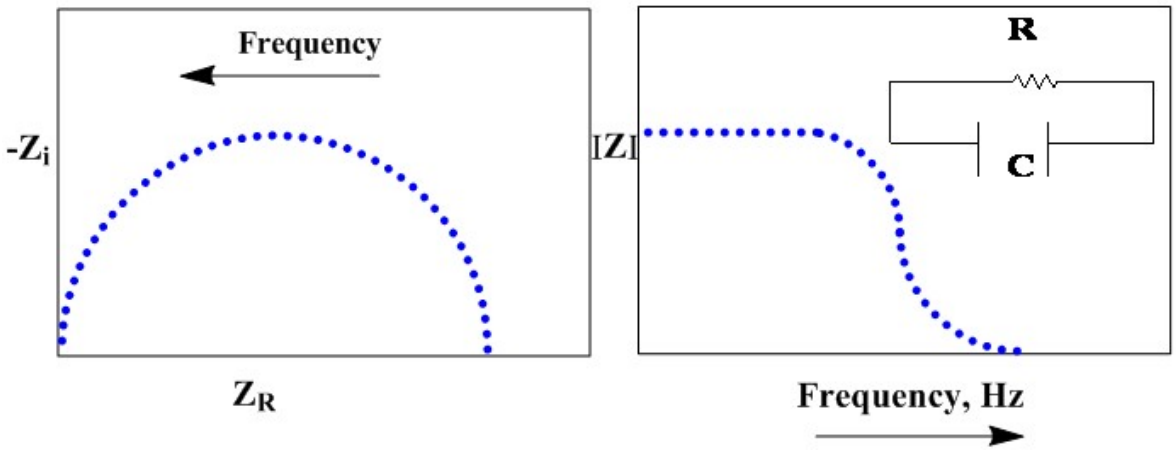


*Figure 4. 3 The graphic presentation of impedance by (a) Nyquist plot and (b) Bode plot for the simple equivalent circuit where resistor and capacitor parallel connected.*

There are several other types of graphical presentation of IS data however they are not widely used within the framework of this project.

### 4.2.3 Resistance of electrolyte and data analysis

Certain distinctions between solid and liquid electrolytes complicates analysis and interpretation of the IS data for solid electrolytes [119].

- While in liquid electrolytes the electronic conductivity is negligible, significant amount of solid electrolytes have electronic conductivity;
- Solid electrolytes can be amorphous, polycrystalline or single crystal;
- In solid electrolytes the mobile ions are able to move in certain conditions for some structural restrictions (for example disordered state of some proton conductors);
- Surface roughness can contribute in features of impedance spectra for solid electrolytes.

The simplest representation of a solid electrolyte system is shown in Figure 4. 4 where the solid cells are described as a series network of parallel connected resistors and capacitors with each representing a different electrode or electrolyte processes.

In reality the impedance of solid electrolyte systems is not well described by the impedance of equivalent circuits with a limited or finite number of ideal resistors and capacitors. The ideal behavior of solid systems is rare and can be described by semicircular arcs with their origin on the real impedance axis (see Figure 4. 4) instead consists of depressed arcs [115]. The depressed arcs are often shifted on the low or on the high frequency end of the impedance spectrum and such behavior indicates the heterogeneity of the system as well as the distribution of time constants. By including into simulation the constant-phase element *Q* (CPE) [120,121], the heterogeneity of the system can be simulated.

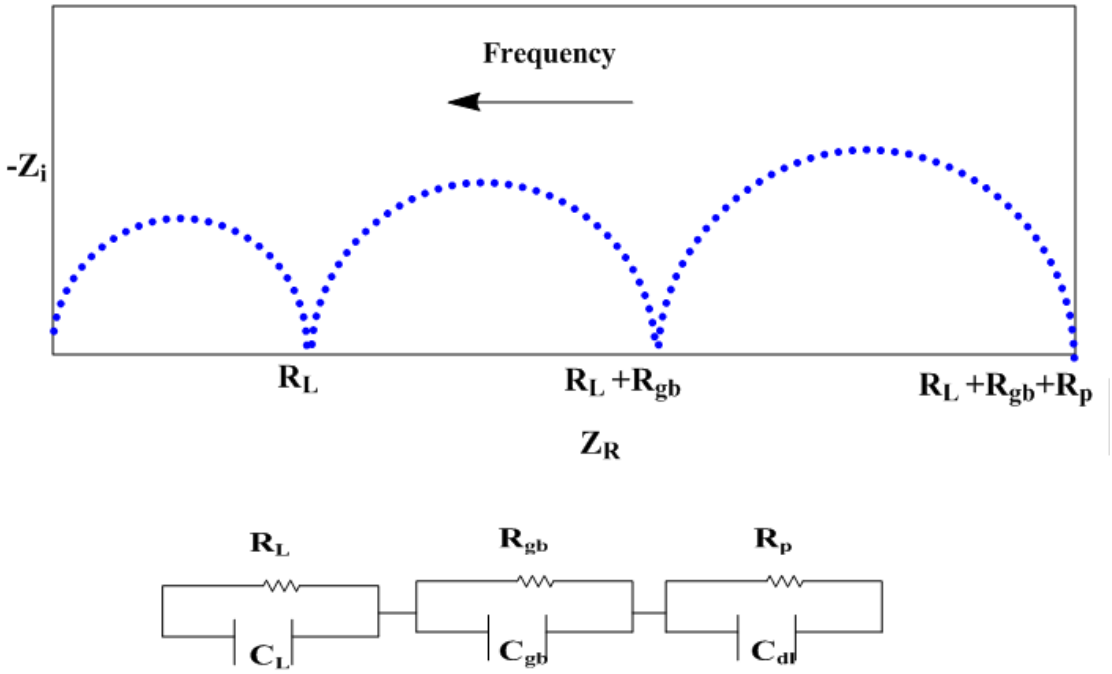


*Figure 4. 4 A simple model representing the general case of solid electrolyte cells with corresponding equivalent circuit and Nyquist plot where $R_L$, $C_L$, $R_{gb}$ and $C_{gb}$ are resistances and capacitances for the bulk and grain boundary electrolyte while $R_p$ and $C_{dl}$ are the electrode polarization processes[Reproduced from [115]].*

***Influence of grain boundary conductivity***

While it is possible to make a better interpretation of the IS data for simple circuits, different contributions in reality significantly complicate the IS response of solid systems and quite often can hardly be separated by fitting. For a powder sample along with a bulk conductivity $R_L$ (described as $R_1$ in the equivalent circuit in Figure 4. 5) the effect from grain boundary conductivity pathes is often can be met. The grain boundary conductivity can be both parallel to the grains $R_2$ and in series with them $R_3$ (often case for proton conducting hydrate Table 1. 3).

$$R_1 < R_2 < R_3 \qquad 4.14$$

$$R_2 < R_1 = R_3 \qquad 4.15$$

Two situations can be discussed together for the case, equation 4.14, (see Figure 4. 5 (a)) and equation 4.15 (see Figure 4. 5 (b)). The bulk resistance can be extracted only in case of equation 4.14 when the grain boundary resistance $R_3$ is much higher than the bulk resistance $R_1$ and will corresponds to a first semicircle on the Nyquist plot. Otherwise the bulk conductivity may be short circuited by the grain boundary effect 4.15 and the first semicircle in the impedance spectrum can be concealed Figure 4. 5 (b).

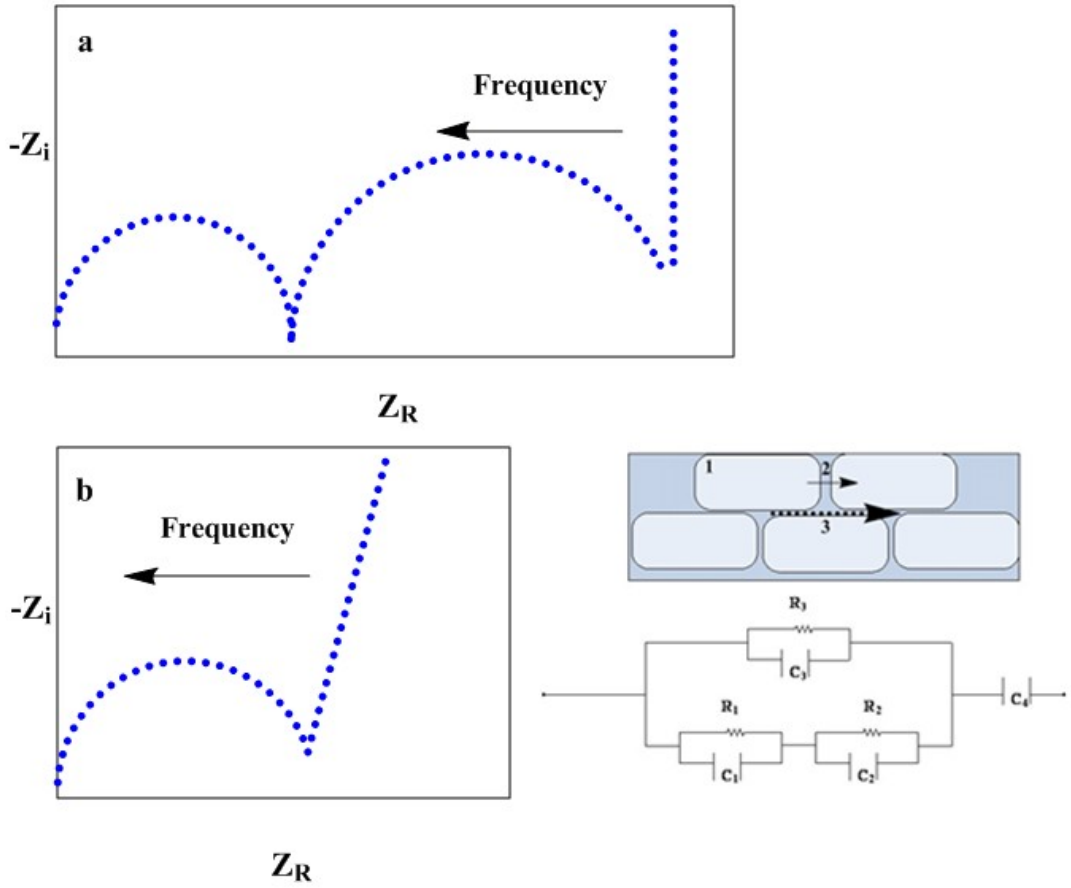


*Figure 4. 5 Simulated Nyquist plots of proton conducting systems where presented an influence from contributions of the bulk conductivity 1; the grain boundary conductivity in series 2; and parallel to the grains 3 and a simple equivalent circuit describing this case. [Reproduced from [18]].*

***Impedance in the presence of diffusion (Warburg impedance)***

The total impedance of electrochemical system consists of the contributions of the electrolyte, the electrode solution interface, and the electrochemical reactions taking place on the electrode [122]. It is possible to write impedance for any mechanism. For the diffusion process the total faradaic impedance $Z_f$ [122] for reaction *4.16* can be expressed as *4.17*:

$$O_X + ne \leftrightarrow Red \qquad 4.16$$

$$Z_f = \frac{RT}{n^2F^2}\frac{1+\frac{k_f}{\sqrt{j\omega D_o}}+\frac{k_b}{\sqrt{j\omega D_R}}}{\alpha k_f C_0(0)+(1-\alpha)k_b C_R(0)} \qquad 4.17$$

where $k_f$ and $k_b$ are the potential-dependent rate constants for the forward and backward reactions; $C_0(0)$ and $C_R(0)$are the surface concentrations of the forms $O_X$ and Red and $D_0$ and $D_R$ their diffusion coefficients; α is the transfer coefficient, n is the number of electrons.

The total faradaic impedance $Z_f$ consists of three terms:

- the derivative $\frac{\partial i}{\partial E}$ is called the *charge-transfer resistance*, $R_{ct}$;

- the two other contributions from $\frac{\partial i}{\partial C_i}$ are called *impedances of mass transfer*, $Z_W$ which in case of semi-infinite diffusion is referred as a semi-infinite Warburg impedance.

$$Z_f = R_{ct} + Z_W = R_{ct} + Z_{W,O} + Z_{W,R} \qquad 4.18$$

The mass transfer impedance may be written as *4.19*:

$$Z_W = \sigma\omega^{\frac{-1}{2}} - j\sigma\omega^{\frac{-1}{2}} \qquad 4.19$$

On the complex plane plot, the Warburg impedance looks like a straight line with a slope of 1 and intercept with the $Z_R$ axis at a $45^o$ angle Figure 4. 6 (Randles model). The Warburg impedance cannot be represented by a connection of simple R and C elements because of power of angular frequency ( $\omega^{\frac{-1}{2}}$ ) and thus in equivalent circuit representation is described by the Warburg element *W*.

In many cases diffusion is not semi-infinite [122]. The diffusion which often observed in conducting polymers or porous electrodes limited by reflection and called the reflective finite diffusion Figure 4. 6 (b) while metal totally covered with oxide will displays another feature and diffusion in this case referred as the finite or bounded Warburg impedance Figure 4. 6 (c).

In solid proton conductors, the electrode reaction takes place between electrode, electrolyte and gas atmosphere and the thickness of the gas layer is small in comparison with the pore size of the electrode. The diffusion process is limited by this layer and defined by penetration depth. At high frequencies influence of the penetration depth is small with respect to the thickness and the diffusion proceeds in semi-infinite conditions. In this case classical Warburg impedance is usually used [115].

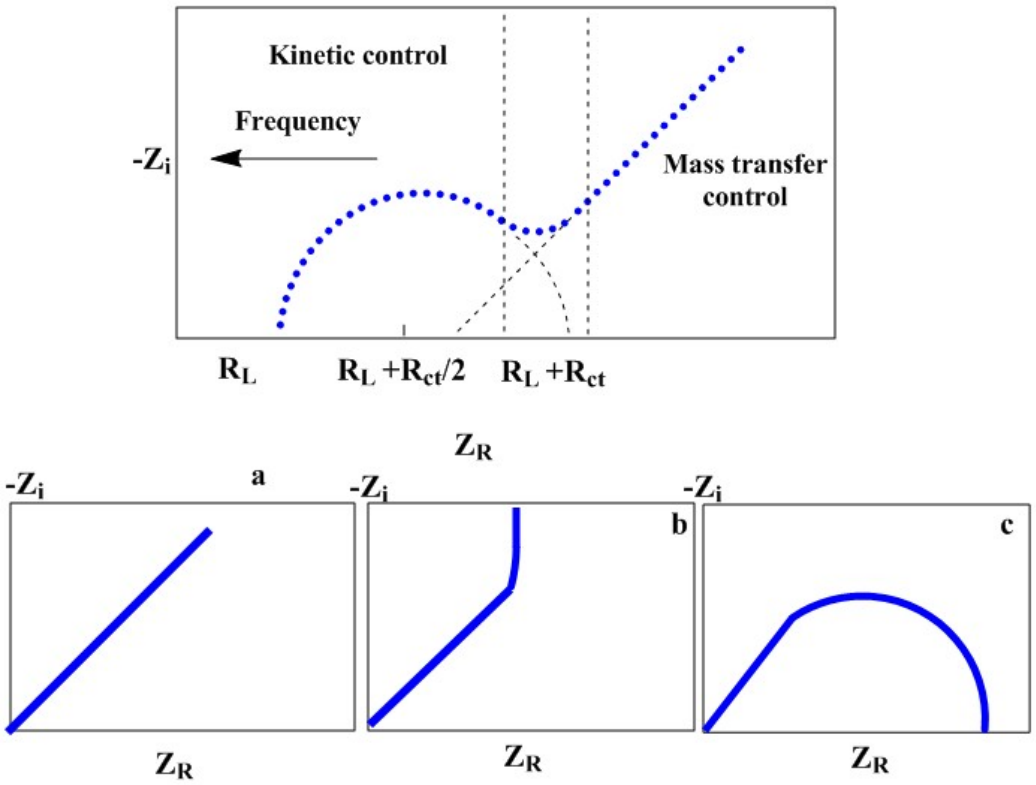


*Figure 4. 6 Nyquist plot of electrochemical cell with variation of impedance for diffusive systems: a semi-infinite diffusion; b-reflective finite diffusion; c- transmissive finite diffusion [Reproduced from [119]]*

## 4.3 Cell design and construction

Through this project, significant efforts were made for design and construction of conductivity cells that are suiting for the present study. This section is devoted to sharing the knowledge and experience that were learnt. Generally speaking, there are three main technical requirements for the present project. First of all, the intermediate temperature range between 200-400 $^{o}$C requires that all constructional parts of conductivity cells have to be stable and suitable when assembled together.

Secondly the proton conductivity strongly depends on the atmosphere in which the measurement is carried out. Particularly the atmospheric humidity should be well defined as it is the

most crucial for the proton conductivity. For this purpose, any condensation has to be completely avoided in the entire conductivity cell including all tubing and joints. And of course all constructional parts should be chemically stable when exposed to the water vapor in the temperature range of interest. From the beginning it was decided that the conductivity cell should be contained in a gas tight chamber for the atmosphere/humidity control. The length of the chamber played a role in reaching the gas-water equilibrium otherwise pre-evaporation or preheating should be introduced.

The last and most crucial and difficult is to ensure good electrical contact between the leading wires/holders and samples during the assembling at room temperature and the following heating. A mismatch of thermal expansions of the sample and the holders would result in either poor contact or breaking the sample. Additional joints in the cabling and wiring may also result in noisy impedance spectra.

The contact problem is even worse considering the fact that most of phosphate samples are rather soft with difficulties in fabrication and handling. It turns out that the first cell design, though operational at temperatures of up to 250 $^{o}$C with well-defined gas conditions, was not sufficiently precise for samples with a conductivity above 0.01 S•cm$^{-1}$. It should be mentioned that precision of one order of magnitude is a general problem of conductivity measurement by IS technique.

In this following, the sample holder, assembling and the cell chamber design are briefly described.

### 4.3.1 Sample holders

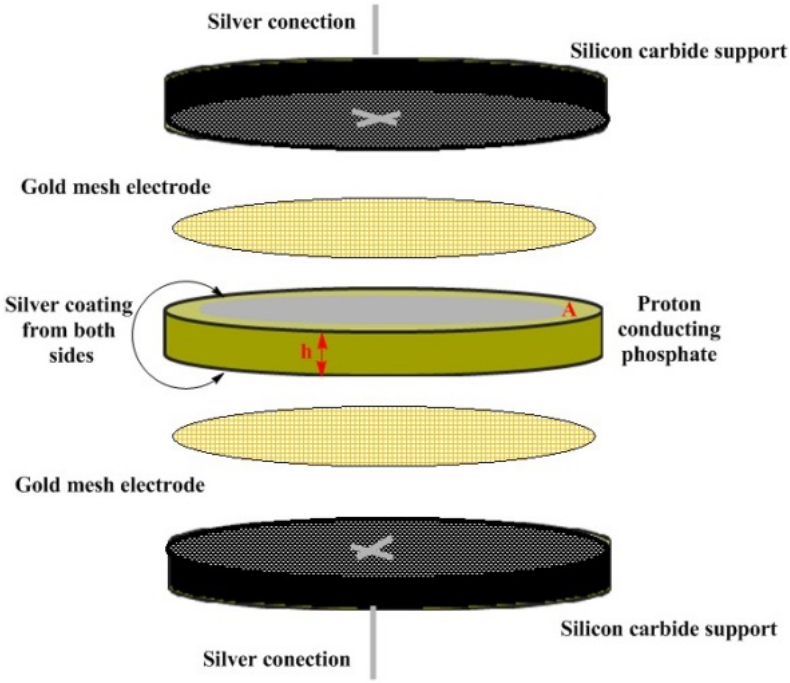


*Figure 4. 7. Schematic representation of assembling sample in cell holder*

The sample holder used in conductivity cells of different designs is shown in Figure 4. 7. The disc sample with a section area of $A$ cm$^2$ and a thickness of $h$ cm is prepared by dry pressing of

powders. The two sides of the disc are brushed with a conductive silver paste LOCTITE® 3863 from Henkel Co. The coated phosphate sample is then attached to two gold meshes acting as current collectors. On the back side of each gold current collector is a porous silicon carbide substrate, allowing the access of humidified air during the measurement. The conductivity (σ) of the disc was calculated by (4.20):

$$\sigma = \frac{h}{RA} \qquad 4.20$$

where *h* is the thickness, A is the section area, and R is the measured resistance.

### 4.3.2 Three types of conductivity cells

The first cell design was featured by hanging a balance weight (of 2.4 kg) on the holders of the sample. The weight ensures good contact between the porous supporting substrates, metal meshes and the pellet sample, as shown in Figure 4. 8. This design avoids tightening screws during the sample assembling in the cell. When the cell is heated to higher temperatures for the conductivity measurement, a constant force is maintained to keep the electrical contact between all assembling parts of the sample. The obtained impedance curves are less noisy particularly for samples with low conductivities. One shortcoming of this cell is less flexible in tightening when samples of different hardness are measured. In case a sample is broken, the porous carbide plates are contaminated and should be replaced. Another disadvantage is a long time required for heating and reaching equilibrium when the atmospheric humidity is varied, because of the metal weight and the long cell chamber.

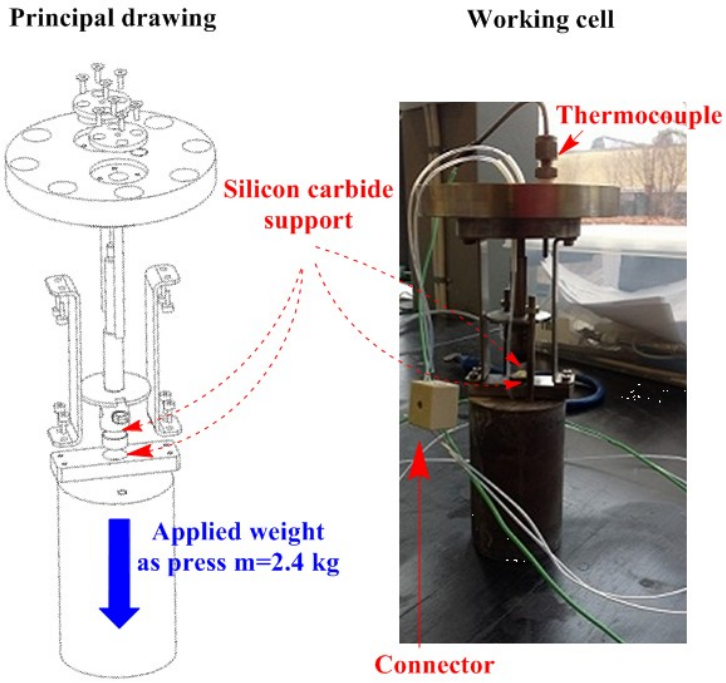


*Figure 4. 8 Design of the conductivity cell with a balance weight*

In another design, the sample holders are fixed between two stainless steel plates with a central opening to fit the sample pellet, as shown in Figure 4. *9*. The two stainless steel plates are mounted with help of four screws. Careful tightening of the screws is needed as the thermal expansion of the samples and assembling parts occurs during the following heating and stress may develop. Anyway varied extents of tightening are optional, which is of importance for different types of phosphate samples. The cell is simple in construction and easy to replace parts if needed. However good contact should be ensured manually otherwise conductivity results can be obtained with a variation of almost one order of magnitude, particularly for samples of high conductivity.

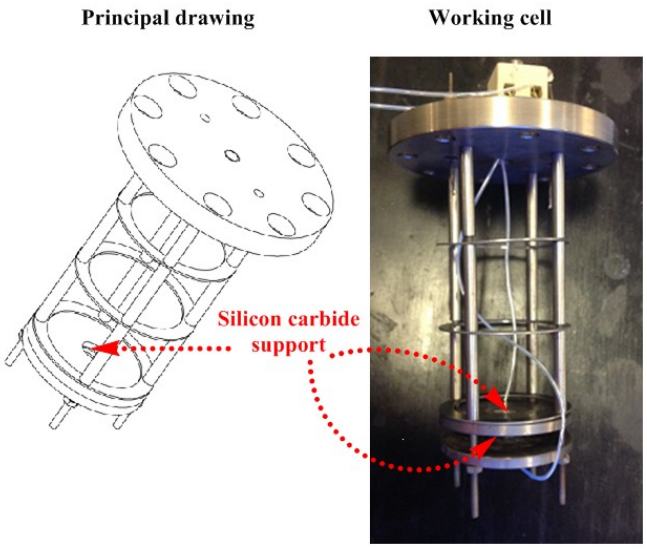


*Figure 4. 9 Design of the conductivity cell with the sample holder mounted to metal plates by screws.*

Further improvement of the cell design is made by using a sample assembly, as shown in Figure 4. 10. The sample pellet, metal meshes and carbide holders are assembled by stainless steel plates with fixed leading wires. This sample assembly as a whole piece is then mounted to the frame of the cell chamber. In this way, a conductivity cell chamber may contain three or more sample assemblies, each having two electrode leads for connection to the Potentiostat. Also in this type of cells, the insulation of the wires, which are made of polytetrafluoroethylene (PTFE) in the previous deigns, is replaced by ceramics so that the conductivity measurements can be done at temperatures of up to 400$^{o}$C.

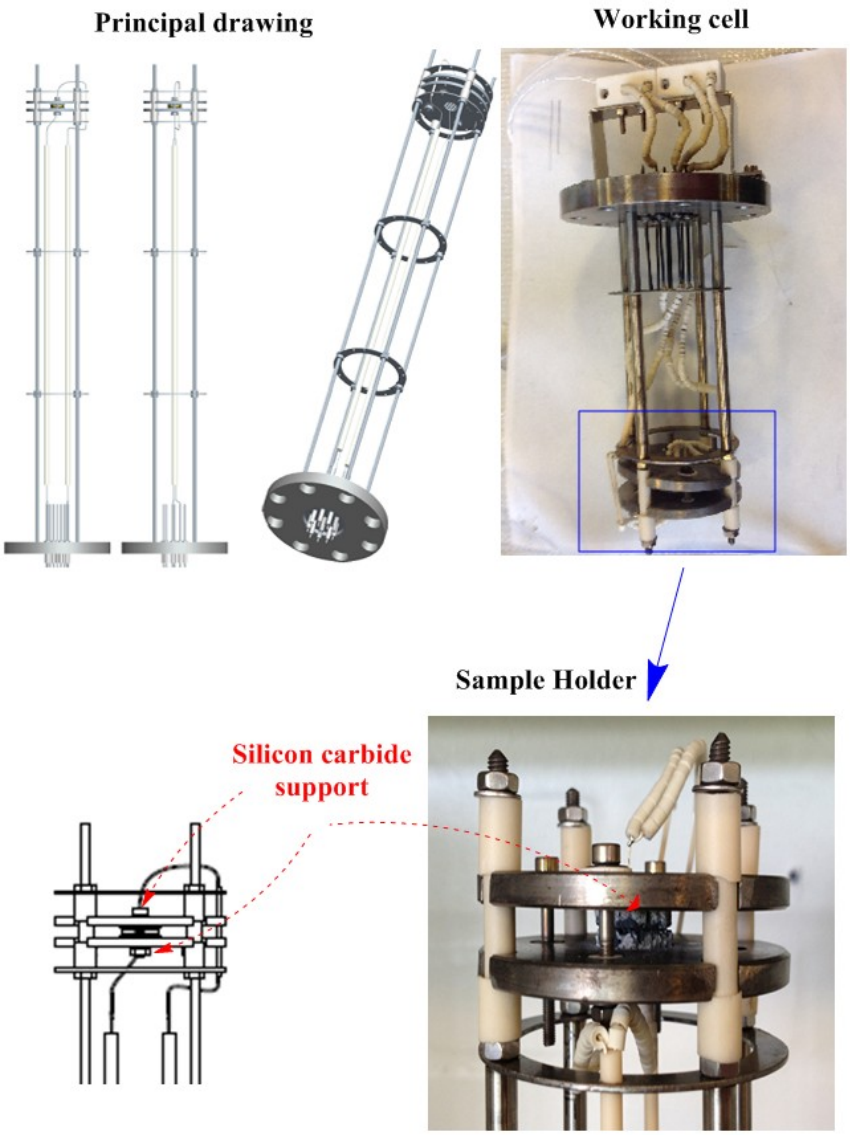


*Figure 4. 10 Design of cell type 3 with view of holder part where assembled sample located during measurement and scheme of improved connection.*

Eventually the fuel cell or electrolyser hardware is used for conductivity measurements. The cell consists of two endplates with gas channels and inserted heating elements and thermocouple. Through the gas channels, humidified gases are supplied for the humidity control. To simplify the operation, the same gas steam is used for the two sides of the sample, i.e. the humidified gas flows from side to the other, as shown by black dot lines and arrows in Figure 4. 11. The inserted heating elements allow fast heating and even thermal cycling of the cell. In the cell, gas tight sealing is achieved using Capton® films as gaskets. These are placed in the way to reach a total thickness corresponding to the thickness of the assembly of the sample and the both electrodes.

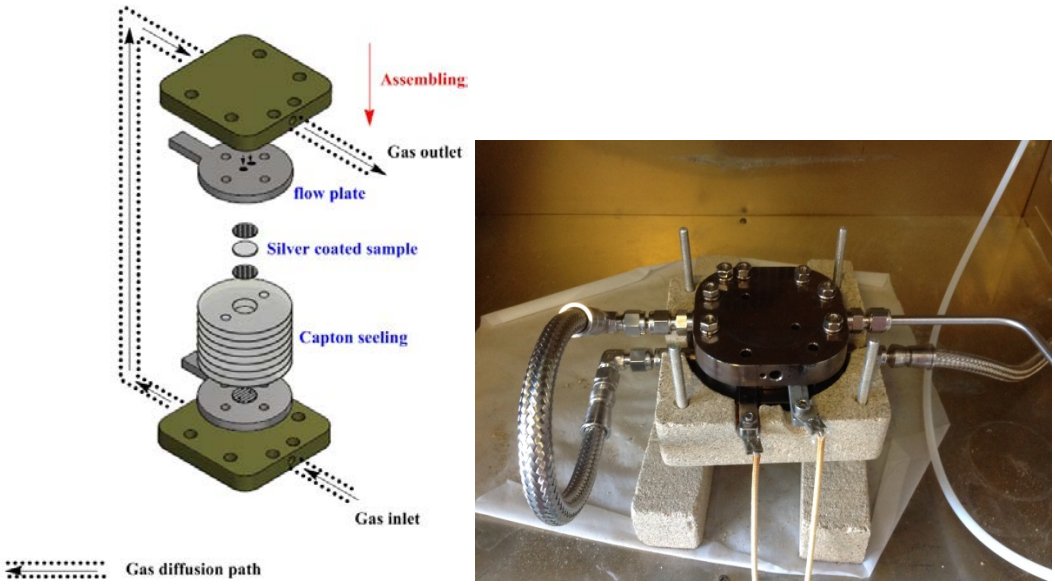


*Figure 4. 11 Simplified presentation of assembling fuel cell type conductivity cell with photo of the cell in assembled station.*

## 4.4 Furnaces, humidity control and impedance measurements

A typical conductivity measuring system is schematically shown in Figure 4. 12. The decompressed air from 7 bar is used as the carrier gas, which is defined as “dry air” when not humidified. To achieve humidified atmosphere, an air flow, controlled by a Brooks Instrument 0254 mass flow meter, is mixing with a water flow from a Shimadzu Prominence LC-20AD water pump through an evaporator. The evaporator is located inside the furnace where the conductivity cell is placed, which means the evaporation temperature is the same as the conductivity cell temperature. In this arrangement, conductivity measurements below 100 $^{o}$C are made only under unhumidified conditions. The furnace temperature is controlled by a temperature controller (Eurotherm 2416) that can be programed.

Impedance spectra of the samples were measured by a Princeton Potentiostat Versa Stat 3(4) equipped with the Versa Studio software. The measuring frequency range was between 0.01 Hz and 1 MHz however in most cases the high frequency range was limited by 0.5 MHz (calibrated by dummy cell).

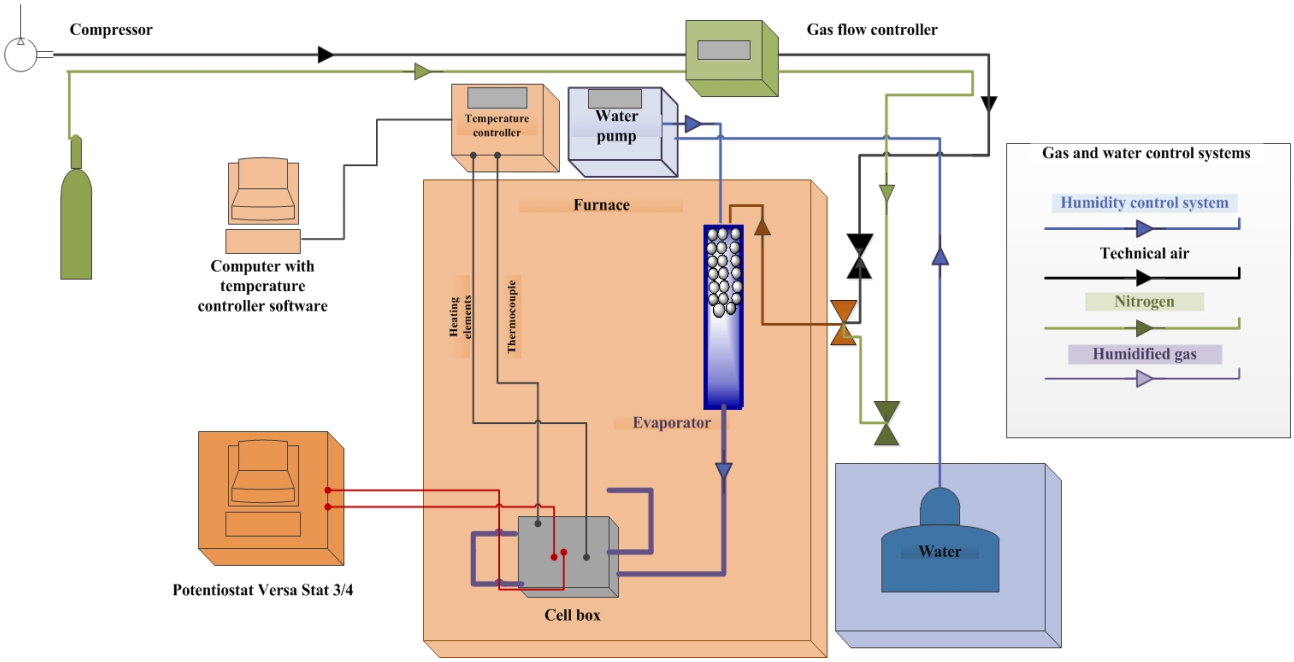


*Figure 4. 12. Modified system for conductivity measurements described by schematic representation.*

# Chapter

# 5 Structural, thermal and conductive properties of rare earth metal orthophosphate hydrates

Metal phosphate hydrates are a large class of materials, some of which exhibit good protonic conductivity. These materials have very interesting electrochemical properties often combined with other characteristics such as possibility to obtain thin films. The liquid like organization (not well studied) of OH groups between layers have possibility to facilitate proton transfer (quasi liquid proton transfer mechanism). The protons of the OH group can move on the surface and trough the bulk. However research of structure and proton transfer of phosphates hydrates materials has been very limited.

The rare earth metal phosphates exist in nature as monoclinic monazite and tetragonal xenotime. The formula is in both cases $MPO_4$, but monazite preferentially incorporates larger rare earth elements from La to Gd, while the tetragonal xenotime ($MPO_4$) tends to incorporate the smaller rare earth elements, typically Y [123]. In their hydrated form ($MPO_4 \cdot nH_2O$) with a typical stoichiometry of $n < 3$, the phosphates adopt the hexagonal rhabdophane crystal structure (see Figure 5. 1).

Most work on proton conductivity has been carried out on rare earth metal orthophosphates with the monazite structure (discussed previously in Chapter 2). Chemically, rare earth metal phosphates show tendency of forming compounds of high complexity and with high phosphorus contents. This can be achieved by sharing the corner oxygen atom with the adjacent $PO_4$ tetrahedra. For example, in the $La_2O_3$-$P_2O_5$ binary phase system, condensed phosphates of $La(PO_3)_3$ and $LaP_5O_{14}$ are well known [124]. Recent efforts are being made to explore the proton conduction in these polyphopsphates. Ray et al. [125] prepared $LaP_3O_9$ and $CeP_3O_9$ glasses and obtained conductivities of $10^{-7.5}$ – $10^{-6}$ $Scm^{-1}$ at 400°C. Similar to the orthophosphates, when lanthanum ions were partially substituted by divalent metal ions such as $Ca^{2+}$, $Sr^{2+}$ and $Ba^{2+}$ [126,127], higher proton conductivities were reported for the polyphosphates, indicating that the substitution leads to proton dissolution into the material and induce protonic conduction. The highest conductivity of $5\times10^{-4}$ $Scm^{-1}$ was reported for 3 mol% Sr-doped $LaP_3O_9$ at 427 °C [128]. Further condensed phosphates in form of e.g. $LaP_5O_{14}$ are believed to provide low energy avenues for proton transport and therefore lead to enhanced conductivity [129,130,131].

These condensed phosphates are well known to undergo phase transformations with temperature. For example, during the synthesis by solution routes, Jørgensen et al. [132] found that the residues of hydrogen phosphates in form of adsorbed surface species led to formation of

lanthanum metaphosphate ($LaP_3O_9$) upon heating to above 600 $^oC$. The $LaP_3O_9$, in turn, decomposed to $LaPO_4$ with loss of $P_2O_5$ at temperatures above 877 $^oC$ and even transformed to an amorphous phase.

Another type of structural transformation of rare earth phosphates is between the monoclinic monazite ($MPO_4$) and hexagonal rhabdophane ($MPO_4 \cdot nH_2O$) through hydration and dehydration[133]. The naturally occurring rhabdophane is of a significant variety of the rare earth metal compositions [134], where the water molecule is accommodated in the "zeolitic" channels of the structure [135]. This type of phosphate structures is metastable. It dehydrates when heated to elevated temperatures and further transforms to the monazite structure at even higher temperatures. The presence and stability of the hydrate water in the rhabdophane phosphates are of particular interest from the proton conductivity point of view.

## 5.1 Structural modeling

Figure 5. 1 shows the structure for neodymium phosphates as calculated from the XRD data.

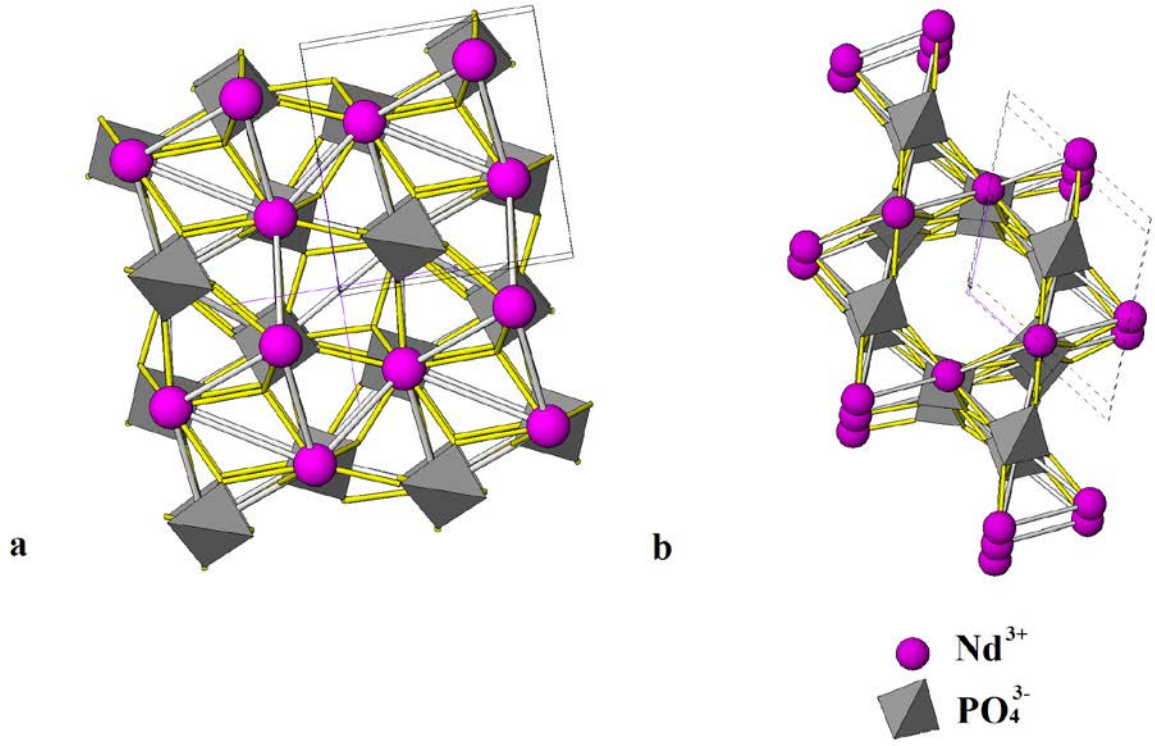


*Figure 5. 1 View of the $NdPO_4$ structure along the c-axis. a) The monoclinic monazite structure and b) the hexagonal rhabdophane structure with channels that can accommodate water (not shown).*

The crystal structure of $NdPO_4$ as seen along the c-axis is shown in Figure 5. 1 (a). It consists of isolated $PO_4$ tetrahedra, which are held together by $Nd^{3+}$ cations. Each $Nd^{3+}$ cation is surrounded by nine oxygen ions. The crystal structure of the hydrated form of $NdPO_4$ (rhabdophane) seen along the c-axis is shown in Figure 5. 1(b). The location of water molecules is suggested by use of geometrical considerations. According to Mooney [135], adjacent sites are only 2.15 Å apart along the hexagonal axis and are assumed to preclude the occupancy of every unit cell by a water molecule. At the maximum, only half of the sites can be occupied, or in other words, there can be only one and a half molecules of water per unit cell. Therefore, if water is present in the crystal structure there should be no more than half a molecule per rare earth metal atom. The location of water molecules is only possible on the $6_2$ axes, in rows. The existence of such unoccupied spaces explains the relatively low density of the hexagonal isomorph as compared to the monoclinic monazite (see Table 5. 1). Mooney [135] also suggested that the crystal structure of $NdPO_4 \cdot nH_2O$ may be stabilized by the presence of water in the interstices. These sites could accommodate a neutral molecule of water or even ions of a suitable size if the charges could be compensated in some ways. An ionic radius depends on the coordination number, spin state and other parameters. The effective ionic radius of trivalent lanthanides in the eight and nine-fold coordination are given in Table 5. 1. In the table are also listed the lattice parameters of these phosphates, which are also plotted as a function of the ionic radius in Figure 5. 2.

*Table 5. 1 Crystal radius of trivalent lanthanide ions in eight and nine coordination as compared to the unit cell dimension of monazite and rhabdophane orthophosphates. Theoretical data have been taken from corresponding references. Measured densities are listed too.*

| Name | Effective Ionic Radius of $M^{3+}$ [136,137], nm | | Unit Cell Dimension, nm | | Density, g/cm$^3$ | |
|---|---|---|---|---|---|---|
| | In eight coordination | In nine coordination | a | c | Theoretical | Experimental (this work) |
| $LaPO_4$ [138] | - | 0.1216 | 0.6825 | 0.6482 | 5.11 | - |
| $LaPO_4 \cdot nH_2O$ [139] | 0.1160 | - | 0.7081 | 0.6468 | 4.15 | 4.13 |
| $NdPO_4$ [140] | - | 0.1163 | 0.6732 | 0.6383 | 5.49 | - |
| $NdPO_4 \cdot nH_2O$ [139] | 0.1109 | - | 0.698 | 0.638 | 4.45 | 4.02 |
| $GdPO_4$ [141] | - | 0.1107 | 0.6621 | 0.631 | 6.06 | - |
| $GdPO_4 \cdot nH_2O$ [142] | 0.1053 | - | 0.6906 | 0.6326 | 5.05 | 4.68 |

Figure 5. 2 illustrates differences in unit cell parameters both for monazite (monoclinic) and rhabdophane (hexagonal) structures as well as gadolinium contraction. It can be seen from the figure that the parameters a and c of the unit cell are larger for the rhabdophane structure than for that of the monazite. This can be explained by channels present in the rhabdophane structure, which are accommodating water molecules. When water molecules are leaving the channels during the heating, the rhabdophane type unit cells contract in order to compensate the open space and transform into the more dense monazite type structure.

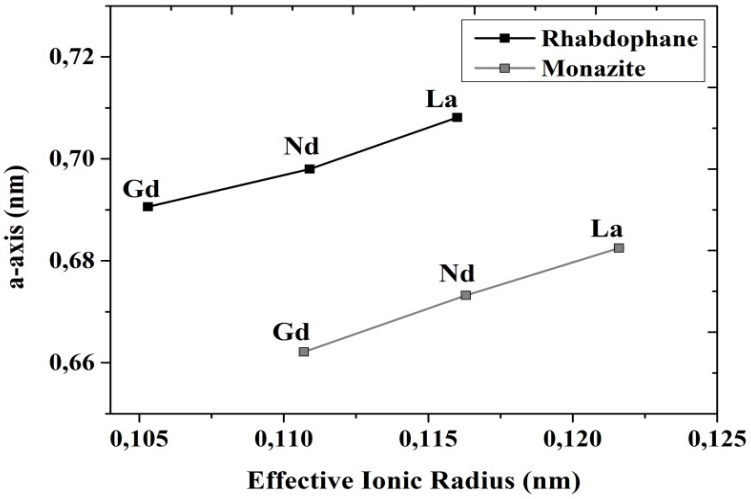


A

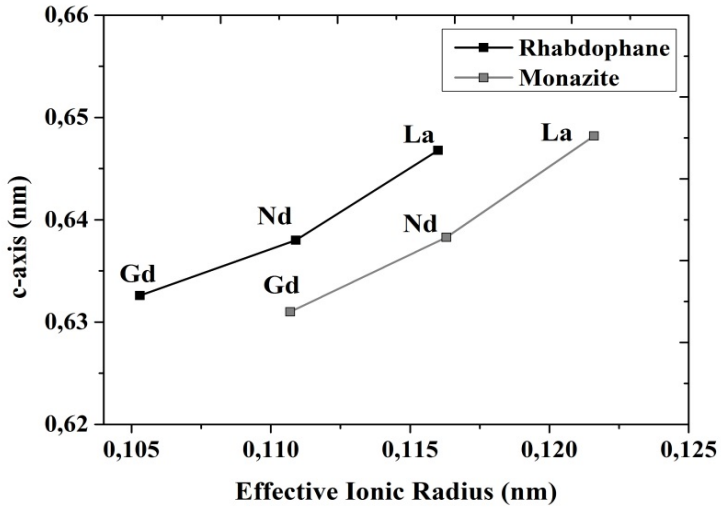


B

*Figure 5. 2 a-axes (a) and c-axes (b) of the rhabdophane $MPO_4 \cdot nH_2O$ and monazite $MPO_4$ unit cells plotted against effective ionic radius of the corresponding lanthanide.*

This process is believed to be slow and energy consuming. After such a transformation it would be difficult for the water molecules to be introduced into unit cells again because of the contraction.

## 5.2 XRD

The hexagonal structure is the low-temperature phase stabilized by hydrate water. The assigned peaks are marked on the X-ray diffraction patterns of unheated samples (Figure 5. 3, open circles). Wide peaks are a typical feature for $MPO_4 \cdot nH_2O$ powders and it is an indication of low crystallinity of the unheated samples. The crystallinity is increasing slightly with temperature until the transition temperature. No presence of the monazite phase (crosses) was observed in the X-ray diffraction patterns of $NdPO_4 \cdot nH_2O$ after the heat-treatments at below 650 $^oC$. The X-ray diffraction pattern of the powder heat-treated at 650 $^oC$ showed the presence of both rhabdophane and monazite structures. Finally at 800 $^oC$ the crystalline phase of the rhabdophane disappeared. The X-ray diffraction patterns of the $LaPO_4 \cdot nH_2O$ and $GdPO_4 \cdot nH_2O$ showed the same behavior. It is noted that for the $LaPO_4 \cdot nH_2O$ powder by heat treatment at temperatures up to 350 $^oC$ contained three additional peaks in the 2θ region from 10 to 30$^o$, which were not recognized by the data base and suggested to be due to contamination by the churchite phase ($LaPO_4 \cdot 2H_2O$).

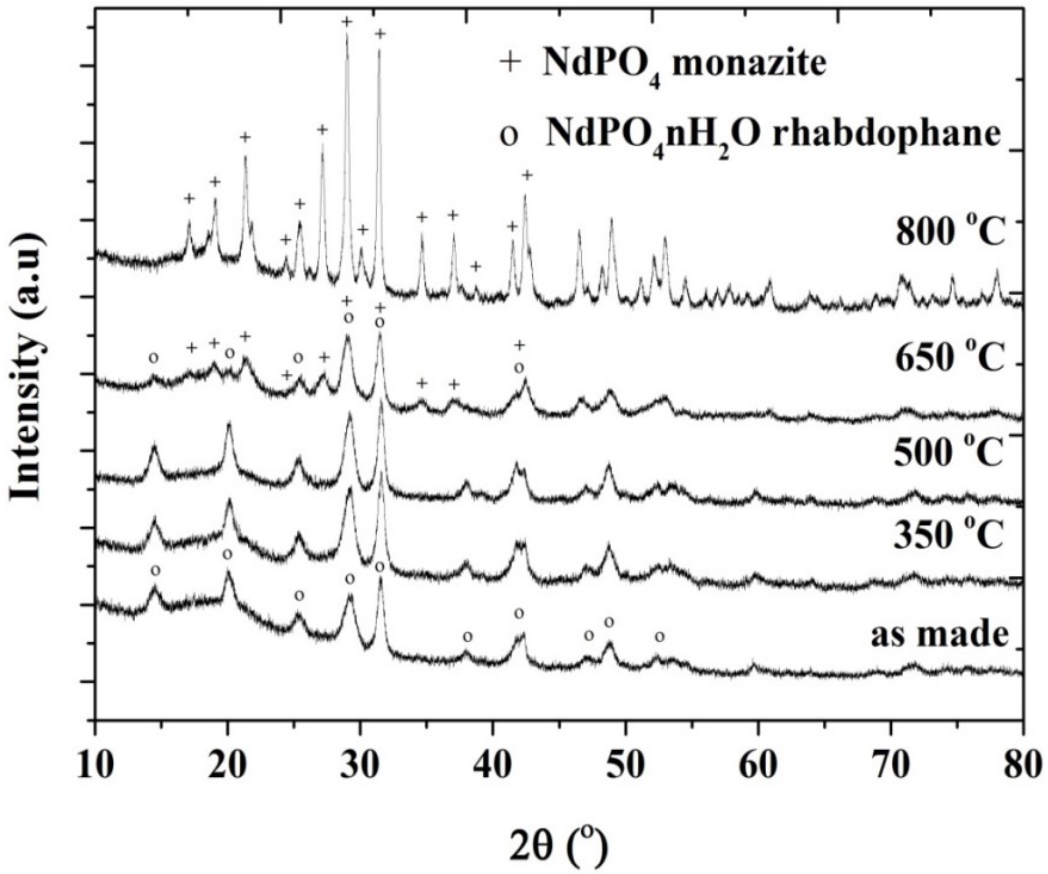


*Figure 5. 3 X-ray diffraction patterns of $NdPO_4 \cdot nH_2O$ powders as prepared and heat treated at different temperatures each for a period of 6 hours. Indexing for rhabdophane [135] and monazite [140] structures is indicated in the figure.*

## 5.3 FT-IR spectra

Infrared spectroscopy has proved to be an important tool for determining the different structures of rare earth phosphates. The space group of the hexagonal form of the $MPO_4 \cdot nH_2O$ is *P*6222 [139]. This space group provides sets of three-fold sites with the point symmetry $D_2$ for the metal and phosphate ions, and six-fold sites with the point symmetry $C_2$ for phosphates [143]. The nature of vibrations of the phosphate group was described by Assaaoudi [144] for the wheinshenkite-type compounds and for the rhabdophane-type compounds.

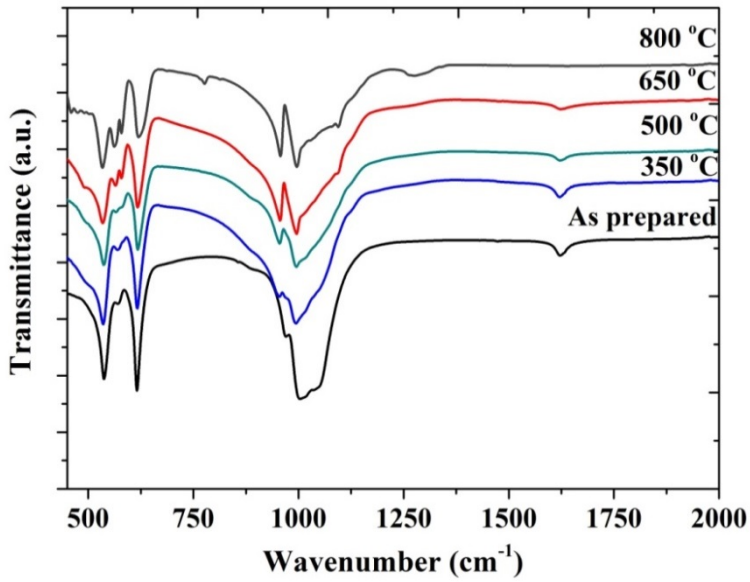


*Figure 5. 4 (a) (b)Typical FT-IR spectra of neodymium phosphate $NdPO_4 \cdot nH_2O$. Temperatures of heat treatment are indicated*

Figure 5. 4 (a) shows infrared spectra of three rare earth phosphates made at room temperature. Aspects of vibrational spectroscopy of inorganic hydrates have been discussed in experimental part. The *v*1 band (P–O symmetric stretch) at 966 $cm^{-1}$[145] appears as a shoulder in spectrum while *v*4 (O–P–O asymmetric bending) appears as a triplet at 542, 570 and 615 $cm^{-1}$ and it is clearly observed for samples $LnPO_4 \cdot xH_2O$ (La, Nd). In case of $GdPO4 \cdot xH_2O$ bands at 523, 542, 630 $cm^{-1}$ were also assigned as vibration of $PO_4$ groups. These bands were shown by Assaaoudi [144] for the sample $GdPO4 \cdot nH_2O$ with rhabdophane- type structure. The *v*3 P-O stretching vibrations were observed at the 990-1100 $cm^{-1}$ region. The band at 1265 $cm^{-1}$ belongs to $P_2O_7^{4-}$ ions and often can be seen at rare earth phosphates spectra of powders received by wet precipitation method from phosphoric acid solutions.

The band at 1631 $cm^{-1}$ was assigned to the hydration water of the hexagonal $MPO_4 \cdot nH_2O$ [133]. FT-IR spectra in Figure 5. 4 shows a decrease of this band indicating loss of water in $NdPO_4 \cdot nH_2O$ at high heat-treatment temperatures. Similar behaviors were observed for the other two phosphates (not shown). The characteristic water band can be observed at temperatures up to 650 °C. Thus together with X-ray diffraction pattern studies this result proves that the rhabdophane phase can be present in the structure at temperatures up to 650 °C and partly recoverable during the cooling process under ambient atmosphere by accommodation of water molecules into the structure. Another interesting region is in the range of 500 - 600 $cm^{-1}$ where peaks connected to the vibration of $PO_4$ groups are located. The presence of three clear peaks on the FT-IR spectra for the sample heat threated at 650 °C is characteristic of the vibrations of phosphate groups in the monoclinic

structure of monazite structured $NdPO_4$ and assumed to result from the distortion of the tetrahedral phosphate groups in the nine fold coordinated Nd atoms [140].

## 5.4 TG/DT Analyses

### 5.4.1 Thermal stability in air

The samples were studied by DTA/TGA analyses in order to determine the amount of residual water in the powders. Using the heating program, powders were heated up to 800 °C with a constant heating speed of 10 K/min in air and the main mass losses caused by removal of water from the initial powders were observed until 500 °C (see Table 5. 2). The TGA/DTA results are shown in Figure 5. 5.

The occurring weight loss could be divided in three regions. In the first region below 200 ˚C, a weight loss of about 3.5-4 wt% accompanied by an endothermic peak with a maximum at about 100-140 ˚C is assumed to be associated with the water adsorbed on the surface (see Table 5. 2) during the storage in air. It is likely that the amount of the adsorbed water depends on the surface area of powders. Powders of lanthanum and neodymium phosphates have higher surface areas than that of gadolinium phosphates (see *Table 5. 2*), which might be explained by differences in the particle size of initial oxides and therefore the obtained phosphates. It must be taken into account that the surface area affects the content of nonstoichiometric water and therefore most likely the conductivity of the phosphates too. This is clearly seen for the $GdPO_4 \cdot nH_2O$ sample as the powder has a low surface area and hence low water adsorption.

The second event between 200 - 500 $^oC$ with a corresponding endothermic maximum at around 200 - 250 $^oC$ is assigned to the dehydration of the hexagonal phase ($MPO_4 \cdot nH_2O$). An important weight loss was registered before 300 $^oC$ which continued at temperatures up to 450 $^oC$. The total weight loss of this event was found to be dependent on the synthesis conditions and corresponded to a hydration ratio, n, of around 0.5 for the phosphates. The additional endothermic peak for the $LaPO_4 \cdot nH_2O$ sample in the 300-350 $^oC$ region was not recognized in the neodymium and gadolinium phosphates, most likely due to the presence of phase impurities as revealed by X-ray diffraction analysis.

The last event above 450 $^oC$ with an exothermic peak at about 500 $^oC$ was not accompanied by significant mass losses and presumed to represent the beginning of transformation from the rhabdophane to the monazite structure. This phase transition was supported by the X-ray diffraction analysis in Figure 5. 3 and FT-IR in Figure 5. 4. The structural differences between these two phases have been described previously. The temperature of this transition is higher in this case than previously reported by others [133], which can be explained by the fast heating rate (10 K/min). The

exact temperature of the structural transition is strongly depending on initial conditions of the synthesis and the amount of nonstoichiometric water.

The results of the TGA measurements are summarized in Table 5. 2. It is clear that the first TGA event at up to 150 °C corresponds to the release of adsorbed water. This part of water loss is of surface nature and dependent on the specific surface area of the phosphates not including the channels. The second event in the temperature region from 200 to 500 °C is due to the dehydration of the rhabdophane phase.

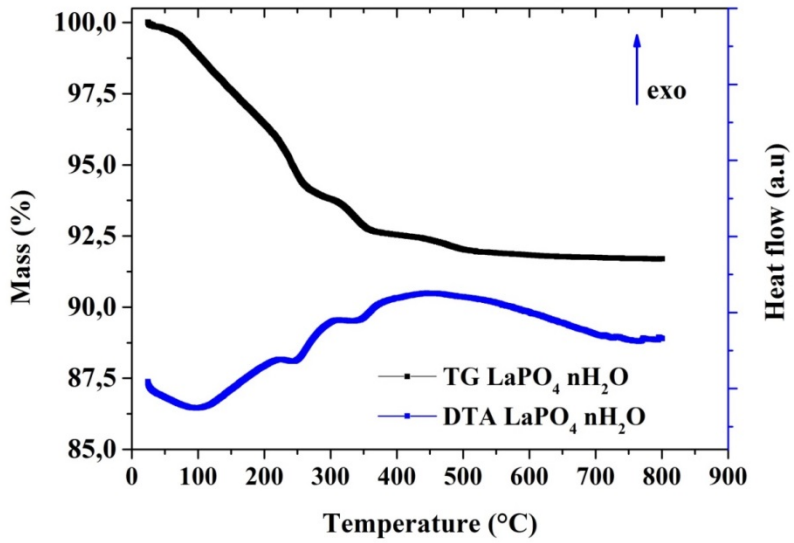


(a)

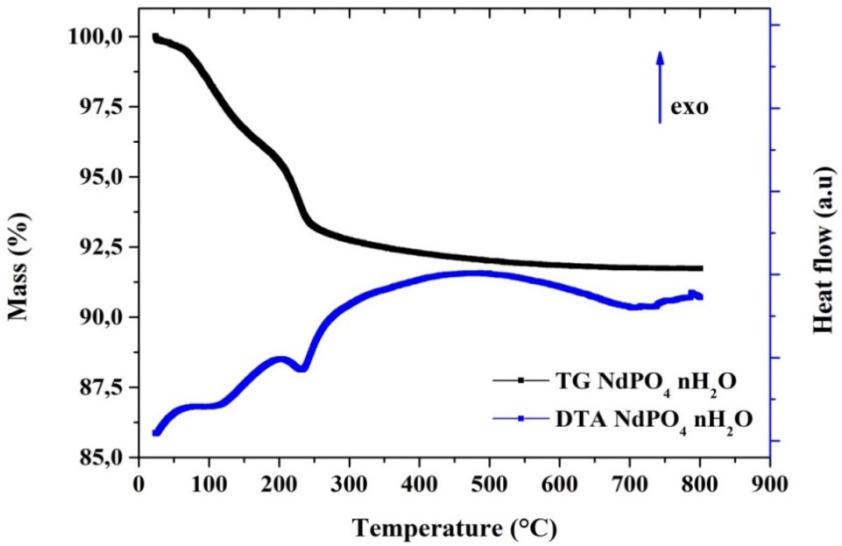


(b)

(c)

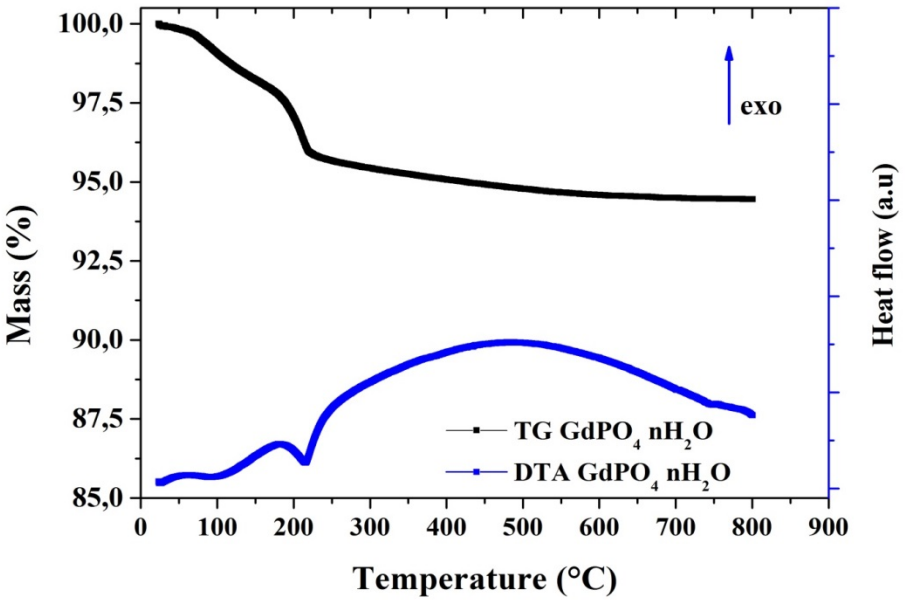


*Figure 5. 5 TGA(solid black) and DTA (solid blue) analyses for powders of (a) $LaPO_4 \cdot nH_2O$, (b) $NdPO_4 \cdot nH_2O$, and (c) $GdPO_4 \cdot nH_2O$ in ambient atmosphere and at a heating rate of 10 K/min*

*Table 5. 2 Water losses determined by TGA assuming that the weight loss can be assigned solely to loss of water.*

| Samples | BET, $m^2/g$ (this work) | As prepared phosphates | | Heat treated at 150 °C | | Heat treated at 500 °C | |
|---|---|---|---|---|---|---|---|
| | | Water losses % | Calculated water content | Water losses % | Calculated water content | Water losses % | Calculated water content |
| $LaPO_4 \cdot nH_2O$ | 78 | 8.3 | 1.2 | 4.5 | 0.6 | 1.1 | 0.1 |
| $NdPO_4 \cdot nH_2O$ | 82 | 8.2 | 1.2 | 3.3 | 0.5 | 0.9 | 0.1 |
| $GdPO_4 \cdot nH_2O$ | 25 | 5.5 | 0.8 | 3.1 | 0.5 | 1.2 | 0.2 |

The value of the hydration water, n, was estimated and found to be $LaPO_4 \cdot 0.6H_2O$, $NdPO_4 \cdot 0.5H_2O$, $GdPO_4 \cdot 0.5H_2O$. This part of water loss should be reversible to a great extent, as there is no structural transformation from rhabdophane to monazite involved. This implies that the dehydration of the rhabdophane phosphates within this temperature region can be restored if water is present in the vapor phase. Combination of the X-ray diffraction data (Figure 5. 3) with TGA/DTA results led to the conclusion that in the temperature region from 500 to 800 $^oC$, a structural transformation from the rhabdophane to monazite occurs. As proposed by Lucas et al. [133], the reaction *5.1* takes place and is followed by *5.2*:

$$MPO_4 \cdot nH_2O\ _{(hexagonal)} \leftrightarrow MPO_4\ _{(hexagonal)} + nH_2O_{(gas)} \qquad 5.1$$

$$MPO_4\ _{(hexagonal)} \rightarrow MPO_4\ _{(monoclinic)} \qquad 5.2$$

This is accompanied by the further loss associated with condensation of orthophosphates to pyro- or higher phosphates. As discussed in the crystal structures of phosphates above, the rhabdophane-to-monazite transformation resulted in the unit cell contraction and therefore irreversible dehydration.

### 5.4.2 Thermal stability under reducing and inert atmospheres

Further investigation was made by varying heating programs under different atmospheres in order to understand the behavior of water molecules in the crystal structures. The hydrolytic stability of the phosphates and their conductivities in the temperature range of 200 - 400 °C are of particular importance for applications in intermediate temperature fuel cells and other electrochemical systems. During the experiment under a reducing atmosphere (5 vol. % of hydrogen in nitrogen), the powders were heated at a rate of 2 K/min to 150 °C in order to remove the adsorbed water. The samples were then cooled to 100 °C and the TGA curves were recorded from 100 to 400 °C. The typical result for the $GdPO_4 \cdot nH_2O$ powder is presented in Fig. 6a. Only one endothermic peak is present at 170-230 $^oC$, attributable to the dehydration of the rhabdophane phase. The total weight loss is found to be 3.1 wt %, corresponding to a hydration number, n, of 0.5, in good agreement with the result estimated by Mooney [135].

During the experiment in the inert atmosphere the powders were first heated at a rate of 2 K/min up to 500 °C. The samples were then cooled to 100 °C and TGA was recorded from 100 to 800 °C, as shown in Figure 5. 6 (b). The presence of remaining water after being heated at up to 500 °C gave a further weight loss of about 1%, accompanied with a small endothermic peak. The water loss in this temperature range indicates the slow phase transition from the rhabdophane to monazite

structure. This fact is in a good agreement with the X-ray diffraction and FT-IR analyses, which showed the presence of the rhabdophane phase at temperatures of up to 650 $^{o}$C. Similar behaviors were observed for the other two phosphates, though not shown in the figure. The presence of dehydration peaks for the three $MPO_4 \cdot nH_2O$ suggests a similar dehydration process for the phosphates under varied atmospheres. The binding of water molecules in the rhabdophane structure is very strong, as expected from the zeolitic structures of the phosphates. The chemical and thermal stability of rhabdophane phosphates, or in other words, the associated water molecules, is of special interest for the proton conductivity.

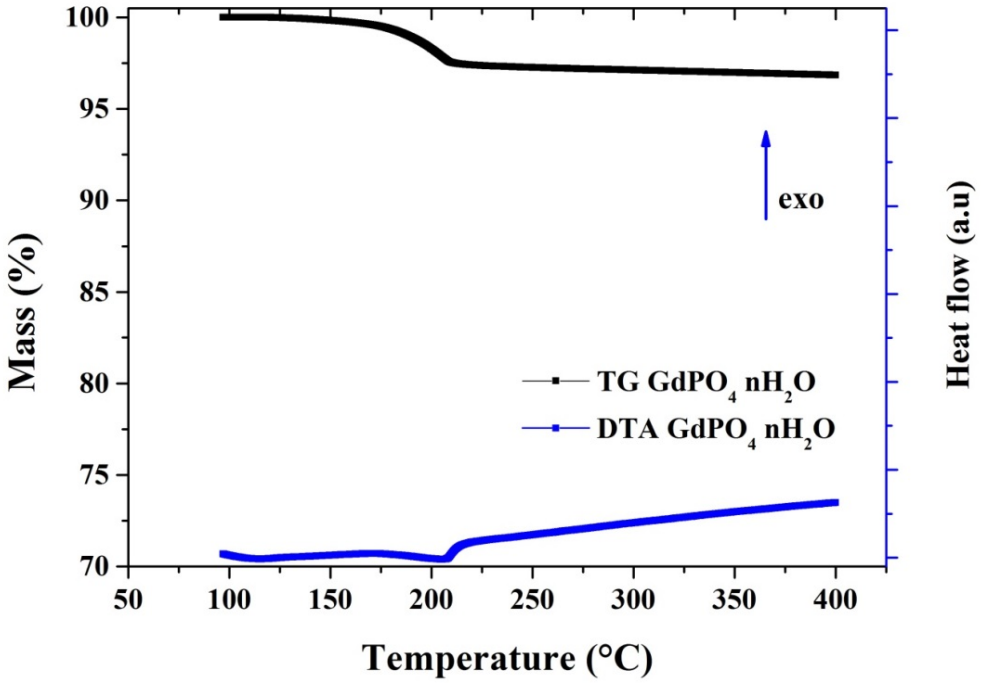


(a)

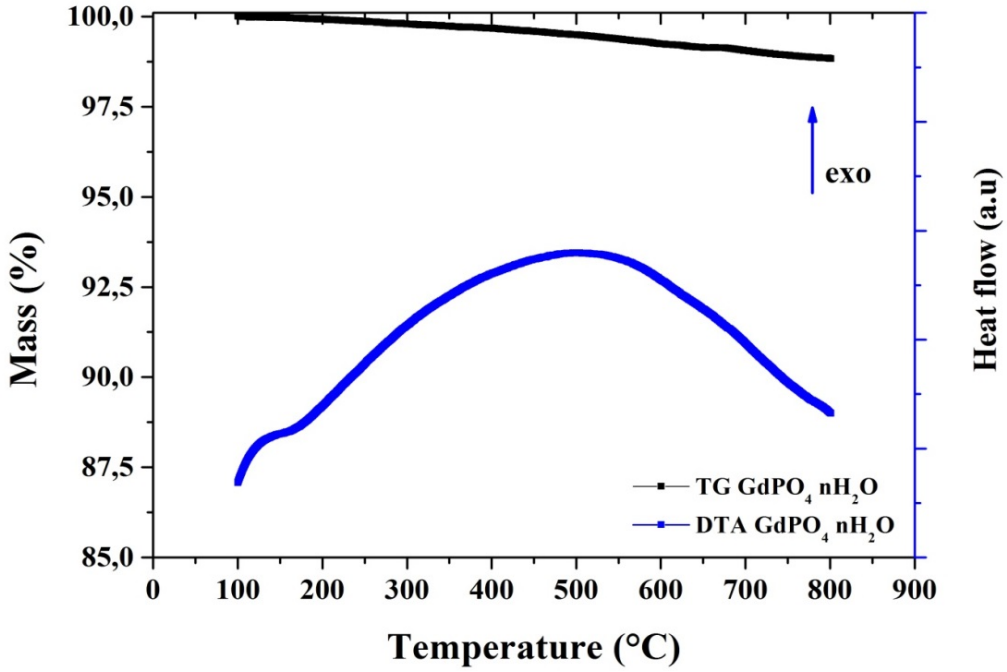


(b)

*Figure 5. 6 TGA (black line) and DTA (blue line) analyses for $GdPO_4 \cdot nH_2O$. (a) under a reducing atmosphere (5 vol% $H_2$ in $N_2$) in the temperature range of 100 to 400 $^oC$ and (b) under an inert (argon) atmosphere in the range of 100 to 800 $^oC$.*

## 5.5 Conductivity

The typical impedance plots are shown in Figure 5. 7 (a) for $NdPO_4 \cdot nH_2O$. The plots consist of two arcs: one located at high frequencies and the other, which is normally uncompleted, at low frequencies. The resistance of samples was found by fitting the first arc into semicircle with a diameter, which was taken as the bulk resistance of the sample. The conductivity of three phosphates is calculated from the resistance, and shown in Figure 5. 7 (b). Additionally shown in the figure is the theoretical calculation on the basis of the DFT calculations for lanthanum monazite by Yu et al. [146]. The measured conductivity of $LaPO_4 \cdot nH_2O$ was slightly lower but in a reasonable range close to the theoretic estimation of the proton conductivity of the monazite phosphates. The activation energy was found to be 0.61 eV for $LaPO_4 \cdot nH_2O$, close to 0.8 eV, the value predicted for monazite by Yu et al. For neodymium phosphates the conductivity is about one order of magnitude higher than that of $LaPO_4 \cdot nH_2O$ with a leveling off at temperatures above 230 °C.

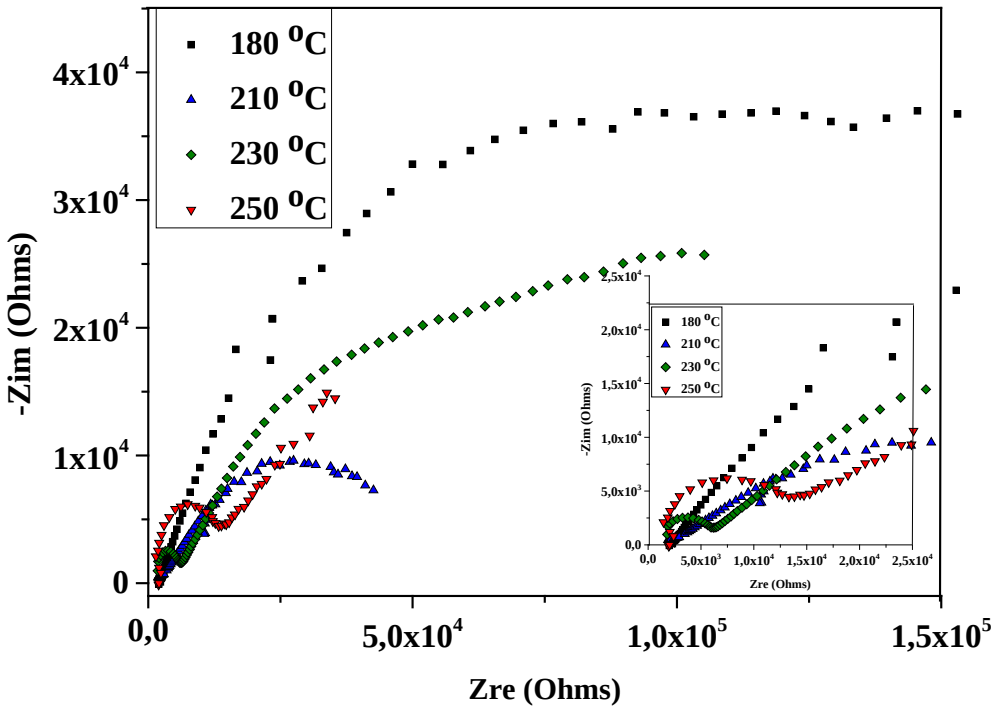
180 °C
210 °C
230 °C
250 °C
-Zim (Ohms)
Zre (Ohms)
0
1x10^4
2x10^4
3x10^4
4x10^4
0,0
5,0x10^4
1,0x10^5
1,5x10^5

(a)

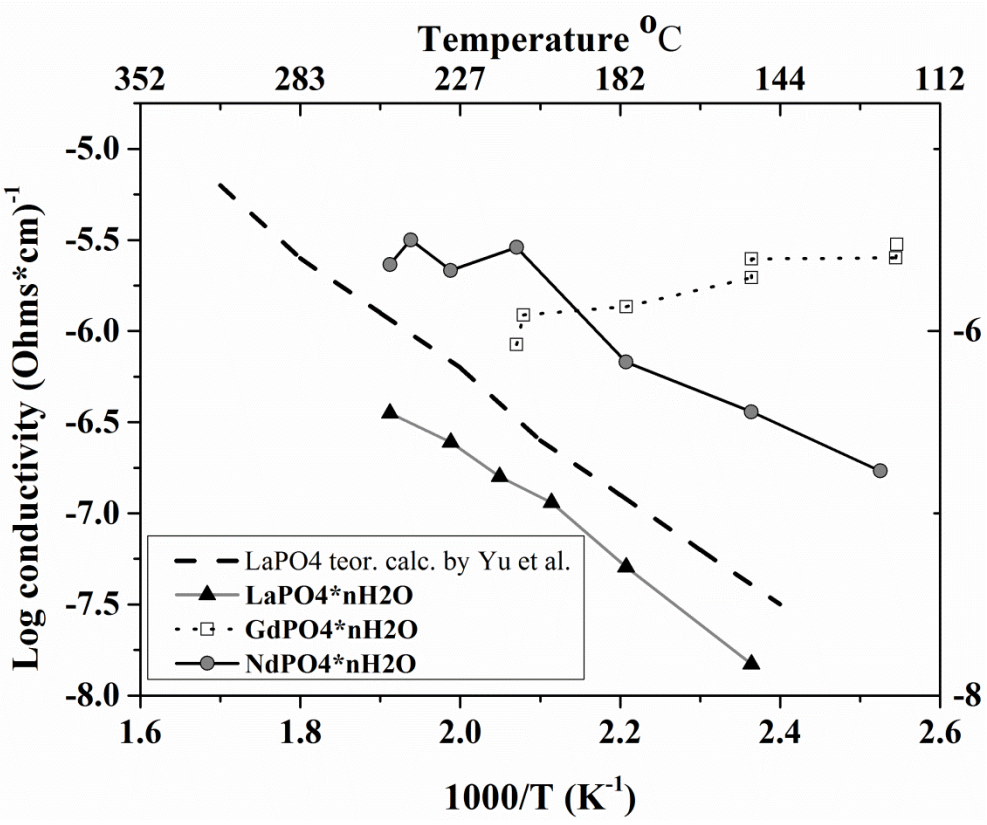
Temperature °C
352
283
227
182
144
112
Log conductivity (Ohms*cm)^-1
1000/T (K^-1)
-5.0
-5.5
-6.0
-6.5
-7.0
-7.5
-8.0
-6
-8
1.6
1.8
2.0
2.2
2.4
2.6
LaPO4 teor. calc. by Yu et al.
LaPO4*nH2O
GdPO4*nH2O
NdPO4*nH2O

(b)

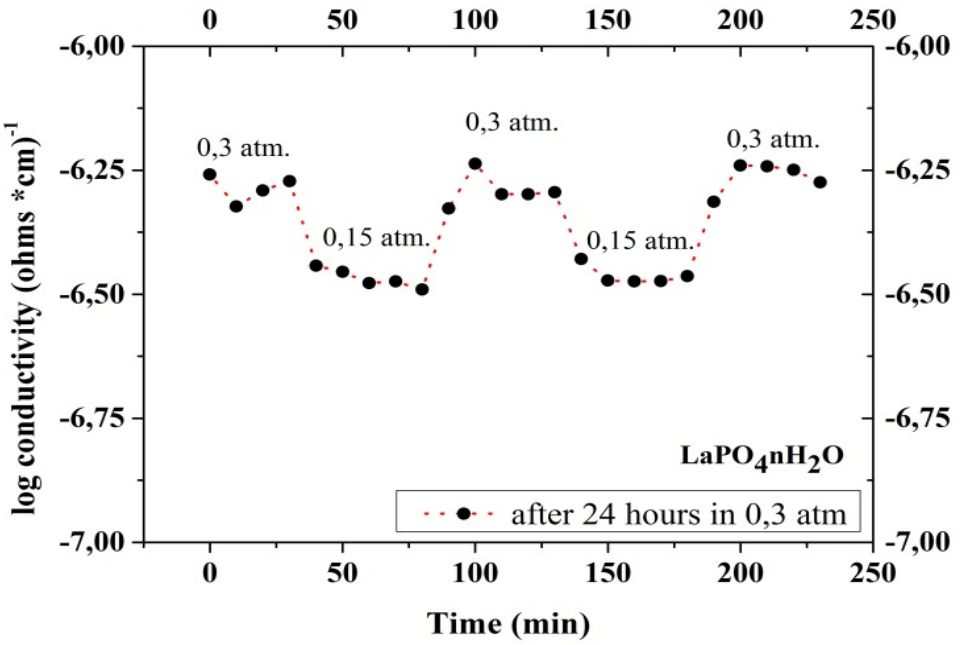


(c)

*Figure 5. 7 (a) Typical Nyquist plot for $NdPO_4 \cdot nH_2O$; (b) Conductivity of $MPO_4 \cdot nH_2O$ (where M = La, Nd and Gd) measured under a water partial pressure of $P_{H_2O}$ = 0,15 atm as compared with literature data reported by Yu et al. for $LaPO_4$ [146]; (b) Conductivity of the three phosphates; (c) Stability of the conductivity under the humidity cycling between $P_{H_2O}$=0.3 atm and $P_{H_2O}$= 0.15 atm*

The average activation energy over the entire studied temperature range from room to 250 °C was found to be about 0.41 eV. The higher conductivity and lower activation energy for $NdPO_4 \cdot nH_2O$, as compared to $LaPO_4 \cdot nH_2O$, is likely connected to the contraction of unit cells, which would shorten the interatomic distance and therefore facilitate the proton conduction. In the low temperature range, the conductivity of $GdPO_4 \cdot nH_2O$ followed the same trend, i.e. much higher conductivity than that of the other two phosphates. When the temperature was further increased, the conductivity remained unchanged or even decreased. As seen from the BET measurements, the as prepared $GdPO_4 \cdot nH_2O$ powder had a much smaller specific surface area, which in turn resulted in less water adsorption. Indeed the TGA data confirmed a lower water loss of $GdPO_4 \cdot nH_2O$, compared to its analogues (see Table 5. 2). This may partly explain the unusual temperature dependence of the conductivity.

Further investigations were made on $LaPO_4 \cdot nH_2O$ for stability evaluation of the conductivity. Figure 5. 7 (c) shows the result during an overall period of 28 hours. The sample was kept at 250 °C under $P_{H_2O}$ = 0.3 atm for 24 hours. During the period, the conductivity was slightly increased to reach a stable value of $5 \times 10^{-7}$ S/cm. This value is slightly higher than that ($3 \times 10^{-7}$) from Figure 5. 7 (b), where the water partial pressure was 0.15 atm. The water partial pressure was

then cycled from 0.3 to 0.15 atm (3 cycles within 4 hours). The conductivity was decreased to $3\times10^{-7}$ S/cm within 20 minutes and remained stable for the rest time of the first cycle. The water partial pressure was thereafter brought back to 0.3 atm, when the conductivity was completely restored in 20 minutes. The cycling was repeated with very good reproducibility. This is clearly verifying the chemical and the thermal stability of the rhabdophane phosphates and the reversibility of hydration and dehydration within the temperature and humidity range. The conductivity is however low for any practical applications of this type of materials in fuel cells or other electrochemical systems at intermediate temperatures.

## 5.6 Conclusions

Three hydrated orthophosphates were prepared from $La_2O_3$, $Nd_2O_3$ and $Gd_2O_3$ by wet precipitation in phosphoric acid aqueous solutions. Thermogravimetric analyses in air showed the following compositions of the hydrated orthophosphates: $LaPO_4\cdot0.6H_2O$, $NdPO_4\cdot0.5H_2O$, $GdPO_4\cdot0.5H_2O$. Two types of water were identified in these systems, the physically absorbed and structurally bound water. The absorbed water was of surface nature and correlated to the specific surface area of the phosphates, which could be reversibly recovered when dehydrated at temperatures below 650 °C. The hydrate water molecules were associated with the rhabdophane structure of the phosphates and stable at temperatures of up to 650 $^{o}$C. Above this temperature, dehydration took place with a structural transformation from the hexagonal rbabdophane structure to the monoclinic monazite structure. As a result of the structural contraction the dehydration is irreversible. The thermal stability of the hydrate water and therefore the structure of the phosphates were of significance for the proton conductivity. Among the studied phosphates, $LaPO_4\cdot nH_2O$ and $NdPO_4\cdot nH_2O$ exhibited the conductivity and temperature dependence in good agreement with the theoretic estimation for their monazite analogues while the prepared $GdPO_4\cdot nH_2O$ showed significant effects of the phosphate morphology.

Three examples of phosphate hydrate systems can be point out in order bring a little bit of light on complexity of proton transfer mechanisms of such families as hydrates which are $H_3OUO_2PO_4\bullet3H_2O$ (an intrinsic conductor), $Zr(HPO_4)_2\bullet nH_2O$ (a mixed surface –bulk conductor), $CeHPO_4\bullet nH_2O$ (a surface conductor) with corresponding activation energies equal 0.35 eV, 0.3-0.5 eV, 0.17-0.45 (Chapter 1). While at low temperatures main proton transfer of hydrates is ion hopping at high temperatures a quasi-liquid behavior dominates. It is possible to assume that quasi-liquid behavior can exists in such materials as rhabdophane. High conductivity values can be obtained when the strongest hydrogen bonds are broken.

# Chapter

# 6 $CsH_2PO_4/NdPO_4$ composites as proton conducting electrolyte

A challenge for the pure $CsH_2PO_4$ as electrolyte is the very narrow temperature range of the superprotonic phase from 230 to 250 $^oC$. Below this range the conductivity is insufficiently low while the chemical stability, mechanical strength and integrity, as well as the long term durability of CDP are of concern at temperatures higher than this range. To address this challenge, heterogeneous doping of the solid acid has been extensively explored as discussed in Chapter 2.

The rare earth metal phosphates have been discussed previously in Chapter 5 and their conductivity were found to be too low for an application. The water contained in such phosphates is of two types, the surface absorbed and crystal hydrate water. The absorbed water can be reversibly recovered after dehydration at elevated temperatures. The hydrate water molecules were associated with the rhabdophane structure of the phosphates and stable at temperatures of up to 650$^oC$. Only above this temperature can dehydration take place with a structural transformation from the hexagonal rbabdophane to the monoclinic monazite structure. The thermal stability of the hydrate water and therefore the structure were of significance for the acidity and proton conductivity of the phosphates. In addition, the rare earth metal phosphates are believed to improve mechanical properties of ceramic composites [147,148]. The present work is devoted to a study of the composites of CDP with the neodymium phosphate hydrate (hereafter abbreviated as NdP) for intermediate temperature proton conductor applications.

## 6.1 Composite samples

Composite materials were prepared in an agate mortar by mixing the two phosphates in changing molar ratios, as listed in Table 6. 1 according to procedures described in Chapters 3.1.1 and 3.1.2.

Table 6. 1 *Nomenclature of prepared materials.*

| Notation | Composition, mol % |
|---|---|
| NdP | $NdPO_4$•$0.5H_2O$ |
| 69NdP-31CDP | 69 $NdPO_4$•$0.5H_2O$ - 31$CsH_2PO_4$ |
| 49NdP-51CDP | 49 $NdPO_4$•$0.5H_2O$ - 51 $CsH_2PO_4$ |
| 29NdP-71CDP | 29 $NdPO_4$•$0.5H_2O$ - 71 $CsH_2PO_4$ |
| CDP | $CsH_2PO_4$ |

In order to study morphology of composite material the scanning electron microscope equipped with backscattering detector described in Chapter 3 has been used. For visualization of the morphology differences both secondary and backscattering pictures have been done for composite material 29NdP-71CDP and additionally discussed in Appendix C.

## 6.2 TGA/DTA

The TGA/DTA analyses were performed in air, as shown in Figure 6. 1 A. The TGA curve of pure $CsH_2PO_4$ showed the first weight loss at temperatures above 230 $^oC$. A plateau was observed between 270-320 $^oC$, the end of which likely corresponds to the formation of the pyrophosphate with a theoretical weight loss of 3.8%. This was followed by a sharp weight loss at above 320 $^oC$, leading to a complete conversion to polymeric $CsPO_3$ at temperatures of above 500 $^oC$ (see Figure 6. 1). The conversion of CDP to the eventual polymeric $CsPO_3$ corresponds to a total weight loss of 7.6 %, which fits well the TGA curves in Figure 6. 1 A.

The DTA curve of pure CDP, as partly shown in Figure 6. 1 B, showed three thermal events at temperatures around 234, 274 and 345 $^oC$. At around 234 $^oC$ the superprotonic phase transition and dehydration of CDP simultaneously occurred while at around 274 $^oC$ the endothermic effect was primarily attributed to the significant dehydration leading to formation of pyrophosphates. The endothermic peak at 345 $^oC$ was weakly visible, obviously associated to the melting point of the CDP. This peak is less distinct, most probably due to the varied degrees of the CDP dehydration.
The TGA plot of pure $NdPO_4$ showed roughly three steps of mass loss, corresponding to different stages of dehydration of the rhabdophane phase. Below 200 $^oC$ there was a weight loss of about 4 wt% accompanied by an endothermic peak at around 100-140 $^{\circ}C$. This was assumed to be due to the loss of the adsorbed surface water. Between 200 - 450 $^oC$ a further weight loss of ca. 3.5% of the initial sample mass was observed with a corresponding endothermic maximum at around 230 $^oC$. This was assigned to the dehydration of the hexagonal phase ($NdPO_4 \cdot nH_2O$), from which the hydration number, n, was found to be 0.5 (Chapter 5). The last event above 450 $^oC$ showed an exothermic peak at about 500 $^oC$, however, with little further weight loss and presumed to represent the transformation of the rhabdophane to the monazite structure. This phase transition was supported by the X-ray diffraction and FT-IR spectra. The total weight loss for the rhabdophane was about 8.2%, very close to that of CDP.

For the three composites studied, the surface adsorbed water of the rhabdophane seems dominating the steady TGA behavior, since the pristine compound displayed a nearly constant mass at temperatures of up to 220 $^oC$. The dehydration of the composite at around 300 $^oC$, due to the conversion of CDP to its pyrophosphate analogues, was substantially smoothed, apparently due to the presence of adsorbed as well as hydrate water from the neodymium phosphate. In case of the 29NdP-71CDP sample, the remaining mass in the temperature range from 350 to 800 $^oC$ was higher than that of either individual component, indicating a chemical interaction between the two phosphates. This was also confirmed by the DTA curves (Figure 6. 1 B), where the sharp endothermic peak of pure CDP at around 280 $^oC$ completely disappeared for all three composite

samples. As discussed above, the DTA event of CDP at around 280 $^{o}$C was attributed to the dehydration of CDP to form pyrophosphates. In other words, in the composites the dehydration of the CDP was to some extent prevented by the presence of the neodymium phosphate and its associated hydrate water.

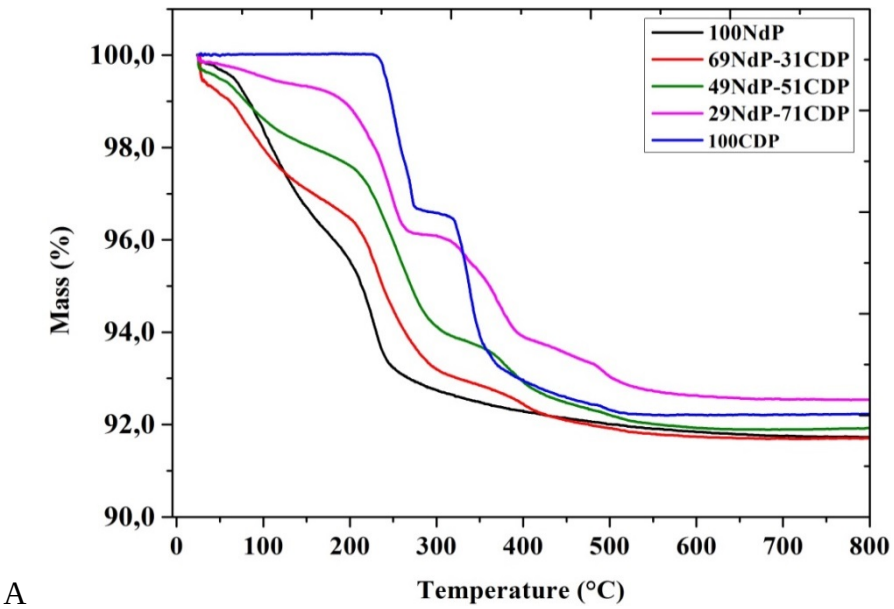


A

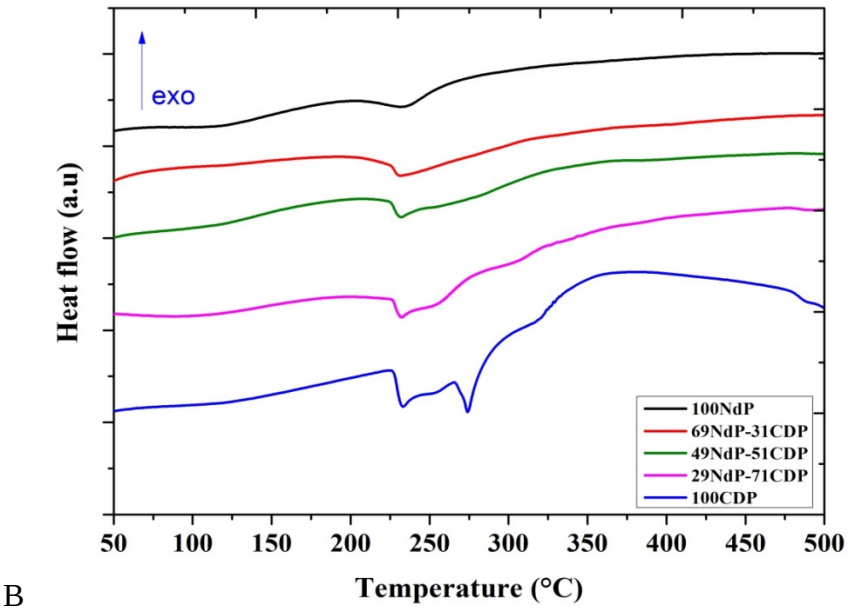


B

*Figure 6. 1 TGA (A)and DTA (B) profiles of the NdP /CDP composites and initial compounds in air (10 ˚C/min).*

## 6.3 XRD

X-ray diffraction patterns of the CDP, NdP and 29NdP-71CDP samples were recorded as shown in Figure 6. 2. Clear peaks for the monoclinic $CsH_2PO_4$ (PDF 010-83-0518) and rhabdophane (PDF 034-0535) are indexed for the two pure phosphates. The as prepared 29NdP-71CDP composite showed characteristic peaks for both components. The intensity of peaks assigned to rhabdophane was relatively week comparing to those of $CsH_2PO_4$, because of the low crystallinity of the rhabdophane phase. The composite sample was then heat treated at 250 $^oC$ for 24 hours under a water partial pressure of $P_{H_2O}$ = 0.15 atm, i.e. at conditions similar to a typical conductivity measurement of the present study. Little change was observed in the XRD patterns for the heat treated sample.

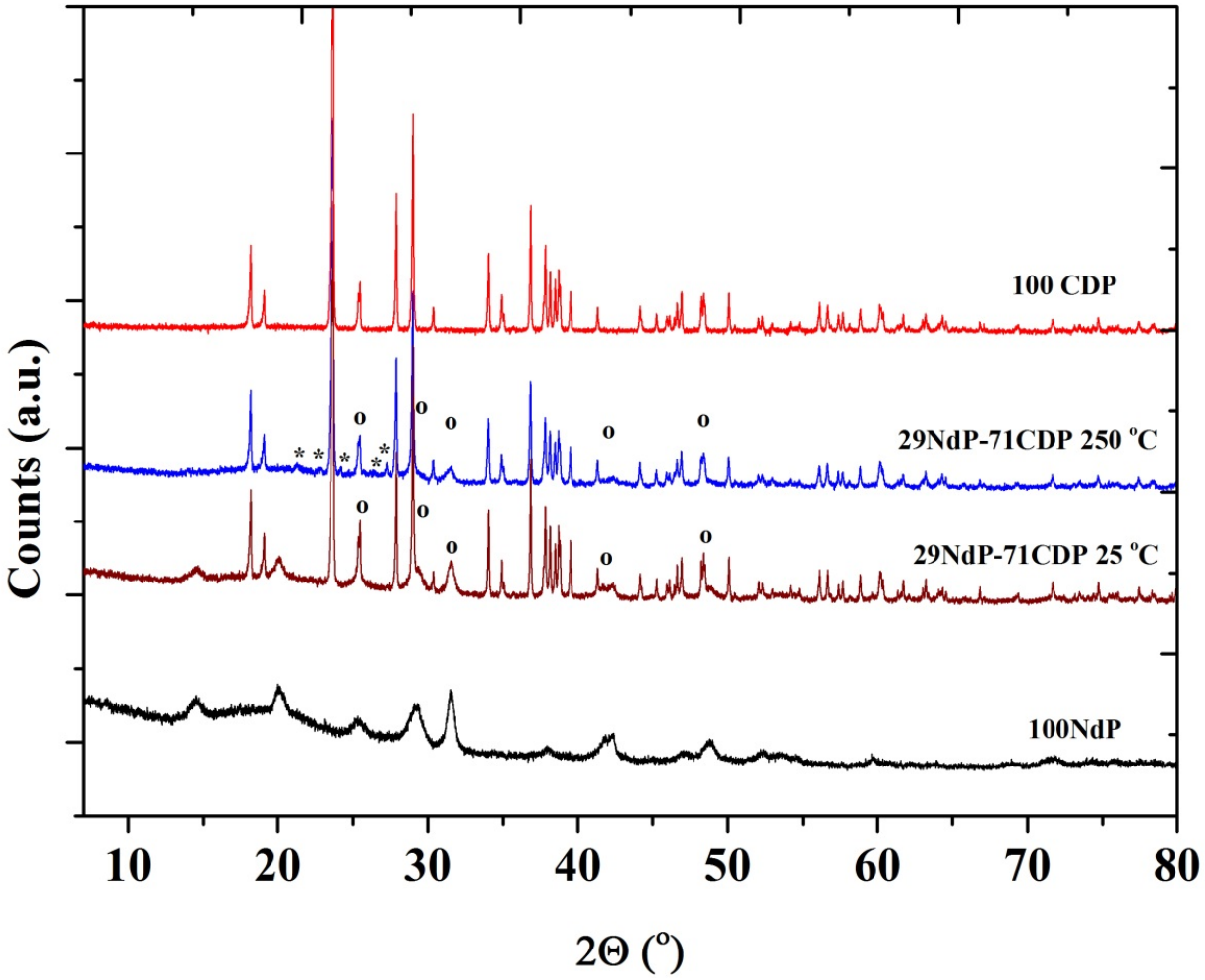


*Figure 6. 2 X-ray diffraction pattern of system 29NdP-71CDP composite and initial components before preparation, after mixing and after heat treating over 24 hours at 250 ˚C in slighlty humidified atmosphere ($pH_2O$=0,15 atm).The open circles indicate peaks for NdP and starts indicate possible peaks for $CsH_5(PO_4)_2$.*

## 6.4 Conductivity

Figure 6. 3 shows the temperature dependence of the conductivity for pure CDP, NdP and three composites in molar NdP/CDP ratios of 29/71, 49/51 and 69/31. The proton conductivity of CDP was previously reported to be $10^{-6}$ $Scm^{-1}$ at 150 °C (see Chapter 2.2.2). An increase by 3 orders of magnitudes from $10^{-5}$ to $10^{-2}$ $Scm^{-1}$ was observed at around 230 °C, corresponding to the superprotonic phase transition of CDP according to Taninouchi et al.[38]. For the pure neodymium phosphate, the conductivity was found to slightly increase from $4.23\times10^{-5}$ $Scm^{-1}$ at 120 °C to $7\times10^{-5}$ $Scm^{-1}$ at 280 °C. These values are one order of magnitude different from those previously reported (see Chapter 5). The previously reported data were collected after keeping neodymium phosphate during 18 hours at 120°C while in the present study the experiment was performed without the additional step at 120°C. The increase of conductivity is assumed to be due to an influence of additional water in neodymium phosphate.

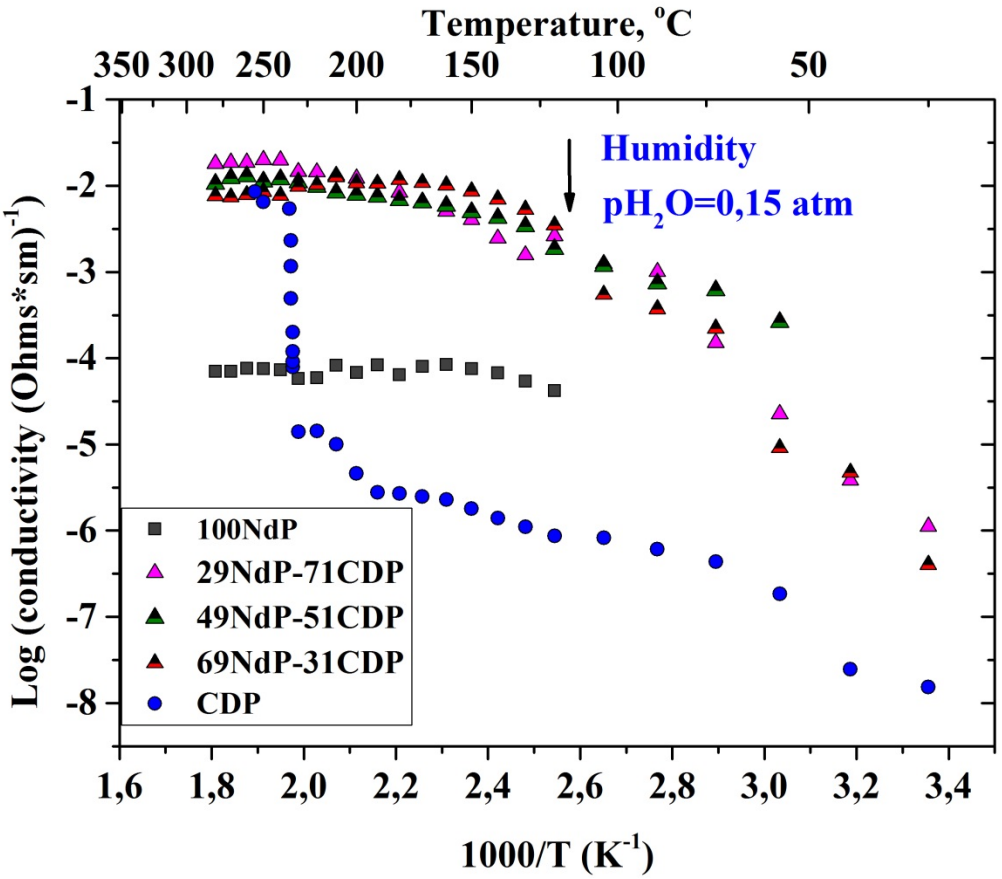


*Figure 6. 3 Conductivity of CDP, NdP and their composites as function of temperature. Humidity ($pH_2O$=0.15 atm).*

At temperatures below the superprotonic transition, the conductivity of CDP was found to be markedly higher when the neodymium phosphate phase was added. At 150°C, for example, the conductivity was $0.9\times10^{-2}$ S $cm^{-1}$ for 69NdP-31CDP, $0.5\times10^{-2}$ S $cm^{-1}$ for 49NdP-51CHP and $0.4\times10^{-2}$ S $cm^{-1}$ for 29NdP-71CDP. Across the transition temperature for CDP, the dramatic change

in the proton conductivity disappeared, indicating a new mechanism other than the superprotonic transition. For the 29NdP-71CDP sample a very small increase in the conductivity was seen while for the other two composites containing higher NdP contents, smooth conductivity curves without any trace of phase transitions were observed. Figure 6. 4 shows the conductivity changes across the entire composition range of the two pure components at four different temperatures 150, 210, 230, and 250 $^{o}$C. Moreover, the conductivity was levelled off at temperatures of up to 280 $^{o}$C.

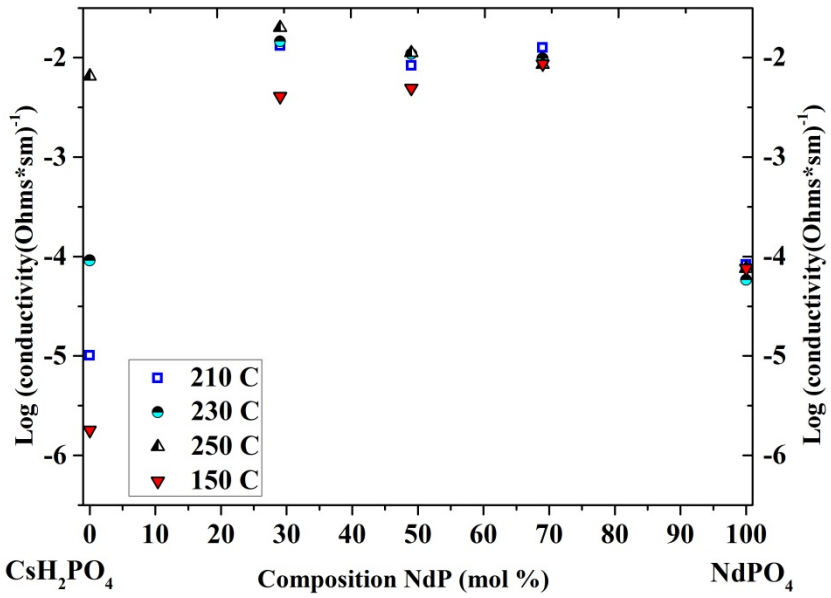


*Figure 6. 4 Conductivity of CDP, NdP and their composites as function of composition at temperatures 150, 210, 230 and 250 $^{o}$C.*

Several mechanisms have been proposed to explain the conductivity increase of CDP at temperatures below the superprotonic transition when a second phase is introduced. Highly dispersed oxides ($SiO_2$, $TiO_2$, $Al_2O_3$, $ZrO_2$) or perovskite-like zirconate ($SrZrO_3$) seem to physically stabilize the highly conductive cubic phase in a lower temperature range [56] or to induce disordering at the interface [62] (see Chapter 2.2.3). In case of CDP and $SiP_2O_7$ composites, chemical formation of a new conducting phase of $CsH_5(PO_4)_2$ was identified, which has a melting point at around 150°C. In the composite a pseudo-liquid layer of $CsH_5(PO_4)_2$ at the grain boundary was assumed to explain the improved low temperature conductivity of the composites [67,54].

Another type of proposed mechanism was related to the acid-base complex interaction via the hydrogen bonding between the two components of different acidities. When a low content of phosphotungstic acid was added to CDP, the composite sample exhibited significantly higher conductivity than that of either of the single component in the temperature range below the superprotonic transition of CDP. The acid-base interaction was further demonstrated with composites of CDP with organic base such as Guanine and its tautomers [66]. The same

phenomenon was observed for the solid sulphate salt ($CsHSO_4$) with organic molecules of basic azoles [149]. In both cases the binary composites showed significantly higher proton conductivities than that of either single component. In fact, the acid-base interaction has been known to be an effective approach to high temperature proton conducting materials, particularly in the form of acid doped polymer membranes [7] or polymeric blends [150]. A systematical investigation of the acid-base electrolyte behaviors throughout the entire composition range of measured composite was performed.[151]. It is likely that the acid-base interaction establishes a dynamic hydrogen bonding network, enabling efficient proton conduction without need for an extensive phase disordering at temperatures above the superprotonic transition.

The present study was done on neodymium phosphate in its hexagonal rhabdophane form containing 0.5 mole hydrate water (Chapter 5). The hydrate water is thermally stable at temperatures well above the superprotonic transition point of CDP. Under a humidified atmosphere, this hygroscopic salt adsorbs extra water, which was found to be associated with the specific surface area or the morphology of the phosphate and could be reversibly restored after dehydration as long as the rhabdophane structure is maintained in the relatively low temperature range. Chemically this phosphate hydrate is acidic in nature. Similar phosphates have recently been studied, e.g. niobium phosphates with significant surface acidities that can be preserved at temperatures of above 500$^oC$ and therefore exhibit proton conductivity in the intermediate temperature range [152,153]. In addition, the prepared neodymium phosphate, having a high specific surface area of about 82 $m^2/g$, may also be able to accommodate $H_3PO_4$ molecules during the solution synthesis, as evidenced by Lucas [133]. As a result the acid-base interaction between the CDP and the NdP might be a major mechanism to achieve the enhanced conductivity in the low temperature range. The dependence of the conductivity on the composite composition, as seen from Figure 6. 4, is also similar to the behavior of other acid-base composites of CDP, i.e. the conductivity of the composite is significantly higher than the conductivity of either individual component.

Moreover thermally stable water of the neodymium phosphate could also play a role, for example, to improve the conductivity as well as the stability of CDP. This seems to be confirmed by the disappearance of the DTA endothermic peak for the composite at around 275$^oC$, where otherwise dehydration of the pristine CDP would occur with significant formation of pyrophosphates.

Further investigation was made for the 29NdP-71CDP composite sample, focusing at the conductivity stability with a special heating program (see Appendix C).The sample was heated at a rate of 2$^oC min^{-1}$ from room temperature to 120$^oC$ under dry air (i.e. unhumidified air decompressed from 7 bar). A steady increase in the conductivity was observed from about $10^{-6}$ at room temperature to $10^{-2}$ $Scm^{-1}$ at 120$^oC$, as seen from Figure 6. 5.

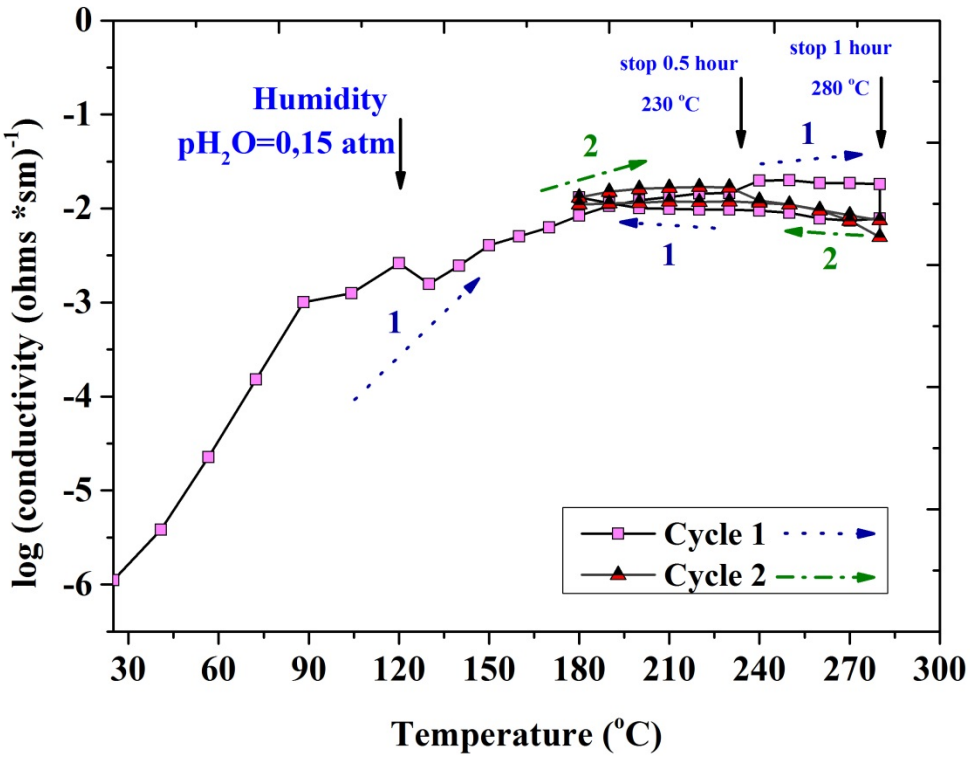


(a)

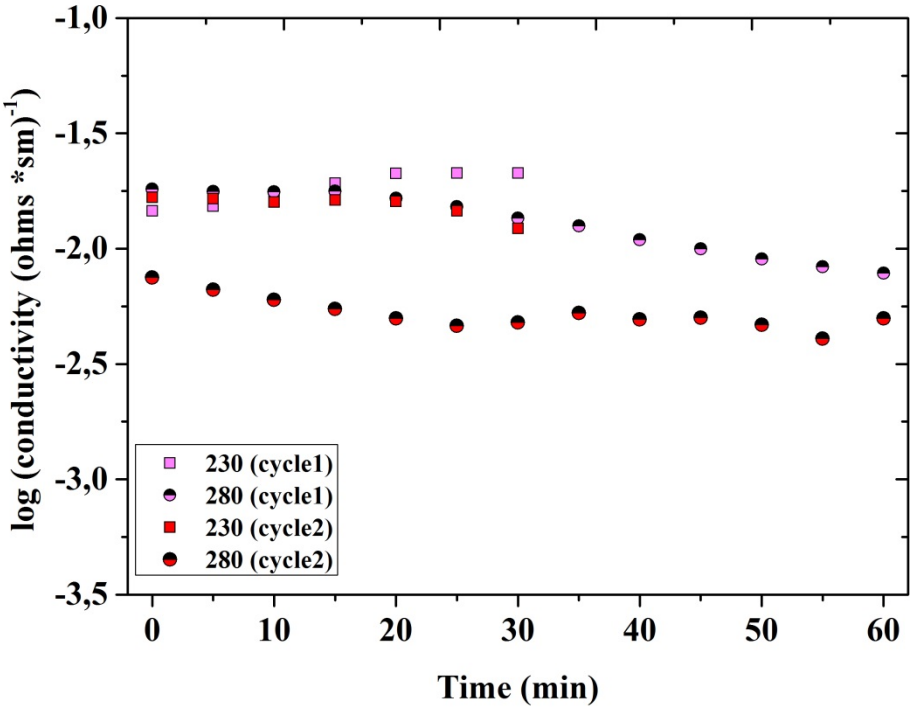


(b)

*Figure 6. 5 Stability of conductivity measured for sample 29NdP-71CDP at humidity $P_{H_2O}$=0.15 atm during 2 cycles applied heating program (additional plot in Appendix C) with 30 min and 60 min stops at temperature 230oC of superprotonic transition of $CsH_2PO_4$ and maximum temperature of 280°C.*

Further heating to high temperatures was made in a humidified atmosphere ($P_{H_2O}$ = 0.15 atm). The conductivity was continuously increased to about $10^{-2}$ $Scm^{-1}$ at 230°C. At this temperature the sample was kept for 30 minutes under the humidified atmosphere, showing a nearly constant value of the conductivity. When the sample was further heated the conductivity was steadily increasing and eventually reached $1.8\times10^{-2}$ $Scm^{-1}$ at 280 °C. At this point the sample was kept for 1 hour, during which period the conductivity was slowly decreasing to $7.8\times10^{-3}$ $Scm^{-1}$. It is interesting that when the temperature was cycled from 280 °C to 170°C, the conductivity was restored. The second cycle was made between 170 and 280 °C. The conductivity was nearly stabilized at the level of the first cycle, though it was slightly lower after the second hold at 230 °C. The conductivity variation during the stay at 230 and 280 °C of the first and second cycles was shown in Figure 6. 5. It should be noted that, the temperature region around 230 °C is where the neodymium hydrate (rhabdophane) starts hydration, which might be the major reason of the conductivity variation for the composites.

While discussing temperature region below 230 °C some good cautions should be taken to improve reproducibility this conductivity region precisely as it depends on three main factors: first one is homogeneity of composite materials (improving mixing procedure), second is acidity of initial solution of phosphoric acid from which rhabdophane powder have been prepared (affect surface acidity properties of rhabdophane) and third is amount of surface non stohiometric water in rhabdophane powder (calculated from TGA). Those three factors were found to be important for reproducing that particular region and also allowed to discuss here a surface nature of conductivity of composite material below 230 °C.

The fact that rhabdophane based composite sufficiently improved thermal properties of $CsH_2PO_4$ is clear seen from experiments performed with cycling and allowed to discuss good compatibility of this two monophosphates and make conclusion of promising properties of composite for application at intermediate temperatures.

The influence of composite material can be seen also from photos after disassembling cell after cycling conductivity measurement as shown by photos Figure 6. 6. While the sample of CDP has been destroyed, the composite material 29NdP-71CDP (measurement on Figure 6. 5) still remains stable in original shape.

Fuel cell tests have been performed in parallel project with the composite material 29NdP-71CDP (See Appendix C). Fuel cell measurements were performed at various temperatures and the fuel cell performance in terms of current density and power density increases with temperature. All I-V curves showed the Ohmic characteristics, apparently due to the thick electrolyte (700 µm) used, however the improvement of the I-V performance might be most likely due to the electrode kinetics, as the electrolyte conductivity was changing to a very limited extent. The maximum current density and power density at 285°C were found to be 117 $mAcm^{-2}$ and 27.7 $mWcm^{-2}$, respectively.

(a)  (b) 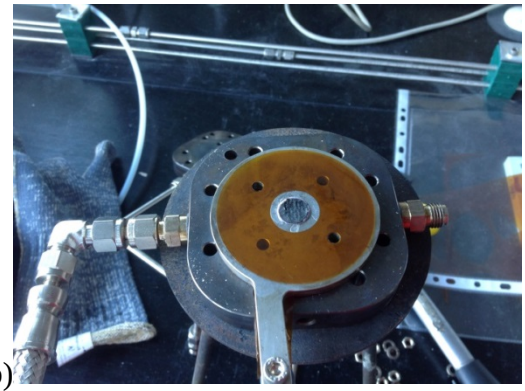

*Figure 6. 6. Photo of the samples after cycling conductivity measurement performed for (a) CDP; (b) 29NdP-71CDP composite.*

## 6.5 Conclusions

The composite phosphates based on cesium dihydrogen phosphate and neodymium phosphate hydrate were prepared with varied molar ratios. X-ray diffraction on the as prepared and heat-treated composite samples showed no evidence of new chemical compound formation. The thermogravimetric as well as differential thermal analysis revealed significant improvement in the thermal stability of cesium dihydrogen phosphates in term of dehydration as neodymium phosphate was introduced. Enhancement in the proton conductivity was observed as compared to that of pristine cesium dihydrogen phosphates in a temperature range extended to both higher and lower regimes. Particularly at temperatures below the superprotonic transition point of the cesium dihydrogen phosphate, significant conductivities were achieved for the composite. It was probable that the acid-base interaction between the two components establishes a dynamic hydrogen bonding network enabling efficient proton conduction long before the development of the extensive phase disordering of the superprotonic transition. The presence of thermally stable hydrate water contained in neodymium phosphate may also play a role in improving both conductivity and stability of the cesium dihydrogen phosphate.

# Chapter

# 7 The amorphous phase in indium doped tin pyrophosphates

Several metal pyrophosphates where M=Sn, Ti, Si, Ge, Ce and Zr [69, 154, 70, 71, 72, 73] have attracted attention due to their relatively high proton conductivities and the interest in the pyrophosphate systems especially $SnP_2O_7$ have increased after discovery of a high protonic conductivity (>$10^{-2}$ S•$cm^{-1}$) of this material in the intermediate temperature range under non-humidified conditions ($pH_2O$= 0.0075 atm.)[154, 155]. Doping with various cations such as $In^{3+}$, $Sc^{3+}$, $Al^{3+}$ have been reported as a one of several ways of enhance conductivity of pyrophosphates[70,76] and 10 mol. % of $In^{3+}$ doping considered as optimum for enhancing conductivity of $SnP_2O_7$.

Different methods to prepare the pyrophosphates have been proposed, as described in Chapter 3. They look simple however significant variations of the prepared phosphates have been reported in literature. A widely used method ís using oxides of the tetravalent atom as precursor and mixed with an excess of $H_3PO_4$ to first obtain a viscous paste, which is then heat-treated at high temperature (typically 650 $^oC$ for hours) [156,157]), followed by quenching in air up to room temperature [69, 154, 70, 72, 73]. The excess of phosphoric acid is added with the purpose to avoid phosphorus deficiency which can happen later due to calcination at higher temperatures. The $P_2O_7^{4-}$ deficiency decreases proton conductivity and changes the slope of conductivity temperature dependence in the interesting temperature range. However adding excess of phosphoric acid led questions about formation of a second phase e.g. the polyphosphorous oxides $P_mO_n$ [78]. The phosphate deficiency in $Al^{3+}$ doped $SnP_2O_7$ have been studied and reported as cause of extremely low conductivity which can be explained as disconnection of proton pathways. Depending on the amount of phosphoric acid deficiency $Al^{3+}$ doped $SnP_2O_7$ conductivity of this material can vary on two orders of magnitude [70, 76].

The excess of phosphoric acid and the possible existence of a second phase have provoked questions about their contribution or even predomination of the conductivity particularly under humidified atmosphere. This chapter is devoted to a study on this matter.

Three methods utilized in preparing the pyrophosphates were described in Chapter 3 and will be briefly outlined below.

**The oxide method.** The phosphates prepared from tin dioxide and indium oxide with excess of phosphoric acid are referred to as CA Samples. Two initial phosphorus to metal ratios were used: CA2, CA3 for P/M = 2.8 with slightly different temperature of synthesis and CA4 for P/M = 4.0. A part of the sample CA2 was further boiled in demineralized water for an hour and then filtered. The water washed sample was referred to as CA2V.

**The metal acetate method.** The phosphates prepared from metal acetates and phosphoric acid by following a procedure from Park et al. [108], with a P/M ratio of 2.0, are referred to as MA2

samples. Additionally part of the MA sample was further treated with additional amount of $H_3PO_4$ wt. 85%. The specified amount of phosphoric acid (P/M ratio 1:1) was diluted to ensure the full wetting of the powder when the MA powder was added in an alumina crucible. The crucible was then placed in furnace at 100 $^oC$ to evaporate water, and then powder was finally heated with a lid on at 650 $^oC$ for 2 hours with a ramp of 180 $^oC/h$. This sample was named as MA2-Treated.

**The metal chloride method.** The phosphates prepared from metal chlorides with ammonium hydrogen phosphate by following a procedure from Tao et al. [77], with a P/M ratio of 2.0, are referred to as Sample MC2 and MC4 and P/M ratio of 2.8 for MC3. Additionally part of the MC2 sample was further treated with an additional amount of $H_3PO_4$ with a P/M ratio of 1:1 and for the second time heated with a lid on at 650 $^oC$ for 2 hours with a ramp of 180 $^oC/h$. Thus obtained sample was named as MC2-Treated. These samples are listed in Table 7.1.

## 7.1 XRD

XRD of the materials prepared by the three methods are shown in Figure 7. 1, with comparison of relevant individual precursors. Other precursors have not been detected on XRD diffractogram. However, for CA2 and CA2V samples some additional small peaks are observed. For this small peaks there was found three possible explanations. First is one from Figure 7. 1 compares the small peaks with existing data for $SnO_2$ cubic ( ICSD 181279) and $SnO_2$ orthorhombic ( ICSD 181281) it possible to suggest existence of unreacted $SnO_2$ in the middle of larger particles mainly from difficulties in mixing of the material prepared by acid synthesis. Another possible explanation will be discussed in relation to Figure 7. 3.

All marked peaks (o) correspond to the 2θ values which have been calculated on the basis of the unit cell parameter a=7.952 Å reported by Park et al [108] for $Sn_{0.9}In_{0.1}P_2O_7$. It can be seen that in all three cases XRD data correspond to a cubic $SnP_2O_7$ phase which also shows the value for the undoped $SnP_2O_7$ reported in literature [108]. As it can be seen, only very small differences can be observed between the four cases. However, according to Park et. al [108], for the composition range $Sn_{(1-x)}In_x P_2O_7$ , $0 \leq x \leq 0.1$, there is no change in the unit cell parameter due to introduction of $In^{3+}$ in the structure, and therefore also no change in the position of the peaks. In another paper [77], a small dependency only, was reported. Thus, for the three different tin-indium pyrophosphates prepared, full success doping of the tin pyrophosphate with indium can therefore very well have been obtained.

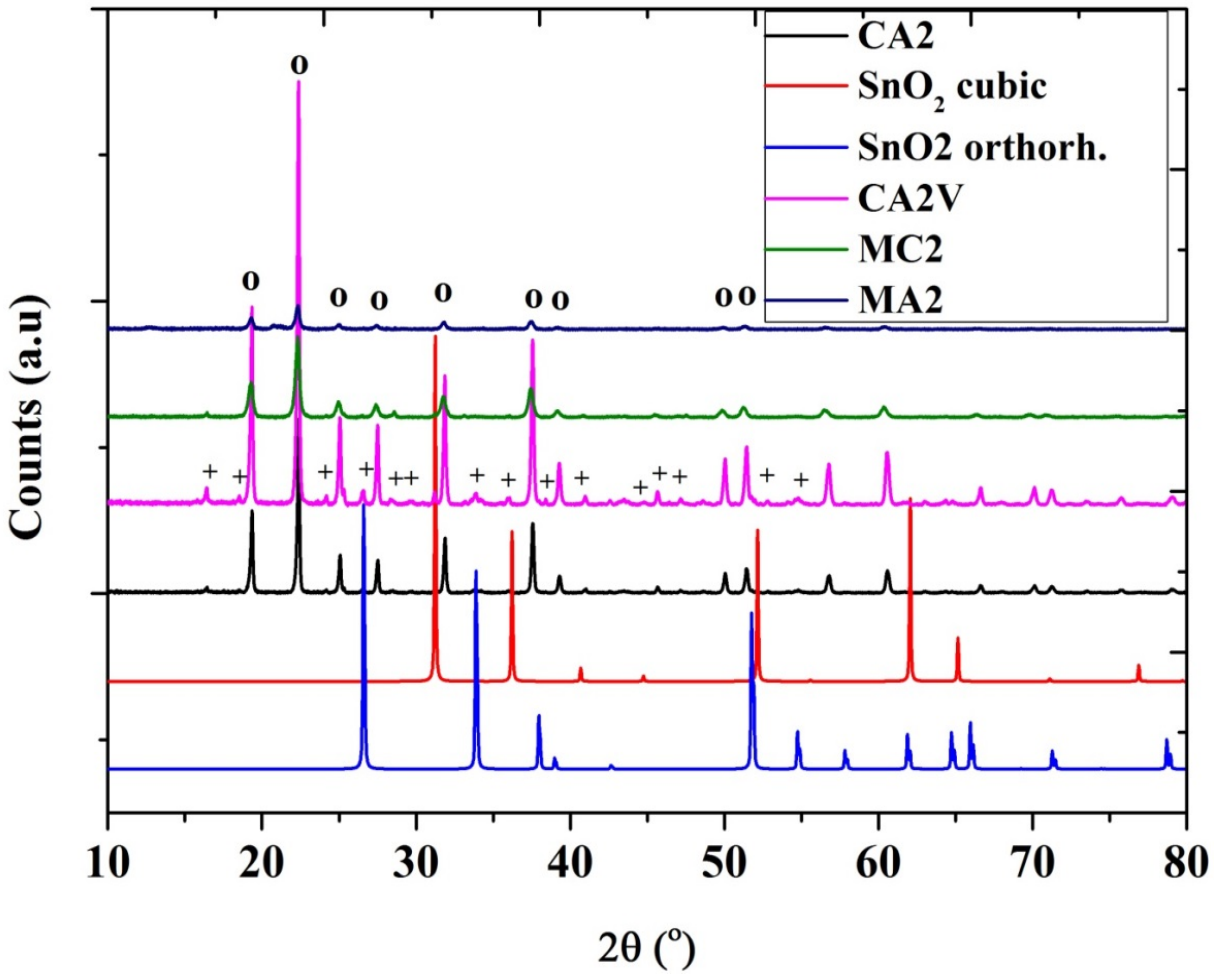


*Figure 7. 1 Typical XRD patterns of powders prepared by different synthetic methods and washed sample CA2V. For the sample of CA2V, additional lines corresponding to both cubic and orthorhombic $SnO_2$ are indicated by +. Lines corresponding to a cubic $SnP_2O_7$ are denoted as o.*

The appearance of the diffractograms indicates that CA2V has the highest crystallinity, and MA2 has the lowest crystallinity (see Figure 7. 1 and additionally Figure 7. 2). The sizes of crystallites have been calculated by Winprep software using the most intensive peak of (2:0:0) reflection and shown in Table 7. 1. The size of crystallites is 182nm, 90 nm and 31 nm for powders CA2, MC2 and MA2 respectively. It can be seen that the crystallite size is decreasing in the order CA2 > MC2 > MA2. For the CA method a nano sized powder (80 nm) was used for the synthesis, and this is probably reflected in the size of the crystallites of the resulting material, which is at the same level for the other two solution/precipitation methods.

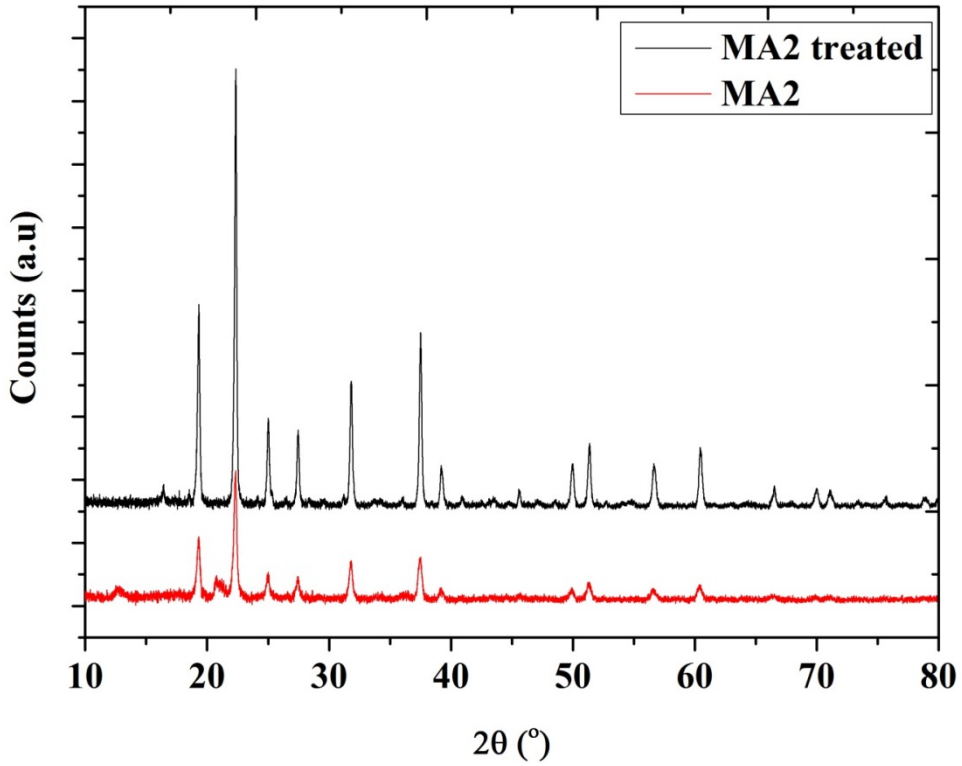


*Figure 7. 2 XRD pattern of powder prepared by the metal acetate based route MA2 as made and after treatment with phosphoric acid.*

The influence of additional treatment with phosphoric acid is shown on diffractograms of the samples prepared by the metal acetate method, MA2 and MA2 Treated, (see Figure 7. 2). The peaks are all found at the same angles of diffraction as powders prepared by the MC and CA methods but variation in intensities have been observed. As seen from the Figure 7. 2 crystallinity of the powder have been improved after treatment and a slight decrease in the peaks width can be an indication of formation larger particles which is also supported by calculation of average crystallite size, 31 nm for MA2 and 99 nm for MA2 Treated.

Part of the small peaks presented on Figure 7. 1 can be explained by presence of unreacted $SnO_2$. However smaller peaks, marked "+" in Figure 7. 3 can be explained as super lattice peaks, as reported by Tao [77]. The existence of superlattice diffraction in pyrophosphate compounds have been reported for $ZrP_2O_7$ and $TiP_2O_7$ and may be indexed as a 3×3×3 orthorombic superlattice. It should be considered however that the structure of $SnP_2O_7$ phase which was initially thought to have the simple cubic structure, later have been shown $SnP_2O_7$ phase undergo a series of reversible phase transitions on heating and cooling and to have a structure which is differs at other members of this family [68]. Thus, on the basis of the XRD data, it can be assumed that all Sn and In are present either in the main crystalline phosphate phase or in an amorphous phosphate phase and a small amount of Sn is present as impurities of $SnO_2$.

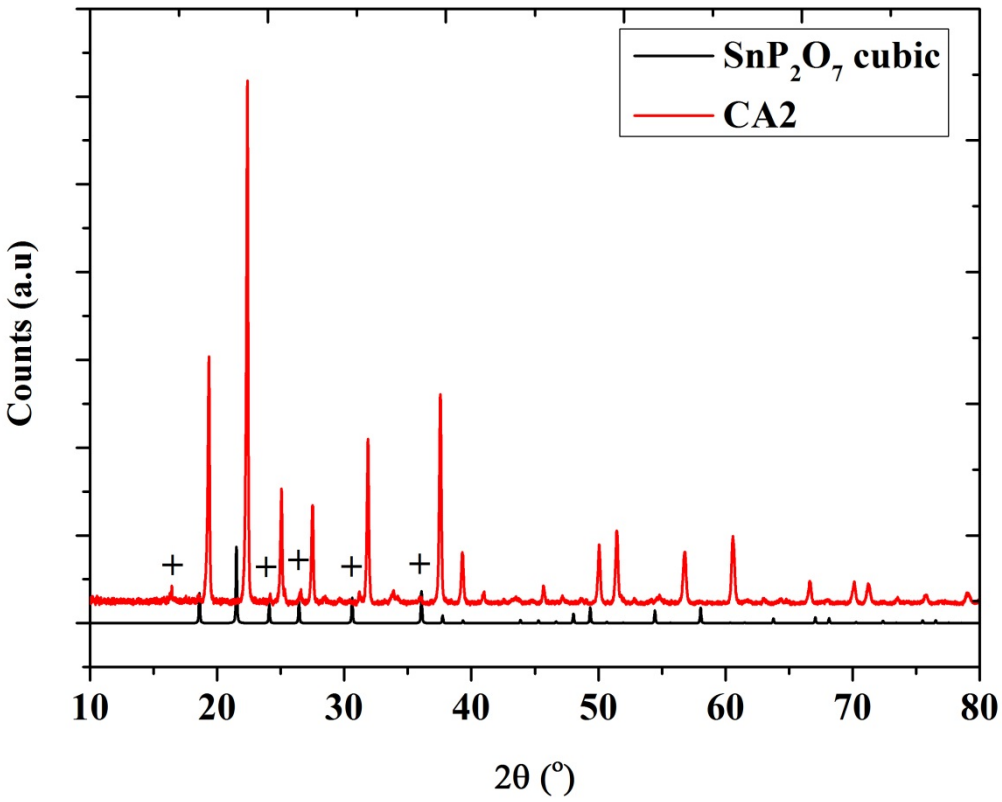


*Figure 7. 3 XRD pattern of powder prepared by acidic procedure CA2 compared with $SnP_2O_7$ (cubic) (ICSD 30583). + Denote super-lattice peaks reported by Tao [77].*

## 7.2 FT-IR

The FTIR spectra of the materials prepared by the three methods are shown in Figure 7. 4. The characteristic bands of pyrophosphates at frequencies about 744, 1015 and 1150 $cm^{-1}$ were present in all prepared powders. These bands can be assigned to the asymmetric vibration mode of $\nu_{as}(PO_3)$, the symmetric vibration mode of $\nu_s(PO_3)$ and the vibration mode of bridging (P-O-P) [78], respectively. There were several broad bands in the frequency range from 1500 and 3600 $cm^{-1}$, which were well recognized for tin pyrophosphate [154, 109] and had been attributed to the vibration of the bonded O–H groups and/or the adsorbed H–O–H groups. Nagao et al.[69] have, among others, tried to draw out a relationship between the amount of protons and the anhydrous conductivity of the $SnP_2O_7$-based conductors by comparing the absorbance intensity of peaks at 1650 and 3410 $cm^{-1}$. In the present study it is interesting that these bands associated with vibrations of bonded O–H and/or adsorbed H–O–H groups were clearly visible for the oxide-acid (CA2) samples compared with those for the acetate-acid (MA2) and chloride-ammonium hydrogen phosphate (MC2) samples. As the XRD diffractograms showed the same crystalline phase of these three samples, the observed OH-bands between 1500 and 3600 $cm^{-1}$ are proposed to be associated with the presence of an amorphous phase occurring primarily in the phosphates (CA2) prepared by the oxide-acid method.

When the CA2 sample was boiled in water, the absorptions in the 1500-3600 $cm^{-1}$ range disappeared (for CA2V in Figure 7. 4), indicating that a phase causing these bands to appear was removed. Furthermore it is also observed that the absorption in the range from 600 to 1000 $cm^{-1}$ was considerably intensified, indicating a growth of the crystallite particles during the washing.

This seems to support the above assumption of an amorphous phase either on the surface of the phosphate particles or in between the phosphate grains. This phase is soluble in hot water since it can be removed by the washing procedure. Such a phase would most likely have a high content of phosphorous. It is even likely to contain phosphoric acid, which should be in a polymerized form as the sample was calcined at 650°C. It seems clear that the absorption bands in the range from 1500 - 3600 $cm^{-1}$ are associated with an amorphous phase containing P-OH groups rather than the crystalline $Sn_{1-x}In_xP_2O_7$ phase.

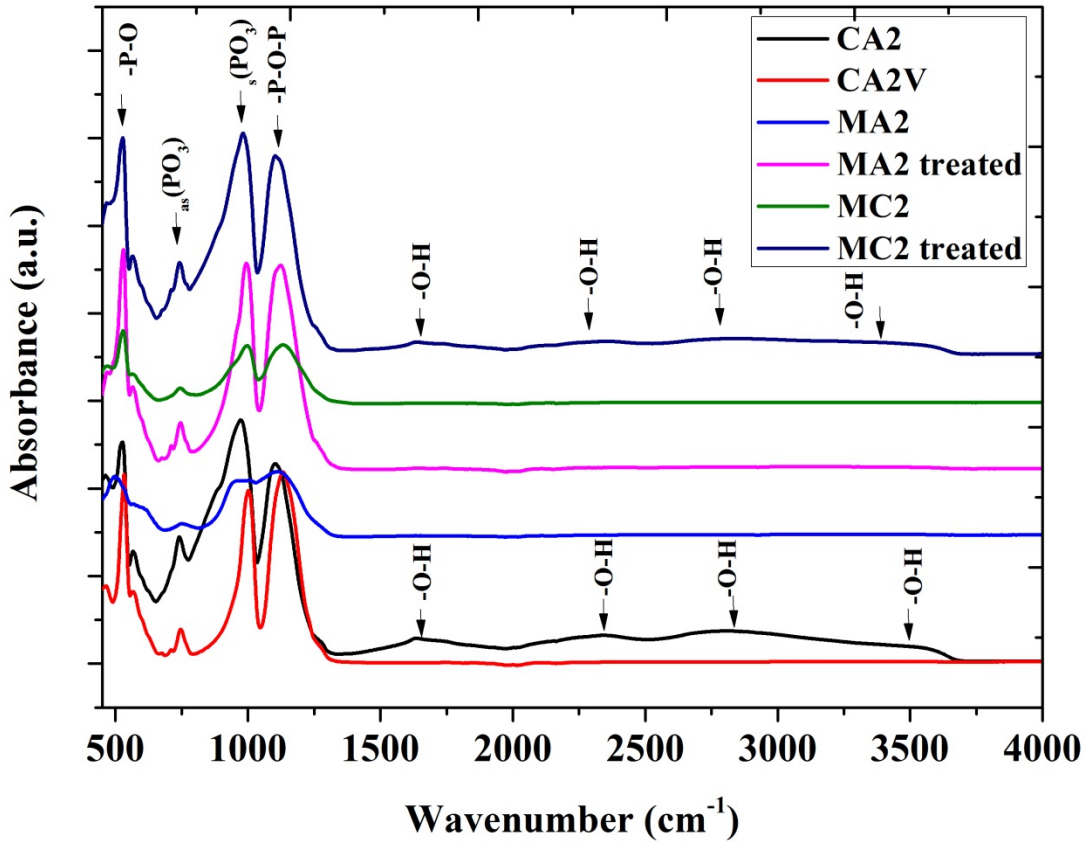


*Figure 7. 4 FTIR spectra of phosphate material prepared by different methods (a) CA and (b) MA, MC, additionally treated with phosphoric acid (MA treated, MC treated) and additionally washed after synthesis (CA2V) in the range from 400-4000 $cm^{-1}$.*

## 7.3 Morphology of particles and elemental analyses obtained by EDX

Figure 7. 5 represents six scanning electron microscopy (SEM) images of the samples (see Table 7. 1) prepared by three different syntheses (procedure described in Chapter 3) as made and additionally treated with phosphoric acid. For samples CA2, CA2V and MC2 treated it was possible to obtain images with higher magnification then for samples (MC2 and MA) mainly due to a charge effect which was a problem even on gold coated samples. The smallest particles with obviously cubic shape (see Figure 7. 5 CA2) was observed for powder prepared by acid synthesis which is somewhat of a surprise if one compares this with the estimated size of crystallites 182 nm (see Table 7. 1).

After the washing procedure (CA2V) the shape of particles is different. The overall distribution of particles for all samples except CA2 becomes less homogeneous and shapes less identified which is in good comparison with what other authors observed [77 74]. According to the reported information the particles prepared by aqueous solutions methods (for example MC) are shaped as flakes together with small balls, while particles in powders prepared by the acid synthesis are more obviously shaped as a small cubes. Such microstructure tendency can be a reason which affects the mechanism of conduction. It can be seen from Figure 7. 5 that the particles in powders prepared by other methods than CA have a strong tendency to agglomeration.

The relation of phosphorous and oxygen content measured by EDX will be discussed later with respect to NMR results. It is interesting to point out that amount of $In^{3+}$ (see Table 7. 1) in the samples prepared by acidic synthesis CA2 differs significantly (1.28 %) from amount of the same element in samples prepared by other synthetic routes such as MA2 and MC2 (4.64 and 4.88 % respectively). It is also interesting to notice that the amount of indium in the samples after the washing procedure is increased and reaches a value of 1.61 %. The individual element mapping (See Appendix) which was done on both CA2 and CA2V (washed) showed slight increase in intensities of indium and a more uniform distribution in sample CA2V. From one side it can be explained by the presence of indium both in the amorphous (in form of some soluble metal phosphate) and the crystalline phase as dopant in $SnP_2O_7$. Another explanation of the small indium content in CA2 samples can be that amorphous phase can act as protective layer and can lead to possible decrease of intensity. Unfortunately estimation of element content in order to support EDX results has not been possible to obtain from other techniques due to problems of $SnP_2O_7$ dissolution.

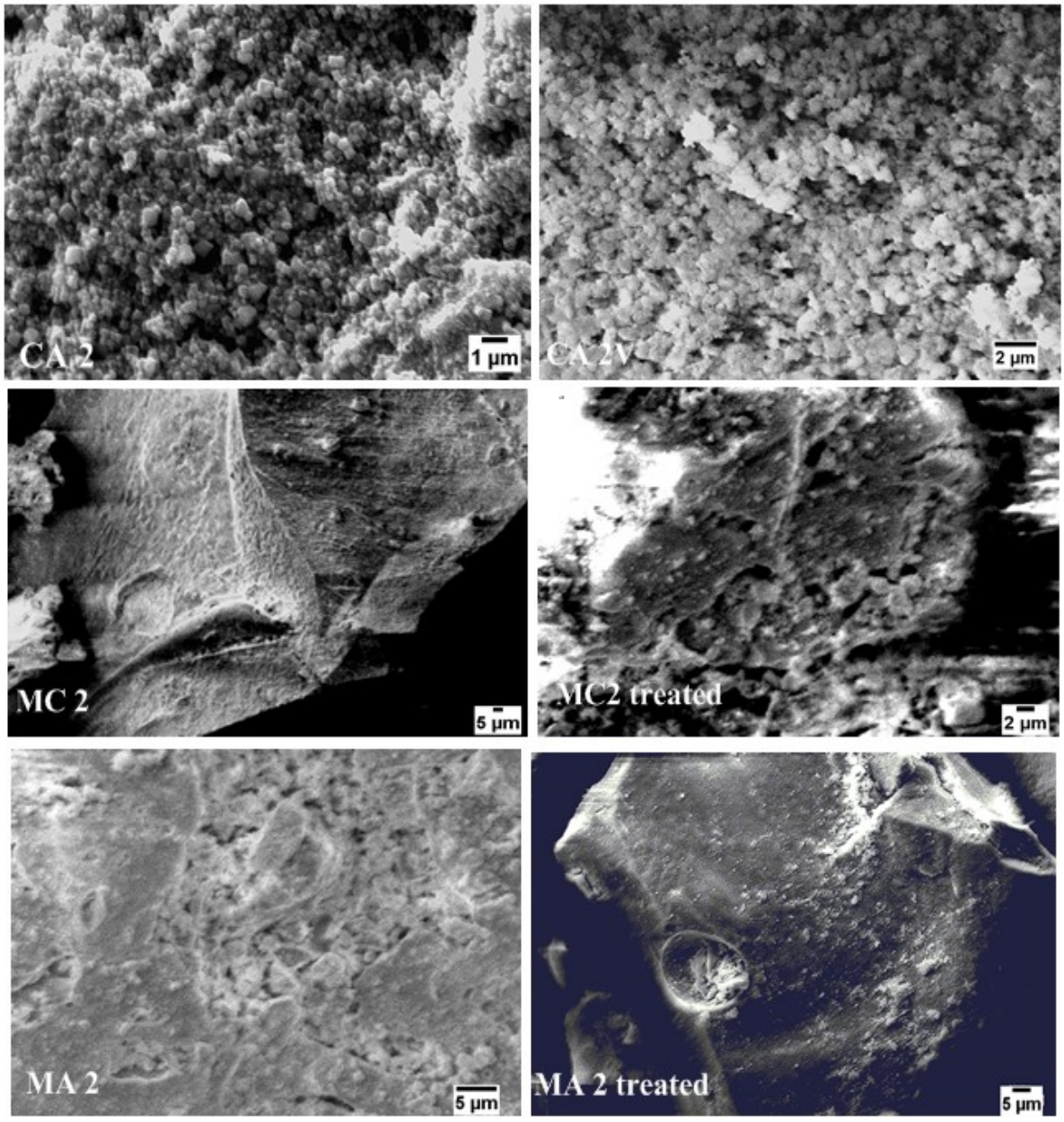


*Figure 7. 5 SEM pictures of powders prepared by acidic synthesis as made (CA2) and after washing (CA2V); by metal chloride synthesis as made(MC2) and additionally treated with phosphoric acid (MC2 Treated), by metal acetate methodic as made(MC2) and treated (MC2 Treated).*

*Table 7. 1. Element content measured by EDX of indium doped tin pyrophosphate prepared by different synthesis techniques with comparison of calculated size of crystallites from corresponding XRD pattern*

| Synthesis technic | Synthesis method | P/M ratio (additional if applied) | Sn% average | P% average | In% content | O% content | XRD Size, nm |
|---|---|---|---|---|---|---|---|
| $Sn_{0,9}In_{0,1}P_2O_7$ | Theoretical calculation | | 36.5 | 21.2 | 3.98 | 38.31 | |
| CA2 | Oxide acid | 2.8 :1 | 26.33 | 18.84 | 1,28 | 53,55 | 181.9 |
| CA2V | Acid washed after | 2.8 :1 | 31.44 | 18.3 | 1,61 | 48,82 | 190.2 |
| CA3 | Oxide acid | 2.8 :1 | 27.45 | 19.05 | 1,33 | 52,17 | 166.6 |
| CA4 | Oixde acid | 4.0:1 | 31.82 | 18.51 | 1,9 | 47,77 | 198.5 |
| MA2 | Metal Acetates and $H_3PO_4$ | 2.0:1 | 30.77 | 16.45 | 4,64 | 47,78 | 30.7 |
| MA2 treated | Metal Acetates and $H_3PO_4$ | 2.0:1 (1.0:1) | 28.93 | 18.72 | 4,66 | 47,69 | 98.5 |
| MC2 | Metal chlorides $(NH_4)_2HPO_4$ | 2.0:1 | 25.30 | 18.3 | 4,88 | 51,52 | 90.3 |
| MC2 treated | Metal chlorides $(NH_4)_2HPO_4$ | 2.0:1 (1.0:1) | 29.84 | 18.86 | 4,21 | 46,76 | 96.6 |
| MC3 | Metal chlorides $(NH_4)_2HPO_4$ | 2.8:1 | 29.18 | 18.51 | 3,44 | 48,87 | 57.8 |
| MC4 | Metal chlorides $(NH_4)_2HPO_4$ | 2.0:1 | 28.78 | 18.93 | 4,44 | 47,85 | 33.2 |

## 7.4 $^{31}$P-NMR spectroscopy and phosphorous content

According to calculation based on NMR results (see Appendix D) for sample prepared by acid synthesis (CA2) with ratio of $H_3PO_4$:$Sn_{0.9}In_{0.1}P_2O_7$ corresponds to 1:2.93 respectively it is possible by making a simple calculation ($M(Sn_{0.9}In_{0.1}P_2O_7)$=292.3 g/mol) to estimate the amount of P in $H_3PO_4$ which is 7.9 % and in $Sn_{0.9}In_{0.1}P_2O_7$ it is 15.9 %. Total amount of phosphorous calculated by using chemical formula is 23.8 %. The average value measured by EDX is at least 5 % lower than one calculated from NMR results. However the maximum measured by EDX for samples prepared by acid synthesis gives a value close to the one calculated from NMR results (see Figure 7. 6 for CA2, CA3, CA4). Of course it must be considered that this calculation is a rather rough value but still gives a clue about the phosphorous deficiency in the sample. Following the same logic the amount of oxygen in the sample O in $H_3PO_4$ is 16 % and in $Sn_{0.9}In_{0.1}P_2O_7$ 28.7 %. Total calculated amount is 44.7 % which is significantly less than the average ratio measured by

EDX (See Table 7. 1). If one compares samples such as CA4 and treated MA and MC methods it can be noticed that there is significant difference between average and maximum and minimum values of phosphorous content. This can be possibly attributed to an uneven distribution of amorphous phase in samples prepared by this method.

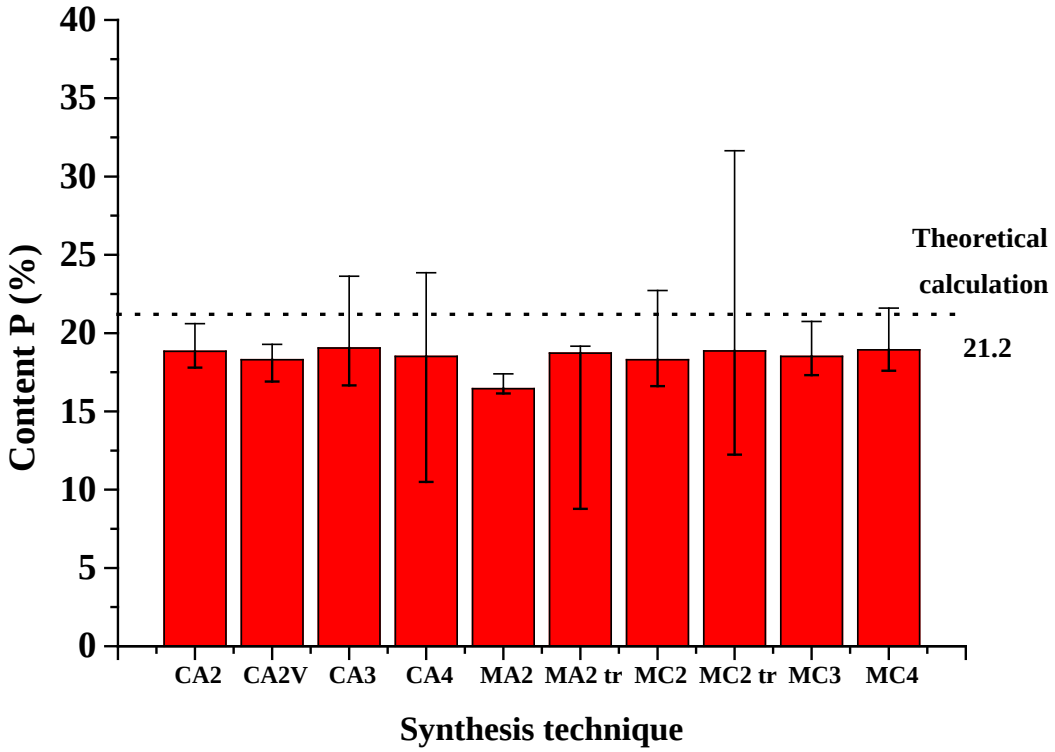


*Figure 7. 6. Phosphorous content measured by EDX for samples prepared by three different ways: the oxide method (CA), the metal acetate method (MA)[108] or the metal chloride method (MC) [77] (according to the Table 7.1) both doped and as made with line corresponding to theoretical value calculated from chemical formula of $Sn_{0.9}In_{0.1}P_2O_7$.*

## 7.5 Conductivity measurements of $Sn_{1-x}In_x(P_2O_7)_{1-\delta}$

Figure 7. 7 shows the conductivity of $Sn_{1-x}In_x(P_2O_7)_{1-\delta}$ prepared by methods (CA2,MC) as well as sample CA2 after washing procedure(CA2V) and samples prepared by MC and MA methods specially treated with phosphoric acid (MC treated, MA treated) in the range of temperatures 120-300 $^oC$ measured at specified humidity conditions ($pH_2O$=0.15 atm). For comparison listed conductivity values for the same type of material prepared by other authors such as Nagao et al [69] (CA type synthesis) and Tao et al [77 109] (MC and CA synthesis) are also included. The highest values of conductivities were always obtained by the classic acid method.

Another interesting feature is that the conductivity of the sample prepared by the acid method after the washing procedure (CA2V) had the lowest value of conductivity from all samples around $10^{-7}$ S/cm. The conductivity values for the sample prepared by MA2 were at the same range as the one prepared by CA2V. In Figure 7. 7 it can be seen that the materials of high crystallinity and very little amorphous phase according to NMR spectra (Appendix D), i.e. the material prepared by MC and MA materials prepared by procedures reported by Park or Tao [77 108], all have shown very low conductivities which is in a good agreement with literature data reported by Tao for the same type of my methods in [77 109]. However it appears that for the MC material the conductivity can be raised to significant values, by treating with phosphoric acid (MC treated). For the materials prepared by the acetate method, the EDX analysis shows that the $H_3PO_4$ added afterwards is rather unevenly distributed (large difference between lowest and highest measured contents of phosphorous, Figure 7. 6 Table 2), and that can be an explanation why the conductivity was not improved by phosphoric acid treatment: A continuous network of particles having a conductive surface was not established. This particular material had very small crystallites (31 nm) (Table 7.1), which might prevent the phosphoric acid to enter the particles to a higher degree than in the case of the chloride method. However another issue could be that the crystals of the cubic tin pyrophosphate have different surface properties depending on the preparation method.

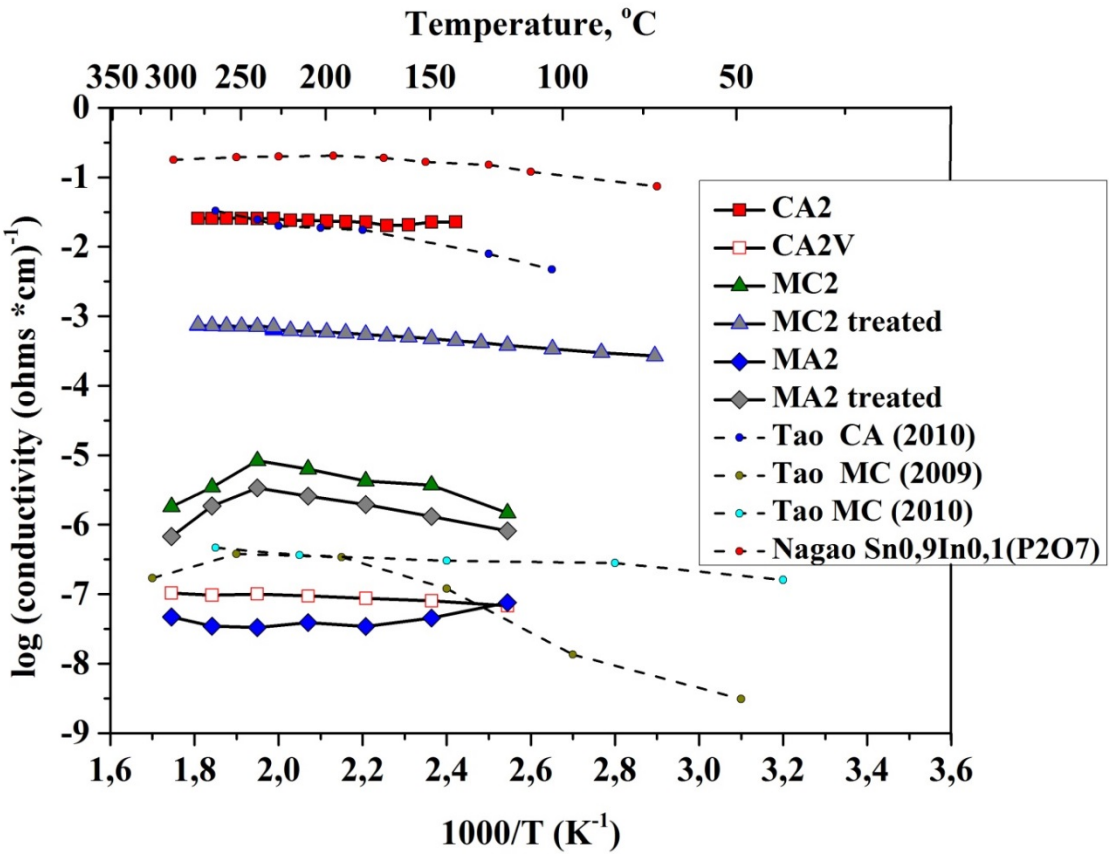


*Figure 7. 7 Temperature dependence of conductivity for $Sn_{1-x}In_x(P_2O_7)_{1-\delta}$ measured under humidified conditions ($P_{H_2O}$=0,15 atm.) compared with literature data obtained by Nagao for $Sn_{0,9}In_{0,1}P_2O_7$ [69]; Tao CA (2010) gives conductivity values for a sample of $SnP_2O_7$ prepared from*

*$SnO_2$•n$H_2O$ and $H_3PO_4$ (2.8:1) according to Tao et al. [109]; Tao MC (2009) corresponds to conductivity values taken for sample of $Sn_{0,92}In_{0,08}(P_2O_7)_{1-\delta}$ prepared by metal-chloride method according to Tao result [77]; Tao MC (2010) corresponds to conductivity values taken for sample of $SnP_2O_7$ prepared from $SnCl_4$•5$H_2O$, $(NH_4)_2PO_4$ according to Tao et al. [109] respectively.*

For chloride method (MC) (see Figure 7. 7), the conductivity values have been improved after phosphoric treatment, $10^{-3}$ $Scm^{-1}$, but never reached the same high values as for samples prepared by CA methods. For the acetate method, it is on the other hand observed that even though there is a relative improvement of conductivity by phosphoric acid treatment, the absolute value is still very low indeed, $10^{-5}$ $Scm^{-1}$. This corresponds to the NMR results, which showed very little amorphous phase, even after a treatment with phosphoric acid. These observations of course strongly support that the conductivity of the materials are related to the presence of an amorphous phase.

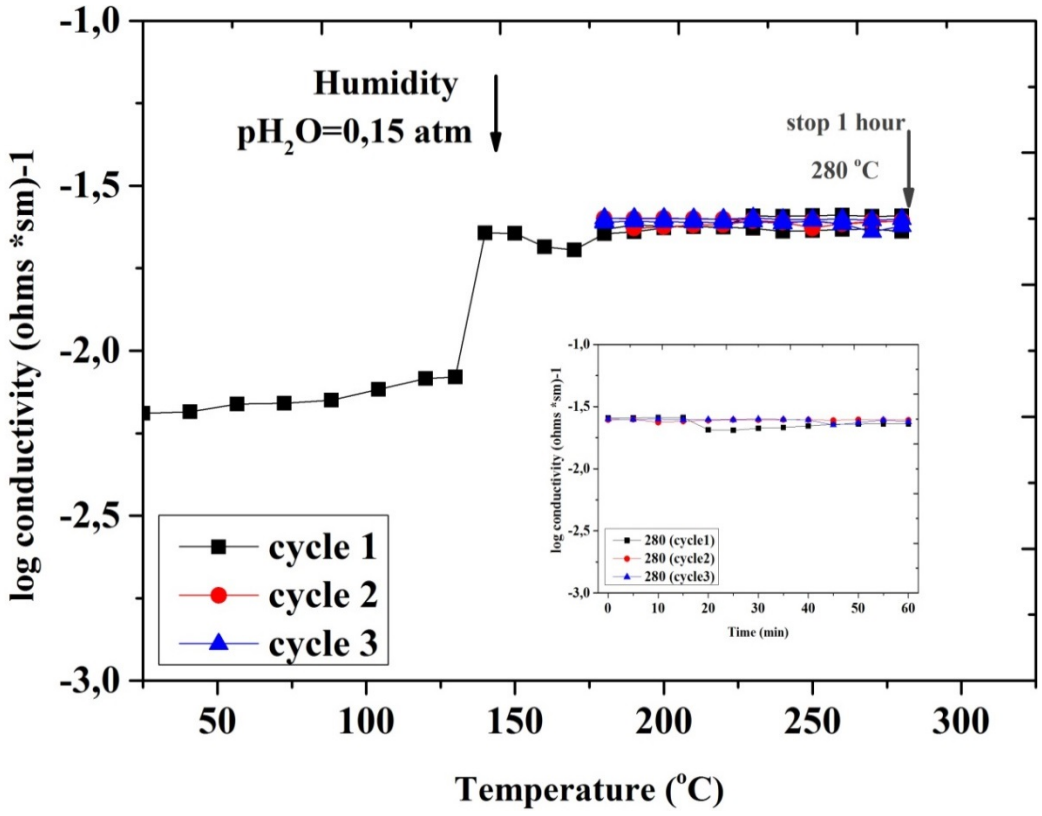


*Figure 7. 8 Stability of conductivity for CA2 sample during three cycles of heating and cooling between 180-280 °C with one hour stop at maximum temperature 280 °C (humidity conditions $P_{H2O}$=0,15 atm.). The insert figure represent values of the conductivity function of time at 280 °C.*

In Figure 7. 8 the cycling (both cooling and heating was done with a temperature program between 160-280 °C with a stop at the maximum temperature of 1 hour) is shown the sample with most promising conductivity values (0.02 $Scm^{-1}$ at 280 °C CA2). Figure 7. 8 summarizes results obtained from three cycles. Slight increase in conductivity (from 0.008 to 0.02 $Scm^{-1}$) is observed

after humidity ($P_{H2O}$=0.15 atm) was introduced into the cell. During the three cycles theconductivity of the CA2 material remained stable and unchanged. The insert figure of conductivity versus time at maximum temperature 280 $^{o}$C did not show changes in the conductivity as well. These results denote stability of material at temperatures up to 280 $^{o}$C even at cycling conditions.

## 7.6 Conclusions

Indium doped tin pyrophosphate have been prepared by three different synthetic routes. It was found that three synthetic routes led to significant differences in conductivity values and properties of indium doped tin pyrophosphate.

The synthesis from oxide precursors with excess of phosphoric acid gave phosphates with the highest conductivity above 0.02 $Scm^{-1}$. A phosphorus rich amorphous phase is simultaneously formed, surrounding or along the grain boundaries of the crystalline particles. The amorphous phase prevents the agglomeration of the particles. The amorphous phase seems to hydrolyze in the presence of water or moisture, evidenced by the OH-bands of FTIR and NMR. Washing in boiling water can remove the amorphous phase causing particle agglomeration and a dramatic decrease in the conductivity.

A phase of $Sn_{0,9}In_{0,1}P_2O_7$ material has been obtained by the acetate and chloride methods. The measured conductivity of these samples was found to be low, similar to that of the washed phosphate samples mentioned above. The additional treatment of low conductivity samples with phosphoric acid showed an increase in conductivity of the acetate samples though never reached the values reported for samples from the oxide synthesis. For the chloride samples, however, little improvement in the conductivity was observed after the acid treatment, probably due to the difficulties of introducing an amorphous phosphorus containing phase onto the agglomerated particles.

The EDX studies revealed that indium doping in samples prepared by the oxide route was less than the expected loading as compared to the other methods, likely indicating a fact that the $In^{3+}$ can present in both amorphous and crystallite forms.

# 7 The amorphous phase in indium doped tin pyrophosphates

# Chapter

# 8 Cerium ultraphosphate $CeP_5O_{14}$

The discovery of high-temperature proton conduction in $SrCeO_3$- based perovskite type oxides by Iwahara [158] stimulated research for further development of cerium based oxides. The detailed study of these cerate perovskites revealed that the chemical stability in atmospheres containing carbon dioxide and water vapor is an issue [159]. On the contrary, rare earth phosphates are expected to have higher chemical stability for fuel cell applications.

Kitamura et al. reported mixed proton and electron hole conduction for cerium orthophosphate $CePO_4$ [94] under reducing atmospheres. The proton conductivity for other cerium based phosphates such as Sr doped $CePO_4$ [160,130], $Ce(HPO_4)_2 \bullet nH_2O$ [21,22] and $CeP_2O_7$ [161,162] has been reported at various temperatures depending on the type of their structures. To date the most widely studied cerium phosphates remain the orthophosphate $CePO_4$ and its doped analogues. The reported conductivity of Sr-doped $CePO_4$ was from $1.7\times10^{-3}$ to $3.82\times10^{-3}$ S/cm at temperatures from 750 to 950°C. The focus on intermediate temperature applications is opening possibilities of high proton conductivity for other phosphate systems.

Recently Unemoto et al.[130] studied strontium doped lanthanum ultraphosphate ($La_{1-x}Sr_xP_5O_{14-\delta}$ ($x = 0$, 0.01, 0.03 and 0.05) under atmosphere with varied oxygen and water vapor partial pressures in the temperature range of 250-400 °C. Proton conductivities, as evidenced by isotope effects of hydrogen and deuterium, were found to be in a range of $4.7\times10^{-5} - 2.2\times10^{-3}$ $Scm^{-1}$. It seems that the strontium doped lanthanum ultraphosphates are purely proton conductors even in unhumidified environment. The proton conductivity and the activation energies are similar to those of other rare earth phosphate based protonic conductors.

Within the present project, preliminary efforts were made to investigate cerium ultraphosphates and the following is a brief accountof the work.

## 8.1 XRD and structural modeling

In the $Ce_2O_3$-$P_2O_5$-$H_2O$ system particularly in the area with the atomic ratio $P_2O_5/Ce_2O_3>1$, several compounds are proposed to exist including $CePO_4$, $CePO_4.nH_2O$[135], $CeP_2O_7$, $Ce(PO_3)_3$, $Ce(PO_3)_4$ and $CeP_5O_{14}$ [163,36]. Chemical methods for preparation of these phosphates have been reported. Attempts were also made to form a whole picture of crystallization of cerium phosphate compounds. A diagram of crystallization of cerium phosphates can be found in the work of Tsuhako et al. [163] (see Appendix E).

For rare earth metal ultraphosphates in general, three different crystal structures are recognized to exist: the monoclinic form I with the space group $P2_1/a$ (for rare earth metals from La to Tb), the monoclinic form II with the space group $C2/c$ (for rare earth metals from Dy to Lu, Ce,

Y) [164] and the orthorhombic form with the space group *Pnma* (for elements from Ce, Dy to Er, Y). In addition, a new type of triclinic crystal structures with the space group *P1* was found for the cerium ultraphosphate.[165]

Some of ultraphosphate compounds are isotypic while others have clear polymorphic properties [110]. Unfortunately many polymorphs have not been recognized to date due to lack of research in the ultraphosphate chemistry. The cerium ultraphosphate ($CeP_5O_{14}$), on the other hand, is found to exist in all four structural forms and the orthorhombic form is the most stable and can be obtained by crystallization under certain conditions.

XRD patterns of the synthesized cerium ultraphosphate powders are shown in Figure 8. 1. Clear peaks for the orthorhombic phase of $CeP_5O_{14}$ (PDF 260053) are indexed for the powders. The two small peaks denoted by star were not recognized.

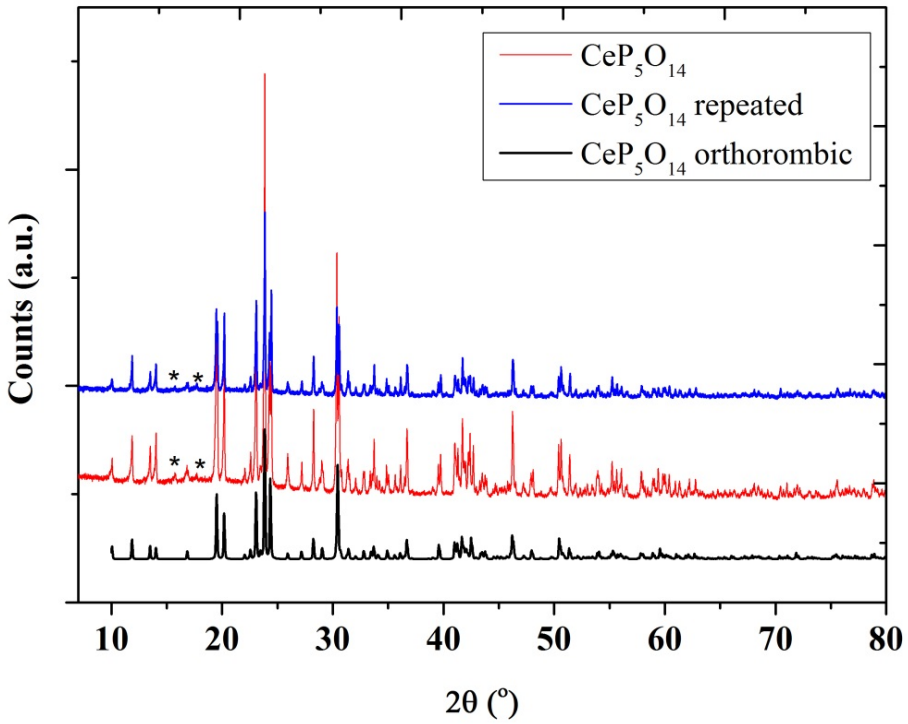


*Figure 8. 1 X-ray diffraction patterns of as prepared $CeP_5O_{14}$ powders*

The SEM image of the prepared powders is shown in *Figure 8. 2*. The crystals in form of beveled prisms are typical as a result of crystallization in orthorhombic systems.

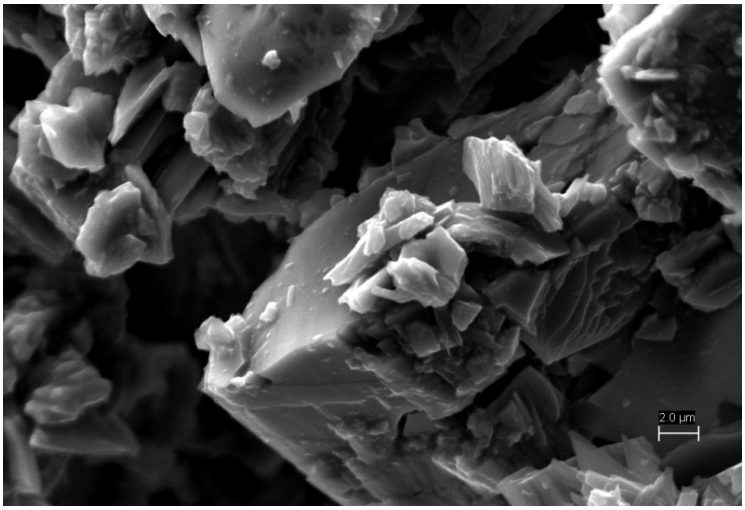


*Figure 8. 2 The typical SEM image of prepared $CeP_5O_{14}$ powders*

The crystal structure of cerium ultraphosphates obtained by the Atoms 63 software based on data for orthorhombic phase is presented in Figure 8. 3 (a). The main difference between ultraphosphates and orthophosphates (see Chapter 5 for the $NdPO_4$ monazite) is the isolated nature of the phosphate anion in these materials. The orthophosphates consist of isolated $PO_4$ tetrahedra that are sharing corners with $NdO_9$ polyhedra (nine fold coordination of the monazite form) whereas the ultraphosphate structure is more complex due to the condensation state of the phosphate anions. It is also on note that the $PO_4$ tetrahedra are linked by three vertices to neighbors. The overall structure of the $(P_5O_{14})^{3-}$ anion contains eight-membered conjugate rings and the coordination state of all rare earth cations in ultraphosphate structures is usually eight. This situation is schematically explained in Figure 8. 3 (b).

## 8.2 Thermal stability of the orthorhombic phase

It was mentioned previously that the ultraphosphate systems have not been well studied up to date [36]. In most cases the structural properties of the cerium ultraphosphate compounds have been investigated in relation to optical applications [165] with little information of their thermal properties. At higher temperatures around 900 - 1000°C the ultraphsophates have a tendency to decompose to metaphosphates.[166] In general it is known that all rare earth metal ultraphosphates, $LnP_5O_{14}$, decompose under long time heating according to the following equation:

$$LnP_5O_{14} \rightarrow LnPO_4 + 2P_2O_5 \qquad 8.1$$

The X-ray diffraction patterns of the prepared powder after being heat-treated for 6 hours at 150, 300, 400 and 650 °C, respectively, are shown in Figure 8. 4. At the heat-treatment temperatures

below 650 $^{o}$C, no polymorphic transformation was observed in the X-ray diffraction patterns of $CeP_5O_{14}$.

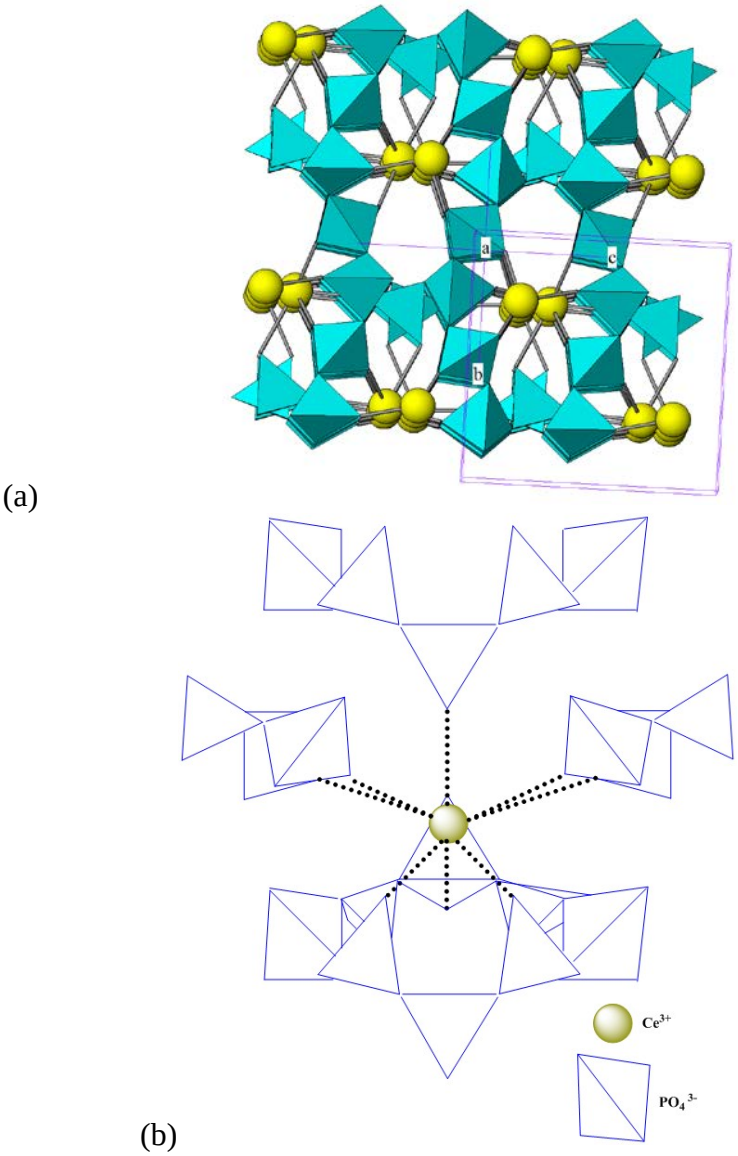


(a)

(b)

*Figure 8. 3 (a) View of the cerium ultraphosphate structure in polyhedral representation along the a-axis(b c plane) with denoted orthorhombic unit cell; (b) The schematic view showing phosphate ribbons linked by the cerium cation (shown along a-axis). The eight fold coordination of the $Ce^{3+}$ cation is denoted by black dot lines.*

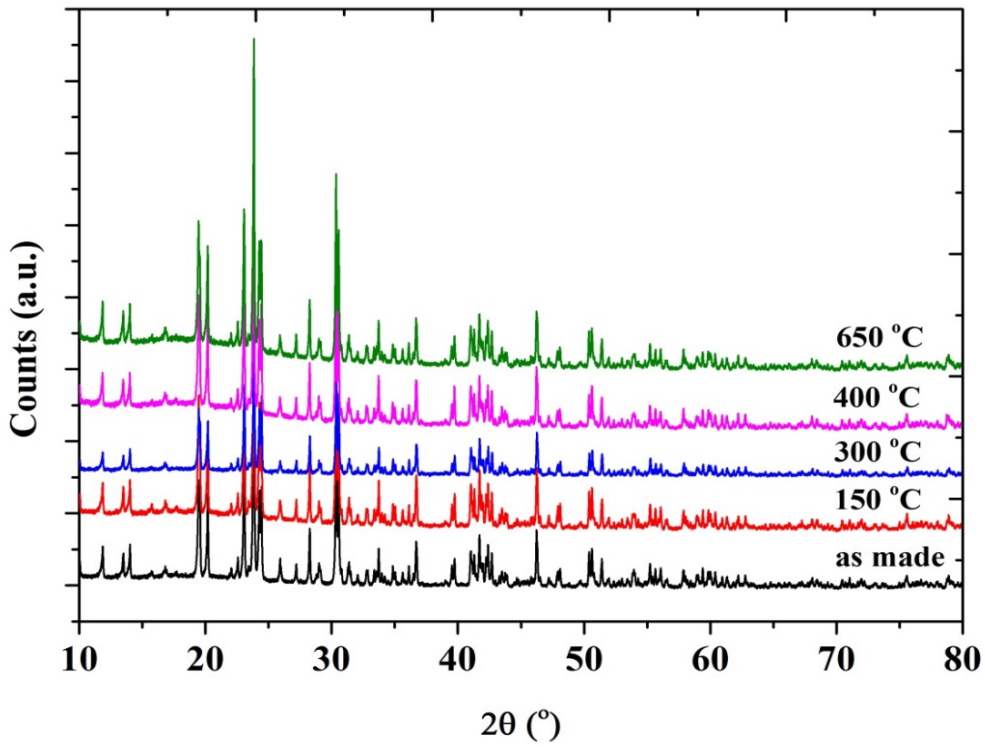


*Figure 8. 4 X-ray diffraction patterns of as made $CeP_5O_{14}$ powders as prepared and being heat-treated at different temperatures for a period of 6 hours, as indicated in the figure.*

## 8.3 FT-IR

The FT-IR spectra of the prepared cerium ultraphosphate and samples after being heat-treated for 6 hours at temperatures of 150, 300, 400 and 650 °C, respectively, are shown in Figure 8. 5. The entire spectra can be divided into two regions. The first region from about 500 - 1450 $cm^{-1}$ can be associated with an influence of structural groups of the ultraphosphate anion such as P-O, P=O (1265-1300 $cm^{-1}$ [163]), O-P-O [167], P-O-P (970, 750-830 $cm^{-1}$[163]) or linked $PO^{4-}$ tetrahedra (a strong band at around 1190 $cm^{-1}$). The second region which contains a wide band at about 1640-3600 $cm^{-1}$ can be assigned to the O-H stretching vibration based on the adsorbed water. The same wide band has been observed for tin pyrophosphate in Chapter 7. This band present in all spectra of samples that are as prepared or have been heat-treated at up to 300 °C. This indicates the thermal stability of adsorbed water or the possibility of recovering it during cooling after the samples have been treated. This wide band depends on surface properties and preparation of the powders. Onoda et al.[168] reported the influence of mechanochemical effects such as treatment with milling on appearance of this wide band.

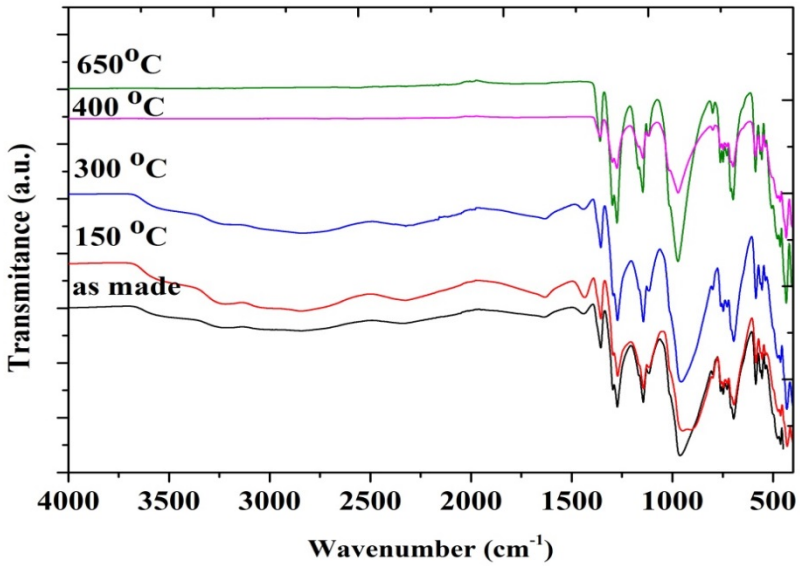


*Figure 8. 5 Typical FT-IR spectra of cerium ultraphsophate. Temperatures of heat treatment are indicated.*

It has been reported for the ultraphosphate glasses that the P-O-H linkage on the surface layer is more prominent [169,170]. Water attack on the surface of lanthanum zinc ultraphosphate glasses resulted in the formation of hydroxyapatite took place. Hydrolysis of this glasses proceeded in the direction of formation of pyrophosphates and then orthophosphate groups [169]. The above described process has been studied using spectral data in the region within about 2000-2400 $cm^{-1}$.There is no clear evidence of hydrolysis on the surface of the powders, however, as mentioned above and observed by Onoda et al.[168], the grinding of cerium ultraphosphate powders led to changes of the P-O-P to P-O-H bonding.

## 8.4 Conductivity

Figure 8. 6 presents the conductivity measured for two cerium orthophosphate samples separately synthesized. The measurements were done at a specific humidity of $P_{H_2O}$=0.15 atm. A steady increase was observed in the studied temperature range from 0.02 S $cm^{-1}$ at 120 °C to 0.025 S $cm^{-1}$ at 210 °C. At higher temperatures from 210 to 250 °C the conductivity exhibited a slight decrease.

By holding the sample at 250 °C and $P_{H_2O}$=0.15 atm for 18 hours, the conductivity was found to slowly increase reaching its maximum value of 0.033 S $cm^{-1}$ in 6 hours after a start of the experiment. In the following period, the conductivity showed a slight decrease. At the end of the period of 18 hours, the conductivity reached 0.03 S $cm^{-1}$.

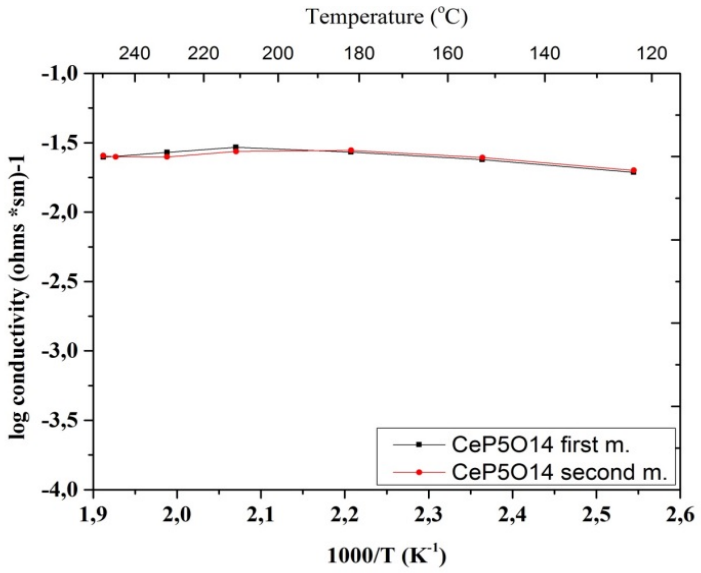


(A)

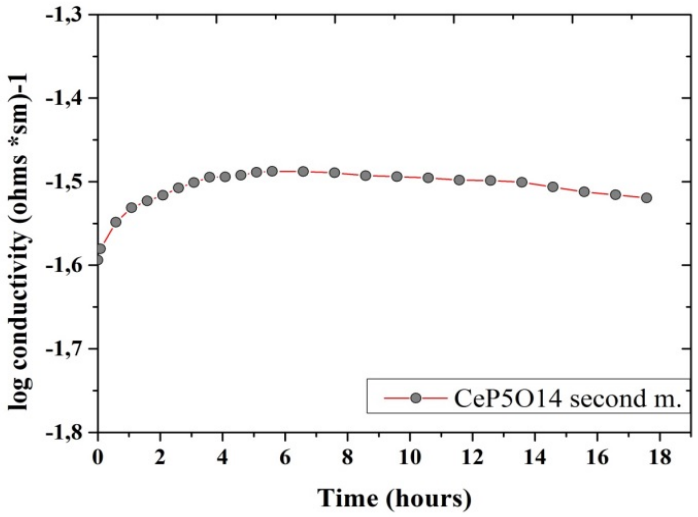


(B)

*Figure 8. 6 Conductivity of the $CeP_5O_{14}$ measured under a water partial pressure of $P_{H_2O}$ = 0.15 atm (A) and stability of the conductivity performed at 250 °C and $P_{H_2O}$ = 0.15 atm.*

## 8.5 Conclusions

The cerium ultraphosphates of the orthorhombic form were prepared. XRD analyses showed that this form of ultraphosphates was thermally stable after being heat-treated at temperatures of up to 650 °C. The existence of the OH group was revealed by FT-IR and remained at the heat-treatment temperatures of up to 300 °C. The conductivity in an atmosphere of $P_{H_2O}$ = 0.15 atm reached a value of 0.025 S $cm^{-1}$ at 210 °C and showed a slight decrease from 210 to 250 °C. As a preliminary study, the conductivity showed good stability within 18 hours under an atmosphere

with $P_{H_2O}$=0.15 atm, showing the potential of ultraphosphates as intermediate temperature proton conductors. Further work on the proton conduction mechanism and doping with other cations is recommended.

# Chapter

# 9 Conclusions and Perspectives

Great efforts are being made to develop new proton conducting materials as electrolyte for fuel cells operational at intermediate temperatures from 200 to 400 °C. This temperature range is of strategic importance, since it bridges the gap between the currently available high and low temperature fuel cells. Proton conductors with conductivities of above $10^{-2}$ $Scm^{-1}$ especially under low water content in the atmosphere are the key materials to achieve intermediate temperature operation of fuel cells. Phosphates are among the candidate materials due to their thermal, chemical and electrochemical stabilities in the temperature range. Of the most interesting phosphates are solid acids, pyrophosphates, ortho- and condensed phosphates of rare earth metal phosphates, which are the focus of the present project.

Hydrated orthophosphates of lanthanum, neodymium and gadolinium are prepared from the oxides by wet precipitation in phosphoric acid aqueous solutions and investigated as a candidate proton conducting electrolyte.

- Thermogravimetric analyses reveal that prepared rare earth phosphate hydrates have compositions of $LaPO_4$•$0.6H_2O$, $NdPO_4$•$0.5H_2O$ and $GdPO_4$•$0.5H_2O$, where two types of water molecules are present, the physically absorbed and structurally bound water.

- The absorbed water is of the surface nature, i.e. its presence is associated with the specific surface area of the phosphates. The structurally bound water is associated with the rhabdophane structure of the phosphates and stable at temperatures of up to 650 $^oC$.

- Above the 650 $^oC$ the dehydration of the structurally bound water happens and this process leads to an irreversible structural transformation from the hexagonal rbabdophane structure to the monoclinic monazite structure.

- The thermal stability of the hydrate water and the structure of the phosphates are of significance for the proton conductivity. The $LaPO_4 \cdot 0.6H_2O$ and $NdPO_4$•$0.5H_2O$ exhibit the conductivity and temperature dependence in good agreement with the theoretic estimation for their monazite analogues while the prepared $GdPO_4$•$0.5H_2O$ showed a significant effect of the phosphate morphology.

- $NdPO_4 \cdot 0.5H_2O$ shows a conductivity of around $10^{-6}$ $Scm^{-1}$ at 250 $^oC$ with a conductivity activation energy of 0.41 eV, while the conductivity of $LaPO_4 \cdot 0.6H_2O$ is around $10^{-7}$ $Scm^{-1}$ at 250 $^oC$.

Solid acid based proton conductors are long known for their high proton conductivity at temperatures above the super proton transition. For $CsH_2PO_4$ the transition temperature is around 230 $^oC$ where the dehydration occurs unless a humidified atmosphere is applied. The composite material based on the $NdPO_4$ hydrate and $CsH_2PO_4$ is prepared and characterized with the following findings:

- X-ray diffraction shows no solid evidence of new chemical compound formation between the two components, though a few weekly visible peaks on the diffractogram are not recognized, possibly the formation of traces of $CsH_5(PO_4)_2$.

- Thermogravimetric and differential thermal analyses reveal significant improvement in the thermal stability of cesium dihydrogen phosphate in terms of dehydration as neodymium phosphate is introduced.

- Significant enhancement in the proton conductivity is observed as compared to that of pristine cesium dihydrogen phosphates in a temperature range extended to both higher and lower regimes. Particularly at temperatures below the superprotonic transition point of the solid acid, significant conductivities are achieved for the composite.

- It is probable that the acid-base interaction between the two components establishes a dynamic hydrogen bonding network enabling efficient proton conduction long before the development of the extensive phase disordering of the superprotonic transition.

Metal pyrophosphates e.g. $SnP_2O_7$, often doped with other metals such as $In^{3+}$, possess high conductivities above $10^{-2}$ $Scm^{-1}$) at temperatures of up to 300 °C with little humidification. Aiming at elucidation of structures and conductivity mechanisms, indium doped tin phosphates are prepared via different routes. The study shows that

- Synthetic methods with either metal acetates or chlorides as precursors produce the pure or single crystalline phase of stoichiometric pyrophosphates as revealed by the XRD, FT-IR and NMR spectra.

- The heterogeneous synthesis from oxide precursors with excess of phosphoric acid gives pyrophosphates containing a phosphorus rich amorphous phase surrounding or along the grain boundaries of the crystalline particles.

- The amorphous phase is found to be responsible for the high and stable proton conductivity of the pyrophosphate achieved under low water vapor pressure (0.15 atm).

- The amorphous phase seems easy to hydrolyze in the presence of water or moisture, as evidenced by the OH-bands of FTIR and the orthophosphoric acid species by NMR.

- Washing in boiling water can remove the amorphous phase, causing agglomeration of the crystalline particles and a dramatic decrease in the conductivity.

Condensed phosphates of particularly rare earth metals represent an effective approach to development of new proton conductive materials. Cerium ultraphosphates is successfully prepared and studied:

- X-ray diffraction of prepared cerium ultraphosphate reveals the existence of the only orthorhombic phase, which is thermally stable with no phase transition at up to 650 $^{o}$C

- The existence of OH groups is confirmed by FT-IR spectra and found to be stable at heat-treatment temperatures of up to 300 $^{o}$C.

- Conductivity measurements in a temperature range of 120-250 $^{o}$C in an atmosphere with $P_{H_2O}$ = 0.15 atm show a maximum value of 0.025 $Scm^{-1}$ at 210 $^{o}$C. Reasonable stability within 18 hours is observed.

- Compared to rare earth metal orthophosphates, the ultraphosphates possess enhanced conductivity. Further exploration of the materials is highly recommended.

# 9 Conclusions and Perspectives

# Bibliography


1. Phair, J. W. & Badwal, S. P. S. Review of proton conductors for hydrogen separation. Ionics (Kiel). **12**, 103–115 (2006).

2. Kreuer, K.-D., Paddison, S. J., Spohr, E. & Schuster, M. Transport in Proton Conductors for Fuel-Cell Applications: Simulations, Elementary Reactions, and Phenomenology. Chem. Rev. **104**, 4637–4678 (2004).

3. Li, Q. High Temperature Proton Exchange Membranes for Fuel Cells. DTU dissertation of Doctor Technices. (2005).

4. Andujar, J. M. & Segura, F. Fuel cells: History and updating. A walk along two centuries. Renew. Sustain. Energy Rev. **13**, 2309–2322 (2009).

5. Wee, J.-H. Applications of proton exchange membrane fuel cell systems. Renew. Sustain. Energy Rev. **11**, 1720–1738 (2007).

6. Stone, C. & Morrison, A. E. From curiosity to “power to change the world.”Solid State Ionics **152-153**, 1–13 (2002).

7. Li, Q., Jensen, J. O., Savinell, R. F. & Bjerrum, N. J. High temperature proton exchange membranes based on polybenzimidazoles for fuel cells. Prog. Polym. Sci. **34**, 449–477 (2009).

8. Chisholm, C. R.I., Boysen D. A., Papandrew A. B., Zecevic S., Cha S., Sasaki K. A., Varga A., Giapis K. P. & Haile, S. M. From Laboratory Breakthrough to Technological Realization: The Development Path for Solid Acid Fuel Cells. Electrochem. Soc. Interface (2009).

9. Norby, T. Ceramic Proton and Mixed Proton-Electron Conductors in Membranes for Energy Conversion Applications. J. Chem. Eng. Japan **40**, 1166–1171 (2007).

10. Reijers R., Haije W. Literature review on high temperature proton conducting materials. Electrolyte for fuel cell or mixed conducting membrane for $H_2$ separation. (2008).

11. Garcia, A. L. T. Transition metal carbides for high temperature PEM water electrolysis. (2013).DTU PhD thesis.

12. Aili, D. Proton Conducting Polymeric Materials for Hydrogen Based Electrochemical Energy Conversion Technologies. (2011). DTU PhD thesis.

13. Haugsrud, R. Defects and transport properties in $Ln_6WO_{12}$(Ln=La, Nd, Gd, Er). Solid State Ionics **178**, 555–560 (2007).

14. Norby, T. Solid-state protonic conductors: principles, properties, progress and prospects. Solid State Ionics **125**, 1–11 (1999).

15. Harley, G., Yu, R. & De Jonghe, L. C. Proton transport paths in lanthanum phosphate electrolytes. Solid State Ionics **178**, 769–773 (2007).

16. Kreuer, K. D. On the development of proton conducting materials for technological applications. Solid State Ionics **97**, 1–15 (1997).

17. Goñi-Urtiaga, A., Presvytes, D. & Scott, K. Solid acids as electrolyte materials for proton exchange membrane (PEM) electrolysis: Review. Int. J. Hydrogen Energy **37**, 3358–3372 (2012).

18. Colomban P. Chemistry of Solid State Materials. Proton conductors: Solid, membranes and gels-materials and devices. (Cambridge University Press, 1992).

19. Fragua D. M., Castillo J., Castillo R. & Vargas, R. A. New amorphous phase $K_nH_2PnO_{3n+1}$(n>>1) in $KH_2PO_4$. Supl. la Rev. Latinoam. Metal. y Mater. **S1 (2)**, 491–497 (2009).

20. Baranov, A. I., Khiznichenko, V. P., Sandler, V. A. & Shuvalov, L. A. Frequency dielectric dispersion in the ferroelectric and superionic phases of $CsH_2PO_4$. Ferroelectrics **81**, 183–186 (1988).

21. Barboux, P., Morineau, R. & Livage, J. Protonic conductivity in hydrates. Solid State Ionics **27**, 221–225 (1988).

22. Barboux, P. & Livage, J. Ionic conductivity in fibrous $Ce(HPO_4)_2$*(3+x)H2O. Solid State Ionics **34**, 47–52 (1989).

23. Barboux, P., Baffier, N., Morineau, R. & Livage, J. Diffusion protonique dans les xerogels de pentoxyde de vanadium. Solid State Ionics **9-10**, Pa, 1073–1080 (1983).

24. Skou, E., Andersen, I. G. K., Simonsen, K. E. & Andersen, E. K. Is $UO_2HPO_4$•$4H_2O$ a proton conductor? Solid State Ionics **9-10**, 1041–1047 (1983).

25. Rice, C. E. J. Solid State Chem. **64**, 188–189 (1986).

26. Baranov A.I., Merinov B.V., Tregubchenko A.B., Shuvalov L.A. & Shchagina, N. M.. Ferroelectrics **81**, 187–191 (1988).

27. Paschos O., Kunze J., Stimming U. & Maglia, F. A review on phosphate based, solid state, protonic conductors for intermediate temperature fuel cells. J. Phys. Condens. Matter **23**, (2011).

28. Haile S. M., Chisholm C. R. I., Sasaki K., Boysen D. A. & Uda, T. Solid acid proton conductors: from laboratory curiosities to fuel cell electrolytes. Faraday Discuss. **134**, 17–39 (2007).

29. Haile, S. M., Boysen, D. A, Chisholm, C. R. & Merle, R. B. Solid acids as fuel cell electrolytes. Nature **410**, 910–3 (2001).

30. Wieczorek, W., Żukowska, G., Borkowska, R., Chung, S. H. & Greenbaum, S. A basic investigation of anhydrous proton conducting gel electrolytes. Electrochim. Acta **46**, 1427–1438 (2001).

31. Matsuda, A., Kanzaki, T., Tadanaga, K., Tatsumisago, M. & Minami, T. Medium temperature range characterization as a proton conductor for phosphosilicate dry gels containing large amounts of phosphorus. Electrochim. Acta **47**, 939–944 (2001).

32. Nogami, M., Suwa, M. & Kasuga, T. Proton conductivity in solgel-derived $P_2O_5$-$TiO_2$-$SiO_2$ glasses. Solid State Ionics **166**, 39–43 (2004).

33. Nogami, M., Kato, A., Nakayama, M. & Lakshminarayana, G. Proton conduction in ionic liquid-modified $P_2O_5$-$SiO_2$ glasses. J. Non. Cryst. Solids **358**, 3495–3500 (2012).

34. Uma, T. & Nogami, M. On the development of proton conducting $P_2O_5$-$ZrO_2$-$SiO_2$ glasses for fuel cell electrolytes. Mater. Chem. Phys. **98**, 382–388 (2006).

35. Furuhashi, Y., Shimada, I., Otomo, J. & Oshima, Y. Fast proton transport in zinc phosphorous glass composites. Mater. Chem. Phys. **127**, 322–328 (2011).

36. Averbuch-Pouchot M-T., Durif A. Topics in phosphate chemistry. (World Scientific, 1996).

37. Lee, K.-S. Hidden nature of the high-temperature phase transitions in crystals of $KH_2PO_4$ : Is it a physical change ? J. Phys. Chem. Solids **57(3)**, 333–342 (1996).

38. Taninouchi, Y., Uda, T., Awakura, Y., Ikeda, A. & Haile, S. M. Dehydration behavior of the superprotonic conductor $CsH_2PO_4$ at moderate temperatures: 230 to 260 [degree]C. J. Mater. Chem. **17**, 3182–3189 (2007).

39. Taninouchi, Y., Uda, T. & Awakura, Y. Dehydration of $CsH_2PO_4$ at temperatures higher than 260 $^oC$ and the ionic conductivity of liquid product. Solid State Ionics **178**, 1648–1653 (2008).

40. Goni-Urtiaga, A., Presvytes, D. & Scott, K. Solid acids as electrolyte materials for proton exchange membrane (PEM) electrolysis: Review. Int. J. Hydrogen Energy **37**, 3358–3372 (2012).

41. Rapoport, E., Clark, J. B. & Richter, P. W. High-pressure phase relations of $RbH_2PO_4$, $CsH_2PO_4$, and $\{KD_2PO_4\}$. J. Solid State Chem. **24**, 423–433 (1978).

42. Croce, F. & Cigna, G. Determination of the protonic transference number for $KH_2PO_4$ by electromotive force measurements. Solid State Ionics **6**, 201–202 (1982).

43. Fritz, I. J. Anomalous acoustic behavior of $KH_2PO_4$ at high pressure. Solid State Commun. **12**, 79–81 (1973).

44. Furuta, H., Endo, S., Tokunaga, M., Tominaga, Y. & Kobayashi, M. Local distortion of $PO_4$ tetrahedra in the paraelectric phase in low temperature under high pressure in $KH_2PO_4$. Solid State Commun. **117**, 7–11 (2000).

45. O'Keeffe, M. & Perrino, C. T. Proton conductivity in pure and doped $KH_2PO_4$. J. Phys. Chem. Solids **28**, 211–218 (1967).

46. Ortiz E., Vargas A. & Mellander, B. E. On the reported high-temperature phase transition in $KH_2PO_4$ - strong evidence of partial polymerization instead of a structural phase transition. J. Phys. Chem. Solids **59**, 305–310 (1998).

47. Bjerrum, N. Structure and Properties of Ice. Science **115**, 385–391 (1952).

48. Yamada, K., Sagara, T., Yamane, Y., Ohki, H. & Okuda, T. Superprotonic conductor $CsH_2PO_4$ studied by $^{1}H$, $^{31}P$ NMR and X-ray diffraction. Solid State Ionics **175**, 557–562 (2004).

49. Boysen D. A., Haile S. M., Liu H. J., & Secco R. High-Temperature Behavior of $CsH_2PO_4$ under Both Ambient and High Pressure Conditions. Chem. Mater. **15**, 727–736 (2003).

50. Boysen D. A., Uda T., Chisholm C. R. I. & Haile, S. M. High-Performance Solid Acid Fuel Cells Through Humidity Stabilization. Science **303**, 68–70 (2004).

51. J. Otomo, T. Tamaki, S. Nishida, S. Wang, M. Ogura, T. Kobayashi, C. Wen, H. Nagamoto, &Takahashi, H. Effect of water vapor on proton conduction of cesium dihydrogen phosphateand application to intermediate temperature fuel cells. J. Appl. Electrochem. **35**, 865–870 (2005).

52. Boysen, D. A., Haile, S. M., Liu, H. & Secco, R. A. High-Temperature Behavior of $CsH_2PO_4$ under Both Ambient and High Pressure Conditions. Chem. Mater. **15**, 727–736 (2003).

53. Baranov, A. I., Grebenev, V. V, Khodan, A. N., Dolbinina, V. V & Efremova, E. P. Optimization of superprotonic acid salts for fuel cell applications. Solid State Ionics **176**, 2871–2874 (2005).

54. Matsui, T., Kukino, T., Kikuchi, R. & Eguchi, K. Intermediate-Temperature Fuel Cell Employing $CsH_2PO_4$ / $SiP_2O_7$-Based Composite Electrolytes. J. Electrochem. Soc. **153**, A339–A342 (2006).

55. Insani E. K., Nguyen V. H, Kawamura G., Hamagami, Jun-Ichi, Sakai, M., Matsuda A. & Yuliarto B. Proton conductivity of $CsH_2PO_4$ ● WPA composites at intermediate

temperatures. Third Nanosci. Nanotechnol. Symp. 2010 (NNSB2010). AIP Conf. Proc. 1284, 42–45 (2010).

56. Otomo, J., Ishigooka, T., Kitano, T., Takahashi, H. & Nagamoto, H. Phase transition and proton transport characteristics in $CsH_2PO_4/SiO_2$ composites. Electrochim. Acta **53**, 8186–8195 (2008).

57. Lavrova, G. V, Shutova, E. S., Ponomareva, V. G. & Dunyushkina, L. A. Proton conductivity and interphase interaction in $CsH_2PO_4$-$SrZrO_3$ composites. Russ. J. Electrochem. **49**, 718–724 (2013).

58. Otomo, J., Minagawa, N., Wen, C., Eguchi, K. & Takahashi, H. Protonic conduction of CsH2PO4 and its composite with silica in dry and humid atmospheres. Solid State Ionics **156**, 357–369 (2003).

59. Ponomareva, V. G. & Shutova, E. S. High-temperature behavior of $CsH_2PO_4$ and $CsH_2PO_4$-$SiO_2$ composites. Solid State Ionics **178**, 729–734 (2007).

60. Muroyama, H., Katsukawa, K., Matsui, T. & Eguchi, K. Tungsten-based Carbides as Anode for Intermediate-Temperature Fuel Cells. J. Electrochem. Soc. **158** , B1072–B1075 (2011).

61. Matsui T., Muroyama H., & Eguchi, R. K. Development of novel proton conductors consisting of solid acid/ pyrophosphate composite for Intermediate-temperature fuel cells. J. Japan Pet. Inst. **53(1),** 1–10 (2010).

62. Jensen, T. R., Norby, P., Stein, P. C. & Bell, A. M. T. Preparation, Structure Determination and Thermal Transformation of a New Lithium Zinc Phosphate, $\delta_1$-$LiZnPO_4$. J. Solid State Chem. **117**, 39–47 (1995).

63. Bocchetta, P., Ferraro, R. & Quarto, F. Di. Advances in anodic alumina membranes thin film fuel cell: $CsH_2PO_4$ pore-filler as proton conductor at room temperature. J. Power Sources **187**, 49–56 (2009).

64. Oh S., Insani E. K., Nguyen V. H, Kawamura G., Muto H., Sakai M. & Matsuda, A. Mechanochemically synthesized $CsH_2PO_4$-$H_3PW_{12}O_{40}$ composites as proton-conducting electrolytes for fuel cell systems in a dry atmosphere. Sci. Technol. Adv. Mater. **12**, (2011).

65. Oh S., Kawamura G., Muto H. & Matsuda, A. Anhydrous Proton Conductivities of $CsH_2PO_4$-$C_5H_5N_5O$ Composite Prepared by Mechanochemically Treatment.

66. Oh, S., Kawamura, G., Muto, H. & Matsuda, A. Mechanochemical synthesis of proton conductive composites derived from cesium dihydrogen phosphate and guanine. Solid State Ionics **225**, 223–227 (2012).

67. Muroyama, H., Matsui, T., Kikuchi, R. & Eguchi, K. Correlation Between Conduction Behavior of $CsH_5(PO_4)_2$ and Thermal History. J. Electrochem. Soc. **155** , B958–B962 (2008).

68. Gover, R. K. B., Withers, N. D., Allen, S., Withers, R. L. & Evans, J. S. O. Structure and Phase Transitions of $SnP_2O_7$. J. Solid State Chem. **166**, 42–48 (2002).

69. Nagao, M. et al. Proton Conduction in $In^{3+}$ Doped $SnP_2O_7$ at Intermediate Temperatures. J. Electrochem. Soc. **153**, A1604–A1609 (2006).

70. Tomita, A., Kajiyama, N., Kamiya, T., Nagao, M. & Hibino, T. Intermediate-Temperature Proton Conduction in $Al^{3+}$ Doped $SnP_2O_7$. J. Electrochem. Soc. **154**, B1265–B1269 (2007).

71. Yoshimi, S., Matsui, T., Kikuchi, R. & Eguchi, K. Temperature and humidity dependence of the electrode polarization in intermediate-temperature fuel cells employing CsH2PO4/SiP2O7-based composite electrolytes. J. Power Sources **179**, 497–503 (2008).

72. Y. Jin, Y. Sato & Hibino, T. Proton conduction in metal pyrophosphates (MP2O7) at intermediate temperatures. J. Mater. Chem. **20**, 6214–6217 (2010).

73. Chang, Y. Keijiro Kojima , Masakazu Nishida , Pilwon Heo , Kyoung Hwan Choi , Hyuk Chang & Hibino, T. Proton conduction in AIII0.5BV0.5P2O7 compounds at intermediate temperatures. J. Mater. Chem. **22**, 14907 (2012).

74. Kanematsu, Y, Yanbai Shen , Masakazu Nishida , Wataru Kanematsu & Hibino, T. Proton conduction in non-doped and acceptor-doped metal pyrophosphate ($MP_2O_7$) composite ceramics at intermediate temperatures. J. Mater. Chem. **22**, 3973–3981 (2012).

75. Hibino, T. Intermediate-temperature proton conductors and their applications to energy and environmental devices. J. Ceram. Soc. Japan **119**, 677–686 (2011).

76. Genzaki, K., Heo, P., Sano, M. & Hibino, T. Proton Conductivity and Solid Acidity of Mg-, In-, and Al-Doped $SnP_2O_7$. J. Electrochem. Soc. **156**, B806–B810 (2009).

77. Tao, S. Conductivity of $SnP_2O_7$ and In-doped $SnP_2O_7$ prepared by an aqueous solution method. Solid State Ionics **180**, 148–153 (2009).

78. Wu, X., Verma, A. & Scott, K. A Sb-doped $SnP_2O_7$ Solid Proton Conductor for Intermediate Temperature Fuel Cells. Fuel Cells **8**, 453–458 (2008).

79. Nalini, V., Haugsrud, R. & Norby, T. High-temperature proton conductivity and defect structure of TiP2O7. *Solid State Ionics* **181,** 510–516 (2010).

80. Nalini V., Amezawa K., Xing W. & Norby, T. High Temperature Proton Conductivity of ZrP2O7. *J. Electrochem. Soc.* **157(10),** B1491–B1498 (2010).

81. Lapina A., Chatzichristodoulou C., Hallinder J., Holtappels P.& Mogensen M. Electrical conductivity of titanium pyrophosphate between 100 and 400 $^{o}$C: effect of sintering temperature and phosphorus content. *J. Solid State Electrochem.* **18,** 39–47 (2014).

82. Norby, T. & Christiansen, N. Proton conduction in Ca- and Sr-substituted $LaPO_4$. Solid State Ionics **77**, 240–243 (1995).

83. Amezawa, K., Maekawa, H., Tomii, Y. & Yamamoto, N. Protonic conduction and defect structures in Sr-doped $LaPO_4$. Solid State Ionics **145**, 233–240 (2001).

84. Amezawa, K., Kjelstrup, S., Norby, T. & Ito, Y. Protonic and Native Conduction in Sr-Substituted $LaPO_4$ Studied by Thermoelectric Power Measurements. J. Electrochem. Soc. **145**, 3313–3319 (1998).

85. Kitamura, N., Amezawa, K., Tomii, Y. & Yamamoto, N. Protonic conduction in rare earth orthophosphates with the monazite structure. Solid State Ionics **162–163**, 161–165 (2003).

86. Gallini, S., Hansel, M., Norby, T., Colomer, M. T. & Jurado, J. R. Impedance spectroscopy and proton transport number measurements on Sr-substituted $LaPO_4$ prepared by combustion synthesis. Solid State Ionics $_{162\text{-}163}$, 167–173 (2003).

87. Kitamura, N. et al. Electrical Conduction Properties of Sr-Doped $LaPO_4$ and $CePO_4$ under Oxidizing and Reducing Conditions. J. Electrochem. Soc. **152**, A658–A663 (2005).

88. Toyoura K., Hatada N., Nose Y., Tanaka I., Matsunaga K. & Uda, T. Proton Conducting Network in Lanthanum Orthophosphate. J. Phys. Chem. C (2012).

89. S. Phadke J. C. Nino & Islam, M. S. Structural and defect properties of the $LaPO_4$ and LaP5O14-based proton conductors. J. Mater. Chem. **22**, 25388 (2012).

90. Oesten, R. & Huggins, R. A. Proton conduction in oxides: A review. Ionics (Kiel). **1**, 427–437 (1995).

91. Kitamura, N., Amezawa, K., Tomii, Y., Yamamoto, N. & Hanada, T. Protonic conduction in Sr-doped $(La1-xSmx)PO_4$. Solid State Ionics **175**, 563–567 (2004).

92. Amezawa, K., Tomii, Y. & Yamamoto, N. High temperature protonic conduction in $Sr_2P_2O_7$–$LaPO_4$ system. Solid State Ionics **176**, 143–148 (2005).

93. Amezawa, K., Tomii, Y. & Yamamoto, N. High temperature protonic conduction in $LaPO_4$ doped with alkaline earth metals. Solid State Ionics **176**, 135–141 (2005).

94. Kitamura, N., Amezawa, K., Tomii, Y., Hanada, T. & Yamamoto, N. Electrical conduction in Sr-doped $(La_{0.99}Ce_{0.01})PO_4$. Solid State Ionics **176**, 2875–2879 (2005).

95. Amezawa, K., Nishikawa, Y., Tomii, Y. & Yamamoto, N. Electrical and Mechanical Properties of Sr-Doped $LaPO_4$ Prepared by Spark Plasma Sintering. J. Electrochem. Soc. **152**, A1060–A1067 (2005).

96. Kitamura, N. et al. Electrical conduction properties of rare earth orthophosphates under reducing conditions. Solid State Ionics **177**, 2369–2373 (2006).

97. Amezawa, K., Tomii, Y. & Yamamoto, N. High temperature protonic conduction in Ca-doped $YPO_4$. Solid State Ionics **162–163**, 175–180 (2003).

98. Byrappa, K. & Litvin, B. N. Hydrothermal synthesis of mixed phosphates of neodymium and alkaline metals ($Me_2O•Nd_2O_3•4P_2O_5$). J. Mater. Sci. **18**, 703–708 (1983).

99. Junichi N., Kubodera K., Yamada T. & Miyazawa, S. Laser-emission cross sections of $MeNdP_4O_{12}$ (Me=Li, Na, K) crystals. J. Appl. Phys. **50**, 6492–6499 (1979).

100. Belam, W. & Mechergui, J. Synthesis, X-ray diffraction study and physico-chemical characterizations of $KLaP_4O_{12}$. Mater. Res. Bull. **43**, 2308–2317 (2008).

101. Rzaigui, M. & Ariguib, N. K. Preparation and characterization of some crystalline condensed cerium-ammonium phosphates. J. Solid State Chem. **49**, 391–398 (1983).

102. Masse, R., Guitel, J.-C. & Durif, A. Structure cristalline du tetrametaphosphate de praseodyme-ammonium, $PrNH_4P_4O_{12}$. Donnees cristallographiques de $NdNH_4P_4O_{12}$. Acta Crystallogr. Sect**. B 33**, 630–632 (1977).

103. Koizumi, H. & Nakano, J. Rubidium neodymium metaphosphate. Acta Crystallogr. Sect. **B 33**, 2680–2684 (1977).

104. Zhu, D., Luo, F., Xie, Z. & Zhou, W. Preparation and characteristic of NASICON ceramics. Rare Met. **25**, 39–42 (2006).

105. Yamanaka, S. Ionic conductivity in anhydrous crystalline zirconium phosphates, $Zr(MPO_4)_2$ (M=Li, Na, K), with layered structures. J. Inorg. Nucl. Chem. $_{42}$, 717–720 (1980).

106. Clearfield, A. & Stynes, J. A. The preparation of crystalline zirconium phosphate and some observations on its ion exchange behaviour. J. Inorg. Nucl. Chem. **26**, 117–129 (1964).

107. Alberti, G., Casciola, M., Costantino, U. & Vivani, R. Layered and pillared metal(IV) phosphates and phosphonates. Adv. Mater. **8**, 291–303 (1996).

108. Park, C.-J., Kim, D.-H., Kim, J.-K., Lee, J.-S. & Song, S.-J. Synthesis of Proton-Conducting, In-Doped $SnP_2O_7$ Core-Shell-Structured Nanoparticles by Coprecipitation. J. Electrochem. Soc. **156**, E23–E25 (2009).

109. Xu, X., Tao, S., Wormald, P. & Irvine, J. T. S. Intermediate temperature stable proton conductors based upon $SnP_2O_7$ including additional $H_3PO_4$. J. Mater. Chem. **20**, 7827–7833 (2010).

110. Zhu, J., Cheng, W.-D. & Zhang, H. An orthorhombic polymorph of cerium(III) ultraphosphate, $CeP_5O_{14}$. Acta Crystallogr. Sect. **E 64**, 74 (2008).

111. http://www.purdue.edu/rem/rs/sem.htm

112. Massa, W. Crystal Structure Determination Second Edition. (Springer, 2004).

113. www.icdd.com

114. Ståhl, K. Powder diffraction and the Rietveld method. (Department of Chemistry, 2011).

115. S.P. Jiang, J. G. Love & Badwal, S. P. S. Electrochemical techniques in studies of solid ionic conductors. Key Eng. Mater. **125-126**, 81–132 (1997).

116. Bauerle, J. E. Study of solid electrolyte polarization by a complex admittance method. J. Phys. Chem. Solids **30**, 2657–2670 (1969).

117. Pletcher D., Greef R., Peat R., Peter L.M., Robinson J.. Instrumental Methods in Electrochemistry. (Horwood Publishing, 2001).

118. Barsoukov E. & Ross Macdonald J. Impedance Spectroscopy. Theory, Experiment and Application. (Wiley-Interscience, 2005).

119. Yuan X-Z., Song C., Wang H. & Zhang, J. Electrochemical Impedance Spectroscopy in PEM Fuel Cells. Fundamentals and Application. (Springer, 2010).

120. Jorcin, J.-B., Orazem, M. E., Pebere, N. & Tribollet, B. CPE analysis by local electrochemical impedance spectroscopy. Electrochim. Acta **51**, 1473–1479 (2006).

121. Hirschorn B., Orazem M. E., Tribollet B., Vivier V., Frateur I. & Musiani, M. Constant-Phase-Element Behavior Caused by Resistivity Distributions in Films: I. Theory. J. Electrochem. Soc. **157**, 452–457 (2010).

122. Lasia, A. in Mod. Asp. Electrochem. (Conway, B. E., Bockris, J. O. & White, R.) **32**, 143–248 (Springer US, 2002).

123. Ni Y., Hughes J. M. & Mariano, A. N. Crystal chemistry of the monazite and xenotime structures. Am. Mineral. **80**, 21–26 (1995).

124. Park, H. D. & Kreidler, E. R. Phase Equilibria in the System $La_2O_3$-$P_2O_5$. J. Am. Ceram. Soc. **67**, 23–26 (1984).

125. Hannah L. Ray, L. D. J. & Wang, R. Rare Earth Phosphate Glass and Glass-Ceramic Proton Conductors. ECS Trans. **16(51),** 389–393 (2009).

126. Amezawa, K., Tomiga, T., Yamamoto, N., Hanada, T. & Tomii, Y. Electrical Conduction Properties of $LaP_3O_9$ Glass and Glass–Ceramics. J. Am. Ceram. Soc. **88**, 3211–3214 (2005).

127. Amezawa, K. et al. Protonic conduction in acceptor-doped $LaP_3O_9$. Solid State Ionics **176**, 2867–2870 (2005).

128. Amezawa, K., Uchimoto, Y. & Tomii, Y. High temperature protonic conduction in Sr-doped $LaP_3O_9$. Solid State Ionics **177**, 2407–2411 (2006).

129. Phadke, S. R. & Nino, J. C. Conductivity Enhancement in Lanthanum Phosphates. J. Am. Ceram. Soc. **94**, 1817–1823 (2011).

130. Unemoto, A., Amezawa, K. & Kawada, T. Electrical conductivities of strontium-doped rare earth ultraphosphates and oxyphosphates. J. Electroceramics **29**, 29–36 (2012).

131. Hammas, I., Horchani-Naifer, K. & Férid, M. Conduction properties of condensed lanthanum phosphates: $La(PO_3)_3$ and $LaP_5O_{14}$. J. Rare Earths **28**, 321–328 (2010).

132. Jorgensen S., Horst J.A., Dyrlie O., Larring Y., Ræder H. & Norby, T. XPS surface analyses of $LaPO_4$ ceramics prepared by precipitation with or without excess of $(PO_4)^{3-}$. Surf. Interface Anal. **34**, 306–310 (2002).

133. Lucas, S., Champion, E., Bregiroux, D., Bernache-Assollant, D. & Audubert, F. Rare earth phosphate powders $RePO_4{\bullet}nH_2O$ (Re=La, Ce or Y)—Part I. Synthesis and characterization. J. Solid State Chem. **177**, 1302–1311 (2004).

134. Bowles, J. F. W. & Morgan, D. J. The Composition of Rhabdophane. Mineral. Mag. **48**, 146–148 (1984).

135. Mooney, R. C. L. X-ray diffraction study of cerous phosphate and related crystals. I. Hexagonal modification. Acta Crystallogr. **3**, 337–340 (1950).

136. Shannon, R. D. Revised effective ionic radii and systematic studies of interatomic distances in halides and chalcogenides. Acta Crystallogr. **A32**, 751–767 (1976).

137. Dronskowski, R. H. Computational Chemistry of Solid State Materials: A Guide for Materials Scientists, Chemists, Physicists and others. (WILEY-VCN, 2005).

138. Mullica, D. F., Milligan, W. O., Grossie, D. A., Beall, G. W. & Boatner, L. A. Ninefold coordination $LaPO_4$: Pentagonal interpenetrating tetrahedral polyhedron. Inorganica Chim. Acta **95**, 231–236 (1984).

139. Mooney, R. C. L. X-ray diffraction study of cerous phosphate and related crystals. I. Hexagonal modification. Acta Crystallogr. **3**, 337–340 (1950).

140. Mullica, D. F., Grossie, D. A. & Boatner, L. A. Structural refinements of praseodymium and neodymium orthophosphate. J. Solid State Chem. **58**, 71–77 (1985).

141. Mullica, D. F., Grossie, D. A. & Boatner, L. A. Coordination geometry and structural determinations of $SmPO_4$, $EuPO_4$ and $GdPO_4$. Inorganica Chim. Acta **109**, 105–110 (1985).

142. Scheetz B., Pfoertsch D., Zellmer L. & Smith D.. JCPDS Grant-in-Aid Rep. (1987).

143. Halford, R. S. Motions of Molecules in Condensed Systems: I. Selection Rules, Relative Intensities, and Orientation Effects for Raman and Infra-Red Spectra. J. Chem. Phys. **14**, 8–15 (1946).

144. Assaaoudi, H., Ennaciri, A. & Rulmont, A. Vibrational spectra of hydrated rare earth orthophosphates. Vib. Spectrosc. **25**, 81–90 (2001).

145. Diaz-Guillen, J. A., Fuentes, A. F., Gallini, S. & Colomer, M. T. A rapid method to obtain nanometric particles of rhabdophane $LaPO_4 \bullet nH_2O$ by mechanical milling. J. Alloys Compd. **427**, 87–93 (2007).

146. Yu, R. & De Jonghe, L. C. Proton-Transfer Mechanism in $LaPO_4$. J. Phys. Chem. **C 111**, 11003–11007 (2007).

147. Davis, J. B., Marshall, D. B. & Morgan, P. E. D. Monazite-containing oxide/oxide composites. J. Eur. Ceram. Soc. **20**, 583–587 (2000).

148. Davis, J. B., Marshall, D. B., Housley, R. M. & Morgan, P. E. D. Machinable Ceramics Containing Rare-Earth Phosphates. J. Am. Ceram. Soc. **81**, 2169–2175 (1998).

149. Oh, S., Kawamura, G., Muto, H. & Matsuda, A. Anhydrous protic conduction of mechanochemically synthesized $CsHSO_4$-Azole-derived composites. Electrochim. Acta **75**, 11–19 (2012).

150. Kerres, J. A. Blended and Cross-Linked Ionomer Membranes for Application in Membrane Fuel Cells. Fuel Cells **5**, 230–247 (2005).

151. Aili, D., Hansen M.K., Pan C., Li Q., Christensen E., Jensen J. O. & Bjerrum N. J.. Phosphoric acid doped membranes based on Nafion®, PBI and their blends – Membrane preparation, characterization and steam electrolysis testing. Int. J. Hydrogen Energy **36**, 6985–6993 (2011).

152. Huang Y., Li Q., Jensen A. H., Min Yin, Jens Oluf Jensen, Erik Christensen, Chao Pan, Niels J. Bjerrum & Wei Xing. Niobium phosphates as an intermediate temperature proton conducting electrolyte for fuel cells. J. Mater. Chem. **22**, 22452 (2012).

153. Huang Y., Li Q., Anfimova T. V., Christensen E., Yina M., Jensen J. O., Bjerrum N. J. & Xing W.. Indium doped niobium phosphates as intermediate temperature proton conductors. Int. J. Hydrogen Energy (2012).

154. Jin, Y., Fujiwara, K. & Hibino, T. High Temperature, Low Humidity Proton Exchange Membrane Based on an Inorganic–Organic Hybrid Structure. Electrochem. Solid-State Lett. **13**, B8–B10 (2010).

155. Chen, X., Wang, C., Payzant, E. A., Xia, C. & Chu, D. An Oxide Ion and Proton Co-Ion Conducting $Sn_{0.9}In_{0.1}P_2O_7$ Electrolyte for Intermediate-Temperature Fuel Cells. J. Electrochem. Soc. **155**, B1264–B1269 (2008).

156. Nagao, M., Yoshii, T., Hibino, T., Sano, M. & Tomita, A. Electrochemical Reduction of NO x at Intermediate Temperatures Using a Proton-Conducting $In^{3+}$-Doped $SnP_2O_7$ Electrolyte. Electrochem. Solid-State Lett. **9**, J1–J4 (2006).

157. Iwahara, H., Esaka, T., Uchida, H., Yamauchi, T. & Ogaki, K. High temperature type protonic conductor based on $SrCeO_3$ and its application to the extraction of hydrogen gas. Solid State Ionics **18-19**, P, 1003–1007 (1986).

158. Bonanos, N., Knight, K. S. & Ellis, B. Perovskite solid electrolytes: Structure, transport properties and fuel cell applications. Solid State Ionics **79**, 161–170 (1995).

159. Unemoto, A., Kitamura, N., Amezawa, K. & Kawada, T. Hydrogen Permeation Properties in ( Ce , Sr ) $PO_4$. Electrochem. Solid-State Lett. **12**, B43–B47 (2009).

160. Singh, B., Im, H.-N., Park, J.-Y. & Song, S.-J. Electrical Behavior of $CeP_2O_7$ Electrolyte for the Application in Low-Temperature Proton-Conducting Ceramic Electrolyte Fuel Cells. J. Electrochem. Soc. **159**, F819–F825 (2012).

161. Sun, X., Shaorong Wang, Zhenrong Wang, Xiaofeng Ye, Tinglian Wen & Fuqiang Huang Proton conductivity of $CeP_2O_7$ for intermediate temperature fuel cells. Solid State Ionics **179**, 1138–1141 (2008).

162. Tsuhako, M., Ikeuchi, S., Matsuo, T., Motooka, I. & Kobayashi, M. Conditions of the Formation of Rare Earth Phosphates and the Colors of Their Powders. Bull. Chem. Soc. Jpn. **52**, 1034–1040 (1979).

163. Ninisto, L. & Leskela, M. Handbook on the Physics and Chemistry of Rare Earth (Chapter 59 Inorganic complex compounds). (Elsevier Science, 1987).

164. Rzaigui, M. & Ariguib, N. K. Preparation chimique et proprietes optiques de $CeP_5O_{14}$ triclinique. J. Solid State Chem. **56**, 122–125 (1985).

165. Szczygiel, I. & Znamierowska, T. The synthesis and thermal stability of cerium ultraphosphate. J. Therm. Anal. Calorim. **36**, 2195–2198 (1990).

166. Abid, M., Et-tabirou, M. & Taibi, M. Structure and DC conductivity of lead sodium ultraphosphate glasses. Mater. Sci. Eng. **B 97**, 20–24 (2003).

167. Onoda H., Nariai H., Maki H.& Motooka, I. Mechanochemical effects of some rare-earth ultraphosphates and reforming of their surface for catalytic properties. Phosphorus Res. Bull. **9**, 69–74 (1999).

168. Condrate, R. A. Infrared and Raman spectra of glasses containing rare earth ions. Key Eng. Mater. **94-95**, 209–232 (1994).

169. Brow, R. K. Section 1. Structure. Review: the structure of simple phsophate glasses. J. Non. Cryst. Solids **263-264**, 1–28 (2000).

# Appendix A.

Phase Equilibria Database software.

Description of reported diagrams.

Diagram Figure 2. 1:

## $K_2O$-$P_2O_5$-$H_2O$

Fig. **13443**—System $KH_2PO_4$. *P-T*(°C) diagram of $KH_2PO_4$. I, IV, and V = unknown phases; II = tetragonal I-42d (paraelectric); II′ = monoclinic phase; III = orthorhombic Fdd2 (ferroelectric).
E. Rapoport, J. B. Clark, and P. W. Richter, *J. Solid State Chem.*, **24** [3-4] 423-433 (1978).

The phase diagram of $KH_2PO_4$ has been reported;[1] the diagram is as reported in Ref. 2. No other details are given. See also Fig. 13427 for later work on this system.

1. E. Rapoport, *J. Chem. Phys.*, **53** [1] 311-314 (1970).
2. C. W. F. T. Pistorius; pp. 1-151 in Progress in Solid State Chemistry, **Vol. 11**. Edited by J. McCaldin and G. Somorjai. Pergamon Press, New York (1976).

Diagram Figure 2. 2:

## $Cs_2O$-$P_2O_5$-$H_2O$

Fig. **13423**—System $Cs_2O$-$P_2O_5$-$H_2O$. *P-T*(°C) diagram of $CsH_2PO_4$. I = unknown crystal structure; II = monoclinic phase $C_2^2$-$P2_1$; III = monoclinic (paraelectric) phase $C_{2h}^2$-$P2_1/m$; V and VI = unknown crystal structure.
E. Rapoport, J. B. Clark, and P. W. Richter, *J. Solid State Chem.*, **24** [3-4] 423-433 (1978).

The $CsH_2PO_4$ specimen was prepared by neutralizing solutions of $Cs_2CO_3$ (purity 99.5%) with $H_3PO_4$ using methyl orange as an indicator. The solid was precipitated by adding alcohol, vacuum-drying, and heating at 80°C for ~12 h; specimens were characterized by X-ray powder diffraction. Pressure was generated with a piston-cylinder device and the phase transformations were detected by DTA using Chromel-Alumel thermocouples. The samples were contained in Ni and Cu capsules. Heating/cooling rates varied between 0.2-1.5°C/s. Temperatures were determined to ±2°C and pressures were determined to ±0.05 GPa.
The phase boundaries of the phase transformations are reported. Triple points are given in the following table. Phase IV is the ferroelectric phase which occurs below 119.5°C, and is not shown on the diagram.

| Temp.<br>Triple Points | P, GPa | (°C) |
|---|---|---|
| $CsH_2PO_4$-I/II/V | 1.10 | 262 |
| $CsH_2PO_4$-II/III/V | 1.12 | 148 |
| $CsH_2PO_4$-I/V/VI | 2.99 | 385 |
| $CsH_2PO_4$-I/VI/Liquid | 4.20 | 457 |

## Appendix B.

Calculation of water partial pressure and listed values of humidity

| Water partial pressure, atm (T=250 °C, Vair=1 L/min) | Water pumping rate, ml/min | Water partial pressure, atm (T=250 C, Vair=0,5 L/min) | water pumping rate, ml/min |
|---|---|---|---|
| | | 0.15 | 0.08 |
| 0.12 | 0.1 | 0.21 | 0.1 |
| 0.21 | 0.2 | 0.35 | 0.2 |
| 0.29 | 0.3 | 0.45 | 0.3 |
| 0.35 | 0.4 | 0.52 | 0.4 |
| 0.40 | 0.5 | 0.58 | 0.5 |
| 0.45 | 0.6 | 0.62 | 0.6 |
| 0.49 | 0.7 | 0.66 | 0.7 |
| 0.52 | 0.8 | 0.68 | 0.8 |
| 0.55 | 0.9 | 0.71 | 0.9 |
| 0.58 | 1 | 0.73 | 1 |
| 0.60 | 1.1 | 0.75 | 1.1 |
| 0.62 | 1.2 | 0.77 | 1.2 |
| 0.64 | 1.3 | 0.78 | 1.3 |
| 0.66 | 1.4 | 0.79 | 1.4 |
| 0.67 | 1.5 | 0.80 | 1.5 |

# Appendix C

a 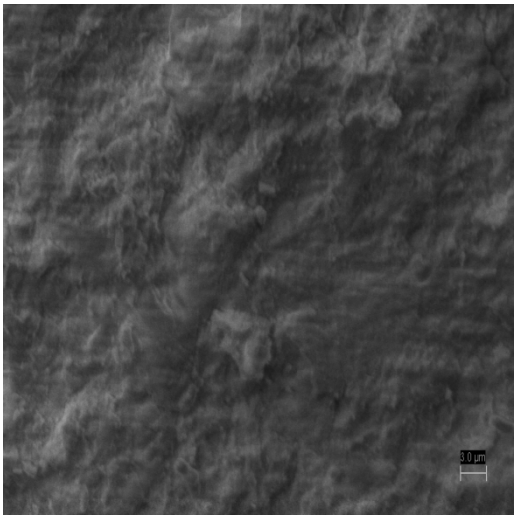


b 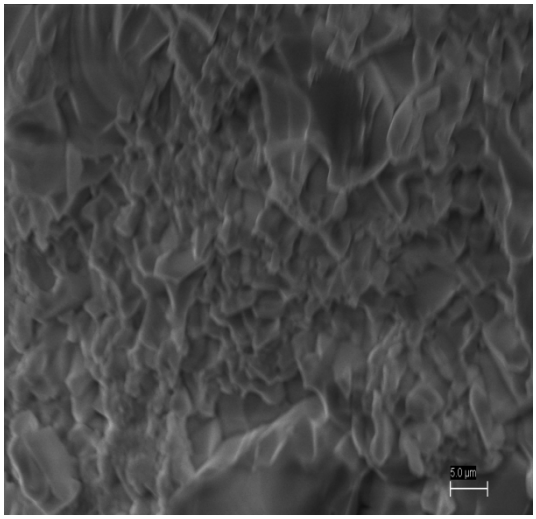


c 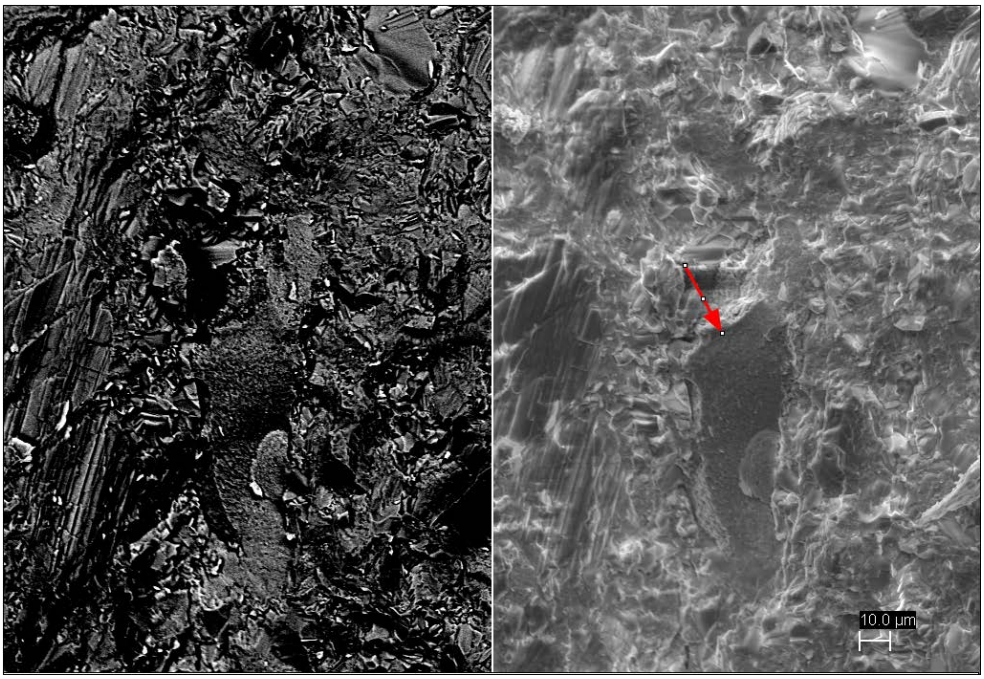


*The cross section area of samples prepared from powders a) $NdPO_4 \cdot 0.5H_2O$ (3µm) b) $CsH_2PO_4$ (5µm) c)* 29 $NdPO_4 \bullet 0.5H_2O$ - 71 $CsH_2PO_4$ (29NdP-71CDP) *composite both back scattering to the left and secondary electron image to the right (10µm) .*

## Appendix C

These images shows three secondary electron images of cross section of the samples made from a) $NdPO_4$•$0.5H_2O$ ( NdP), b) $CsH_2PO_4$ (CDP) and c) composite material 29 $NdPO_4$•$0.5H_2O$ - 71 $CsH_2PO_4$ (29NdP-71CDP) .

The image a shows a cross section of the sample prepared from NdP. The sample was dense, strong and had not shown visible defects of microstructure. The sample prepared from $CsH_2PO_4$ (b) show a layered structure. Indeed it seems like it consist of small crystals. The secondary electron image of composite material 29NdP-71CDP) (c (right)) showes two different regions. The region 1 consisted of only CDP. The second region shown by a red arrow consisted of a dense layer without visual defects. It contained $CsH_2PO_4$ and $NdPO_4$•$0.5H_2O$ (Region 2). This was proved by Energy-dispersive X-ray spectroscopy (EDX) see Table C.

*Table C. The elemental content of 29NdP-71CDPcomposite measured by EDX spectroscopy.*

| Name of element | Theoretical calculation | EDX | | |
|---|---|---|---|---|
| | | Region 1 | Region 2 | Average |
| Nd | 18.1 | - | 37.0 | 13.9 |
| Cs | 39.1 | 57.7 | 16.3 | 39 |
| P | 13 | 13 | 12.7 | 13.2 |
| O | 28.9 | 27.7 | 32.6 | 33.9 |
| C | - | 1.6 | 1.4 | - |
| H | 0.8 | - | - | - |

## Appendix C

The heating program was developed separately to study both temperature dependence of conductivity and stability of samples. The impedance spectra were recorded every 5 minutes during heating program. It should be said that real temperature of the cell was always different from program.

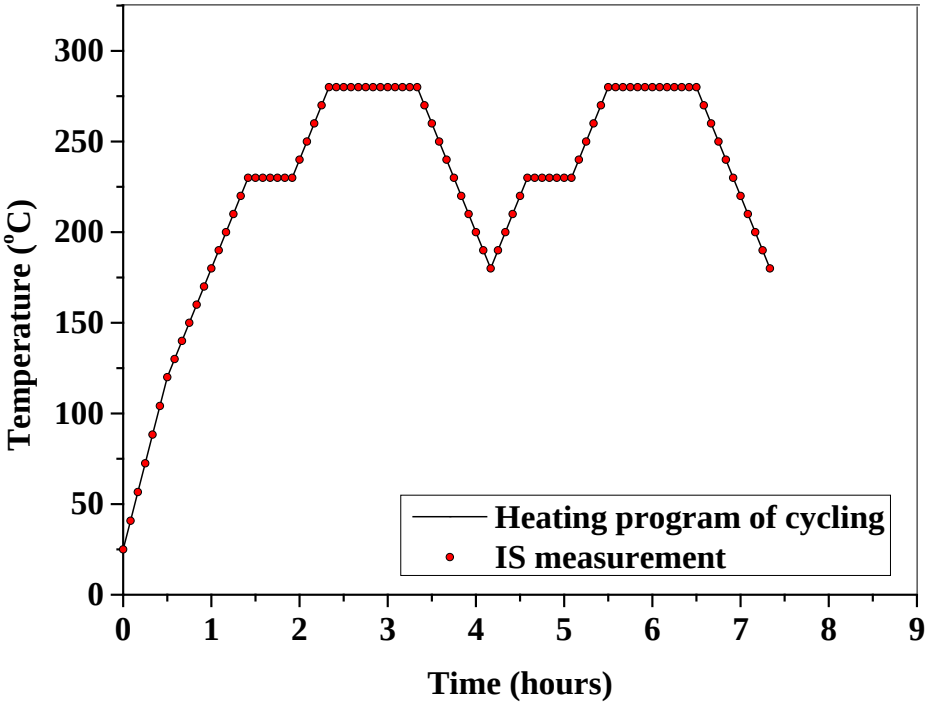


*Heating program of Cell type 4 together with recoding of IS spectra.*

## Appendix C

For measurements of the electromotive force (EMF), open circuit voltage (OCV) and fuel cell performance, pressed discs of phosphate composites with thicknesses of around 700 microns were fabricated. Taking advantages of using a previously available recipe without further optimization, $CsH_2PO_4$, without addition of NdP, was used in the catalyst layer. The electrodes were prepared by spraying a catalyst layer from a mixture of $CsH_2PO_4$, Pt black (Aldrich, 27 $m^2$ $g^{-1}$) and platinum supported on carbon (60 mass% Pt, Johnson Matthey), onto the gas diffusion layer (GDL) of Toray carbon paper. The ratio of the three solid components in the catalyst layer was 1:6:6 by mass with a total Pt loading of 7 $mgcm^{-2}$. EMF measurements were performed by feeding the cell with pure hydrogen on one side and a mixture of hydrogen and nitrogen on the other side. The EMF was then measured as a function of temperature from 150°C to 240°C. OCV and fuel cell demonstrations were performed by feeding the cell with humidified hydrogen on one side and humidified air on the other side.

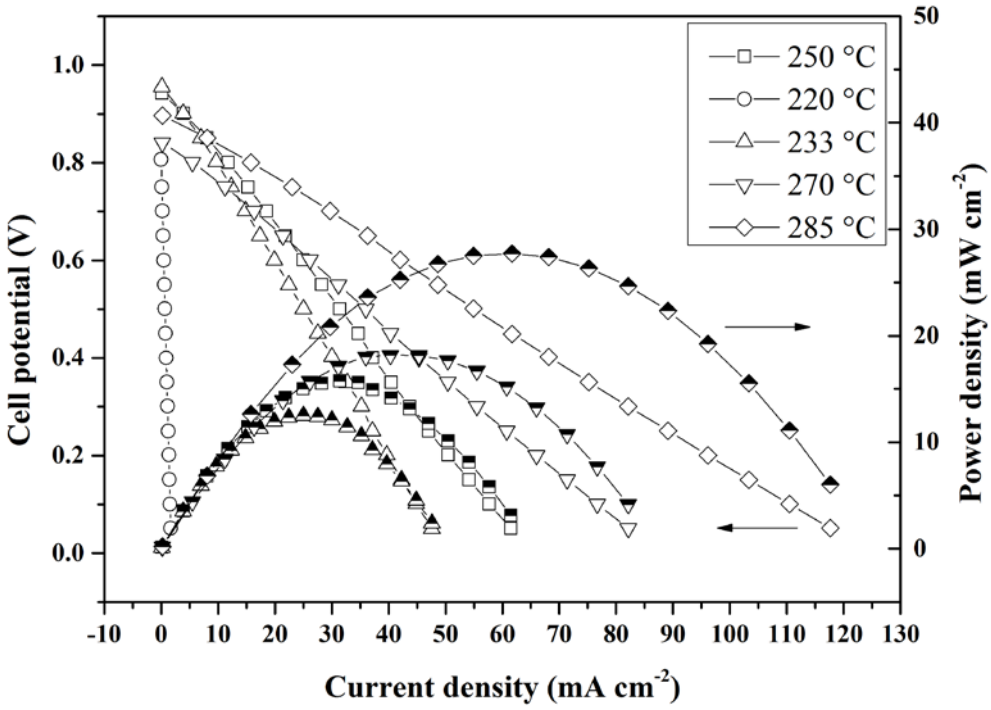


I-V and I-P characteristics of single cells at 230 and 250 °C. [70% $H_2/H_2O$, Pt|0.3x$NdPO_4$•n$H_2O$-$CsH_2PO_4$|Pt, 70% air/$H_2O$.

# Appendix D

Ratio of phosphoric acid to $Sn_{1-x}In_x(P_2O_7)_{1-\delta}$

| Material | Ratio of $H_3PO_4$: $Sn_{1-x}In_x(P_2O_7)_{1-\delta}$ |
|---|---|
| CA2 | 1:2.93 |
| MC3 | 1:31.06 |
| MC2 treated | 1:3.76 |
| MA2 treated | 1:76.46 |

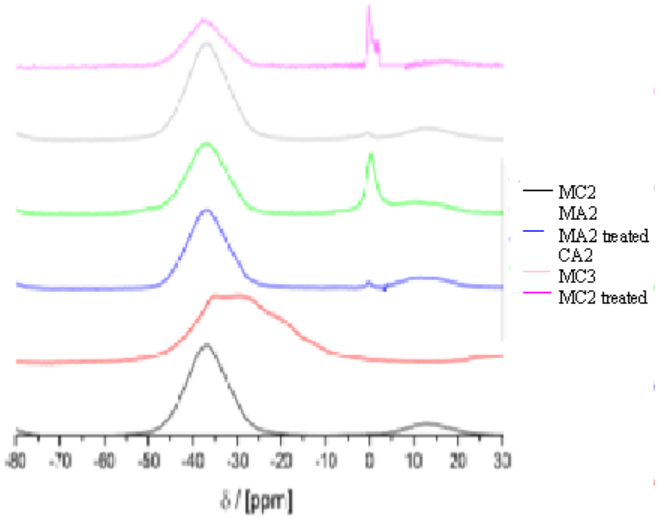


Overview of measured $^{31}$P-NMR spectra. The MC2 treated spectrum has been multiplied by a constant of 15 and data has been removed from 2-10 ppm since an experimental error gave a large misreading in this range

# Appendix D

**Element mapping electron image of $Sn_{0,9}In_{0,1}P_2O_7$ sample as made**

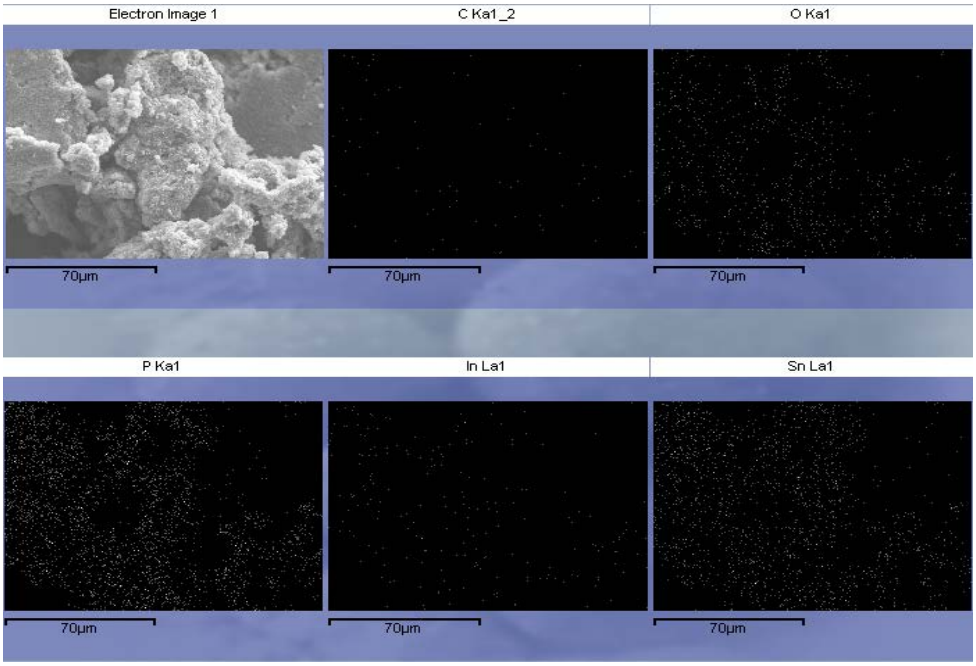


**Element mapping electron image of $Sn_{0,9}In_{0,1}P_2O_7$ sample washed after synthesis**

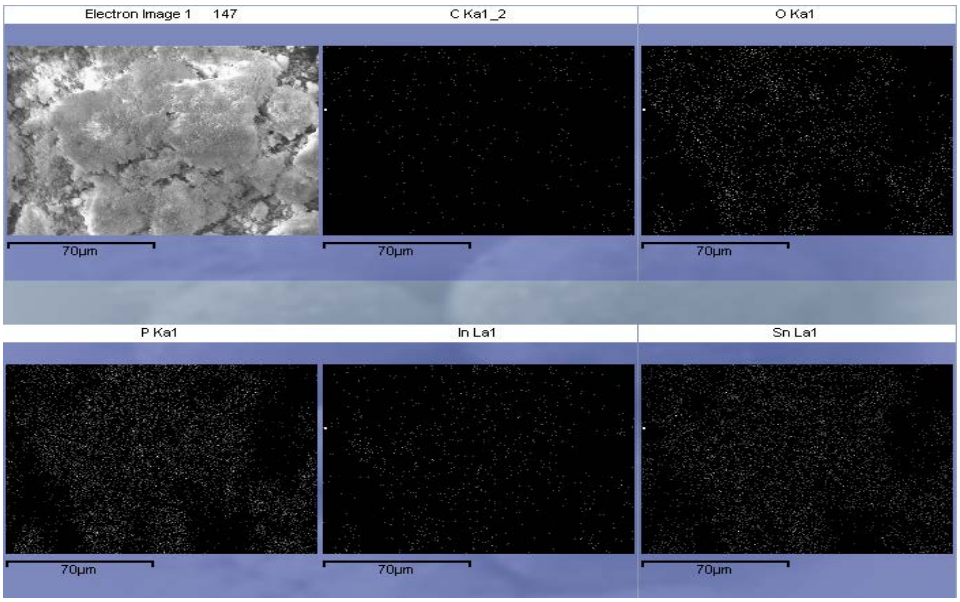

## Appendix E

Types of the cerium phosphates in relation with temperature of synthesis and atomic ratio:

▲ $CePO_4$

○ $CeP_2O_7$

□ $Ce(PO_3)_3$

△ $Ce(PO_3)_4$

● $CeP_5O_{14}$

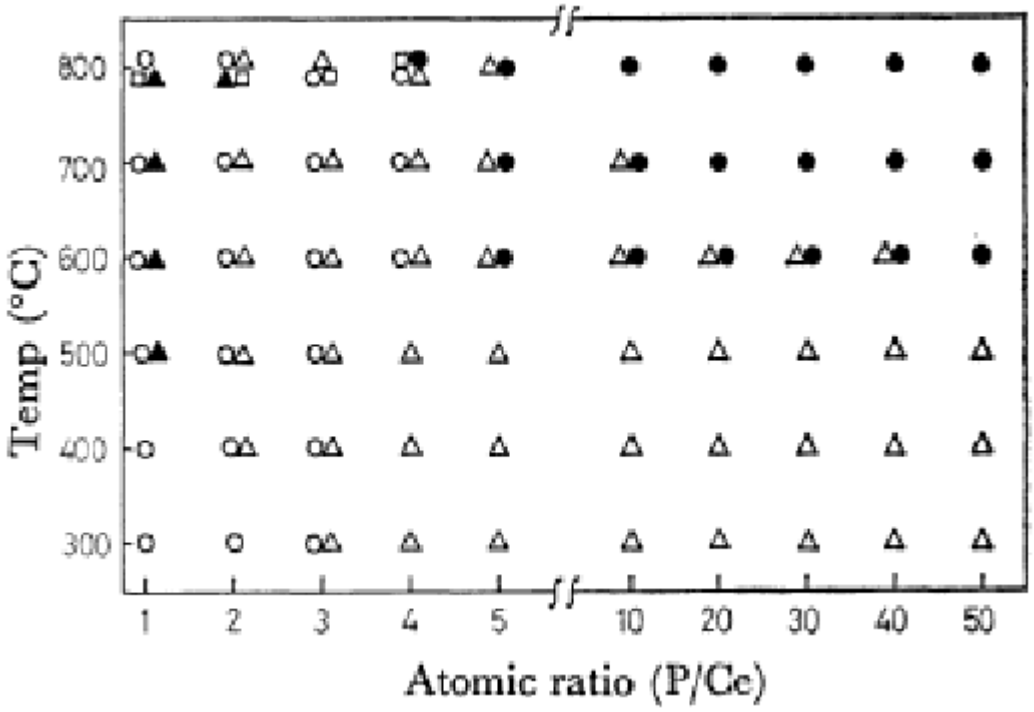

# Appendix E